Crystal structure prediction at high pressures: stability, superconductivity and superionicity

A dissertation submitted for the degree of

Doctor of Philosophy

at the University of Cambridge

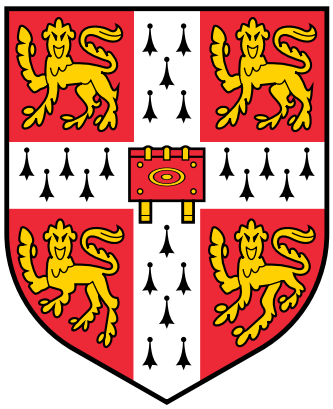

Joseph Richard Nelson

Churchill College, Cambridge

April 2017

Abstract

The physical and chemical properties of materials are intimately related to their underlying crystal structure: the detailed arrangement of atoms and chemical bonds within. This thesis uses computational methods to predict crystal structure, with a particular focus on structures and stable phases that emerge at high pressure. We explore three distinct systems.

We first apply the *ab initio* random structure searching (AIRSS) technique and density functional theory (DFT) calculations to investigate the high-pressure behaviour of beryllium, magnesium and calcium difluorides. We find that beryllium fluoride is extensively polymorphic at low pressures, and predict two new phases for this compound − the silica moganite and $CaCl_2$ structures − to be stable over the wide pressure range 12−57 GPa. For magnesium fluoride, our results show that the orthorhombic 'O-I' TiO_2 structure (*Pbca*, $Z = 8$) is stable for this compound between 40 and 44 GPa. Our searches find no new phases at the static-lattice level for calcium difluoride between 0 and 70 GPa; however, a phase with $P\bar{6}2m$ symmetry is energetically close to stability over this pressure range, and our calculations predict that this phase is stabilised at high temperature. The $P\bar{6}2m$ structure exhibits an unstable phonon mode at large volumes which may signal a transition to a superionic state at high temperatures. The Group-II difluorides are isoelectronic to a number of other AB_2-type compounds such as SiO_2 and TiO_2, and we discuss our results in light of these similarities.

Compressed hydrogen sulfide (H_2S) has recently attracted experimental and theoretical interest due to the observation of high-temperature superconductivity in this compound ($T_c = 203$ K) at high pressure (155 GPa). We use the AIRSS technique and DFT calculations to determine the stable phases and chemical stoichiometries formed in the hydrogen-sulfur system as a function of pressure. We find that this system supports numerous stable compounds: H_3S, H_7S_3, H_2S, H_3S_2, H_4S_3, H_2S_3 and HS_2, at various pressures. Working as part of a collaboration, our predicted H_3S and H_4S_3 structures are shown to be consistent with XRD data for this system, with H_4S_3 identified as a major decomposition product of H_2S in the lead-up to the superconducting state.

Calcium and oxygen are two elements of generally high terrestrial and cosmic abundance, and we explore structures of calcium peroxide (CaO_2) in the pressure range 0−200 GPa. Stable structures for CaO_2 with $C2/c$, $I4/mcm$ and $P2_1/c$ symmetries emerge at pressures below 40 GPa, which we find are thermodynamically stable against decomposition into CaO and O_2. The stability of CaO_2 with respect to decomposition increases with pressure, with peak stability occurring at the CaO B1−B2 phase transition at 65 GPa. Phonon calculations using the quasiharmonic approximation show that CaO_2 is a stable oxide of calcium at mantle temperatures and pressures, highlighting a possible role for CaO_2 in planetary geochemistry, as a mineral redox buffer. We sketch the phase diagram for CaO_2, and find at least five new stable phases in the pressure/temperature ranges $0 \leq P \leq 60$ GPa, $0 \leq T \leq 600$ K, including two new candidates for the zero-pressure ground state structure.

Preface

The following dissertation reports work completed by the author between October 2013 and April 2017 in the Theory of Condensed Matter group at the University of Cambridge. This work was carried out under the supervision of Professor Richard J. Needs, and was also conducted in close collaboration with Professor Chris J. Pickard in the Department of Materials Science and Metallurgy, University of Cambridge.

This dissertation is the result of my own work, and includes nothing which is the outcome of work done in collaboration except where specifically stated in the text. It has not, either in whole or in part, been submitted for another degree, diploma or any other qualification at this or any other university. This document does not exceed the 60,000 word limit prescribed by the Physics and Chemistry Degree Committee at the University of Cambridge.

Joseph Richard Nelson
Cambridge, April 2017

Acknowledgements

I extend a warm thank-you to my supervisor, Richard Needs, and to Professor Chris Pickard. Both Richard and Chris are unwaveringly generous with their time, knowledge and expertise, which I have benefitted greatly from over the past $3\frac{1}{2}$ years.

To my wife Gemma, and daughter Elsa, I am appreciative to you both for your support and encouragement over the years. I have also received tremendous support from my family over this time: in particular, from my parents, Keren and Jon, my siblings James and Juliet, and from Ron, Jackie and Robert Goodfellow.

Thanks is also due to several members (both former and current) of the Theory of Condensed Matter group at Cavendish, for fostering a sense of community in the group and creating a great environment to learn physics. Particular thanks goes to David Turban and James Hamp, who shared an office with me.

Finally, I acknowledge my funding body, the Cambridge Commonwealth Trust. I am the grateful recipient of a joint Prince of Wales and C. T. Taylor award from the Trust, which made it possible to come to Cambridge from New Zealand to take up this PhD.

Contents

Chapter 1

Introduction

This thesis follows three main themes: crystal structure prediction, electronic structure calculations, and high-pressure physics. In this introduction, we give a broad overview of these areas of physics.

The properties of a material are closely related to its underlying crystal structure. A very familiar example is carbon, where atoms can be arranged in 2D hexagonal sheets, creating a soft, flaky and opaque material suitable for use in pencils (graphite), or with atoms arranged in a 3D network, creating an extremely hard and transparent material, suitable for industrial cutting (diamond).

Given the strength of the link between structure and material properties, there are now many experimental techniques available for determining crystal structure. The most well-known of these is x-ray diffraction, for which the 1915 Nobel Prize in Physics was awarded to father-and-son physicists W. H. and W. L. Bragg. This technique, and the many crystal structures it has uncovered, has had a profound impact on the history of science; among other discoveries, x-ray crystallography was used to determine the structure of penicillin. In elucidating the crystal structure of a material, we gain a deep understanding of how it functions and interacts at the atomic level.

The research presented in this thesis takes a different, computational approach to structure determination. We focus on methods that allow us to predict crystal structure from *first principles* − that is, without recourse to any prior knowledge, other than the constituent atoms. The process of crystallization in a solid is guided by the simple principle that atoms will position themselves in the arrangement of least energy, so from a technical standpoint the task of predicting crystal structure is an optimization problem. Two ingredients are therefore key: (i) a method for reliably generating candidate crystal structures, and (ii) a method for reliably calculating the energy of structures, in order to compare them to others. The latter point typically means that we must use quantum mechanics, as the uniquely quantum−mechanical phenomena of electron exchange and correlation contribute to the total energy of a structure in a highly non−trivial manner.

It would be an understatement to say that our understanding of the physical world was irreversibly altered with the formulation of quantum mechanics. Published in 1926, the time independent Schrödinger equation

$$H\Psi = E\Psi \tag{1.1}$$

purported to contain in its solution Ψ all possible information about the system described by the Hamiltonian H. This would lead Paul Dirac, three years after its publication and experimental validation in systems such as hydrogen and helium, to make his famous remark that 'chemistry had come to an end' [1]:

"The underlying physical laws necessary for the mathematical theory of a large part of physics and the whole of chemistry are thus completely known, and the difficulty is only that the exact application of these laws leads to equations much too complicated to be soluble."

-P. A. M. Dirac, 1929 [2]

In this thesis, we are interested in *electronic structure*, and our 'system' is therefore a set of interacting electrons and nuclei. Arguably the very first calculation performed with the Schrödinger equation, namely the determination of the energy levels of the hydrogen atom, falls into this same category. In saying that we must use quantum mechanics to calculate the energies of crystal structures, we mean that we must solve Eq. (1.1) for the energy E.

Aside from just the energy of a crystal structure, the power of the Schrödinger equation is that it provides us with the ability to make first-principles predictions of a wide array of material properties, such as mechanical hardness, electrical conductivity, and response to temperature or pressure. However, as we saw with the example of carbon in the opening paragraph of this chapter, we need the correct crystal structure at hand before making such predictions.

Approaching electronic structure using quantum mechanics is a formidable task for all but the simplest of systems, and approximations are at some point necessary. An early approximation to solutions of Eq. (1.1) was Hartree-Fock theory, which introduces the idea that our system of interacting electrons and nuclei can be replaced by a set of non-interacting electrons moving in an *average* potential. This idea is also central to density functional theory (DFT), which is the method we use exclusively in this thesis for our first-principles calculations. DFT describes a system in terms of the electron density alone, rather than the full many-body wavefunction Ψ. This allows a computationally feasible solution to the Schrödinger equation without sacrificing its first-principles predictive power. State-of-the-art DFT calculations are at the time of writing capable of deducing the electronic structure of systems with thousands of atoms [3]. This has allowed a first-principles study of systems, such as biological molecules and nanostructures, whose size and complexity previously meant they were

only describable at the macroscopic level of theory.

The application of high pressure to a system can strongly modify its electronic structure. In this thesis, we work with pressures on the gigapascal (GPa) scale. Gigapascal pressures can allow otherwise unreactive noble gases to form chemical compounds [4], turn grey sodium metal transparent [5], or turn gaseous oxygen into a superconducting metal [6]. These pressures are well above those encountered at Earth's surface (0.0001 GPa) or even at the bottom of the Mariana trench (≈0.11 GPa), but they are encountered deep within planetary interiors, and as such are usually associated with high temperatures. For example, the center of the Earth is expected to be at a pressure of 360 GPa; the pressure at the center of Jupiter is around 10 times larger still. One advantage of a first-principles approach to structure prediction is that these extreme environments can be studied very efficiently through computational means. On the experimental side, state-of-the-art double diamond anvil cell apparatus can currently attain static pressures of around 640 GPa in the laboratory [7].

The subsequent chapters of this thesis are set out as follows. In Chapter 2, we give a description of electronic structure calculations and in particular density functional theory, and show how practical calculations determine energies, forces, phonon frequencies and lattice thermodynamics. In Chapter 3, we examine crystal structure prediction, showing the many different approaches now possible for predicting crystal structure from first principles. Chapter 4 applies these methods to the Be-F, Mg-F and Ca-F systems at pressures up to 70 GPa, and Chapter 5 looks at stable compounds in the H-S system over the pressure range 25-200 GPa. In Chapter 6, we predict structures for CaO_2 at pressures up to 200 GPa. Finally, we give our conclusions and some directions for future research in Chapter 7.

Chapter 2

Density functional theory

In this chapter, we provide the theoretical background for density functional theory, the method we have used in this thesis to carry out electronic structure calculations.

The starting point for a discussion of electronic structure is the non-relativistic Hamiltonian describing a system of N electrons and M nuclei (with nuclear charges Z_α), interacting mutually by the Coulomb force. It is given by:

$$H = -\sum_{\alpha=1}^{M} \frac{1}{2M_\alpha}\nabla_\alpha^2 - \sum_{i=1}^{N} \frac{1}{2}\nabla_i^2 + \frac{1}{2}\sum_{\alpha\neq\beta}^{M} \frac{Z_\alpha Z_\beta}{|\mathbf{r}_\alpha - \mathbf{r}_\beta|} - \sum_{i=1}^{N}\sum_{\alpha=1}^{M} \frac{Z_\alpha}{|\mathbf{r}_i - \mathbf{r}_\alpha|} + \frac{1}{2}\sum_{i\neq j}^{N} \frac{1}{|\mathbf{r}_i - \mathbf{r}_j|}. \tag{2.1}$$

Eq. (2.1) is written in (Hartree) **atomic units**, where lengths $\mathbf{r}_i$ are measured in multiples of Bohr radii (0.52918 Å), energy is in Hartrees (1 Ha = 27.211 eV) and masses are given relative to that of the electron [8]. Our theoretical development will proceed with these units throughout this thesis, however the results of calculations will tend to use electron-volts (eV) and Angstroms (Å) as the energy and length units; this will be clearly indicated. The terms in the Hamiltonian of Eq. (2.1) describe the nuclear kinetic energy, electron kinetic energy, nuclear-nuclear interaction, nuclear-electron interaction and electron-electron interactions respectively.

2.1 The Born-Oppenheimer approximation

Making the *Born-Oppenheimer* approximation is a simplifying assumption that allows us to separate the nuclear and electronic degrees of freedom in Eq. (2.1). The nuclei are substantially heavier than the electrons, so we may consider the terms in $1/M_\alpha$ in Eq. (2.1) to be small. Hence the nuclear kinetic energy term above can, to lowest perturbative order, be neglected. The nuclear-nuclear interaction term, which we denote by E_{II} (for 'ion-ion', following [9]) can be absorbed into the energy eigenvalue

E of Eq. (1.1), giving:

$$H = \underbrace{-\sum_{i=1}^{N} \frac{1}{2}\nabla_i^2}_{\equiv T} + \sum_{i=1}^{N} \underbrace{\sum_{\alpha=1}^{M} \frac{-Z_\alpha}{|\mathbf{r}_i - \mathbf{r}_\alpha|}}_{\equiv V_{nuc}(\mathbf{r}_i)} + \underbrace{\frac{1}{2}\sum_{i\neq j}^{N} \frac{1}{|\mathbf{r}_i - \mathbf{r}_j|}}_{\equiv U}. \tag{2.2}$$

This is referred to as the *electronic* Hamiltonian, which now describes a set of N electrons moving in the potential created by a field of M nuclei that are taken to be 'frozen' in place. The designations T, $V_{nuc}(\mathbf{r})$ and U are for later convenience.

In the full Hamiltonian of Eq. (2.1), the wavefunction Ψ is in general an explicit function of all electron *and* nuclear positions $\mathbf{r}_i$ and $\mathbf{r}_\alpha$. Wavefunctions for the electronic Hamiltonian are considered to explicitly depend on $\mathbf{r}_i$, and parametrically depend on $\mathbf{r}_\alpha$.

A full perturbative treatment of the Born-Oppenheimer approximation has been taken up, for example, by Born and Huang [10], where a perturbation expansion in $(1/M_\alpha)^{1/4}$ is developed.

2.2 Hartree-Fock theory

The electronic wavefunction corresponding to Eq. (2.2) must be antisymmetric under the exchange of any of the coordinates of two different electrons. This includes both the spatial $\mathbf{r}$ and spin σ coordinates of those electrons. In Hartree-Fock ('HF') theory, this wavefunction is approximated by a single *Slater determinant*:

$$\Psi^{HF} = \frac{1}{\sqrt{N!}} \det \begin{bmatrix} \chi_1(\mathbf{r}_1,\sigma_1) & \chi_2(\mathbf{r}_1,\sigma_1) & \dots & \chi_N(\mathbf{r}_1,\sigma_1) \\ \chi_1(\mathbf{r}_2,\sigma_2) & \chi_2(\mathbf{r}_2,\sigma_2) & \dots & \chi_N(\mathbf{r}_2,\sigma_2) \\ \vdots & \vdots & & \vdots \\ \chi_1(\mathbf{r}_N,\sigma_N) & \chi_2(\mathbf{r}_N,\sigma_N) & \dots & \chi_N(\mathbf{r}_N,\sigma_N) \end{bmatrix} \tag{2.3}$$

where the $\chi_i(\mathbf{r},\sigma)$ are one-particle spin orbitals [8, 9], which we take to be orthonormal. The properties of the determinant ensure that Ψ^{HF} has the required antisymmetry.

The spin orbitals are products of spatial orbitals $\psi_i(\mathbf{r})$ and spin functions $\alpha(\sigma)$ or $\beta(\sigma)$ (spin up or down). For convenience, let us take $\chi_i(\mathbf{r},\sigma) = \psi_i(\mathbf{r})\alpha(\sigma)$ for $i = 1, 2, ..., A$ and $\chi_i(\mathbf{r},\sigma) = \psi_i(\mathbf{r})\beta(\sigma)$ for $i = A+1, A+2, ..., N$. The energy E of Eq. (2.3) with

H as in Eq. (2.2) is then:

$$
\begin{aligned}
E^{HF} &= \langle \Psi^{HF} | H | \Psi^{HF} \rangle \qquad (2.4)\\
&= \sum_{i=1}^{N} \int d^3r \; {\psi_i}^*(\mathbf{r}) \left[-\frac{1}{2}\nabla^2 + V_{nuc}(\mathbf{r}) \right] \psi_i(\mathbf{r}) \\
&\quad + \frac{1}{2} \sum_{i,j=1}^{N} \int d^3r d^3r' \; {\psi_i}^*(\mathbf{r}) {\psi_j}^*(\mathbf{r}') \frac{1}{|\mathbf{r}-\mathbf{r}'|} \psi_i(\mathbf{r}) \psi_j(\mathbf{r}') \qquad \text{(Direct terms)} \\
&\quad - \frac{1}{2} \left[\sum_{i,j=1}^{A} + \sum_{i,j=A+1}^{N} \right] \int d^3r d^3r' \; {\psi_i}^*(\mathbf{r}) {\psi_j}^*(\mathbf{r}') \frac{1}{|\mathbf{r}-\mathbf{r}'|} \psi_j(\mathbf{r}) \psi_i(\mathbf{r}'). \qquad \text{(Exchange terms)}
\end{aligned}
$$

Exchange terms are only summed over orbitals of the same spin.

We consider the (true) ground state wavefunction Ψ of the electronic Hamiltonian, whose energy eigenvalue is E. The variational principle:

$$
\frac{\langle \Psi^{HF} | H | \Psi^{HF} \rangle}{\langle \Psi^{HF} | \Psi^{HF} \rangle} \geq E, \qquad (2.5)
$$

must therefore hold. The idea in Hartree-Fock theory is to vary the spatial orbitals $\psi_i(\mathbf{r})$ that constitute Ψ^{HF} so as to obtain the best approximation to Ψ and E. We therefore wish to minimise Eq. (2.4) subject to the constraint that these spatial orbitals are kept orthonormal. One employs a set of Lagrange multipliers ϵ_{ij} to enforce the constraint, and so we have[1]:

$$
\frac{\delta}{\delta {\psi_i}^*(\mathbf{r})} (\langle \Psi^{HF} | H | \Psi^{HF} \rangle - \epsilon_{ij} (\langle \psi_i | \psi_j \rangle - \delta_{ij})) = 0, \qquad (2.6)
$$

giving rise to the Hartree-Fock equations for the spatial orbitals $\psi_i(\mathbf{r})$ [9]:

$$
\begin{aligned}
&\left(-\frac{1}{2}\nabla^2 + V_{nuc}(\mathbf{r}) + \sum_{j=1}^{N} \int d^3r' \; {\psi_j}^*(\mathbf{r}') \frac{1}{|\mathbf{r}-\mathbf{r}'|} \psi_j(\mathbf{r}') \right. \qquad (2.7)\\
&\left. - \left[\sum_{i,j=1}^{A} + \sum_{i,j=A+1}^{N} \right] \int d^3r' \; {\psi_j}^*(\mathbf{r}') \frac{1}{|\mathbf{r}-\mathbf{r}'|} \frac{\psi_j(\mathbf{r})}{\psi_i(\mathbf{r})} \psi_i(\mathbf{r}') \right) \psi_i(\mathbf{r}) = \epsilon_i \psi_i(\mathbf{r}).
\end{aligned}
$$

We can think of all the terms except $-\frac{1}{2}\nabla^2$ in parentheses as an *effective* potential $V_{\text{eff}}(\mathbf{r})$. What we then notice is that Eq. (2.7) appears to be a set ($i = 1, 2, ..., N$) of Schrödinger-like equations describing the motion of N 'independent' electrons, each moving in a potential $V_{\text{eff}}(\mathbf{r})$ generated by all the other electrons. The Lagrange multipliers ϵ_i appear to take on the role of 'energies', but care must be taken in too literal an interpretation: for example, it is not the case that $E = \sum_{i=1}^{N} \epsilon_i$. This idea of reformulating the N-body problem posed by Eq. (2.2) into N separate single-particle

[1] Here, we perform a variation with respect to ${\psi_i}^*(\mathbf{r})$. A variation with respect to $\psi_i(\mathbf{r})$ gives the same result [11].

problems was a significant concept introduced by Hartree-Fock theory.

$V_{\text{eff}}(\mathbf{r})$ is comprised of the nuclear potential, direct and exchange terms. The exchange terms allow correlation between electrons of the same spin, but not of opposite spin. This reflects our choice of wavefunction Eq. (2.3), which respects the Pauli exclusion principle. In light of this, it is customary to refer to the difference between the Hartree-Fock energy $\langle \Psi^{HF}|H|\Psi^{HF}\rangle$, with orbitals from Eq. (2.7), and the true energy $E = \langle \Psi|H|\Psi\rangle$ as the *correlation energy* [8].

Various improvements can be made on the basic Hartree-Fock method given here. For example, in Eq. (2.3), we write the true wavefunction Ψ as a single Slater determinant. While this is only an approximation to Ψ, it is true that Ψ can be expanded exactly as an infinite sum of Slater determinants. *Configuration interaction* is a method that pursues this approach [8].

2.3 Density-functional theory

"This raised a general question in my mind: Is a complete, exact description of electron structure in terms of $n(\mathbf{r})$ possible in principle?"

-W. Kohn [1]

The essence of DFT is encapsulated in this quote by Walter Kohn[2]. DFT seeks a complete description of a system of N interacting electrons in terms of the particle number density:

$$n(\mathbf{r}) = N \int d^3r_2 ... d^3r_N \Psi^*(\mathbf{r}, \mathbf{r}_2, ..., \mathbf{r}_N)\Psi(\mathbf{r}, \mathbf{r}_2, ..., \mathbf{r}_N). \tag{2.8}$$

Quantities such as the total energy E of the system are then given as *functionals* of $n(\mathbf{r})$: $E = E[n(\mathbf{r})]$ and so on. In DFT, it is the density that is the central quantity as opposed to the wavefunction. The founding ideas of DFT were developed and made mathematically rigorous by Pierre Hohenberg and Walter Kohn in the early 1960s. We turn our attention to some of the key elements of DFT now.

Only $n(\mathbf{r})$?
Ordinarily, we determine quantities such as E from the full wavefunction Ψ. In calculating $n(\mathbf{r})$ however, we integrate out all but 3 variables (in the absence of spin) of Ψ. Hence there is the question of whether $n(\mathbf{r})$ alone is *enough* to determine E or other observables of interest. The Hohenberg-Kohn theorem shows that, for the *ground-state* density $n(\mathbf{r})$, the density is indeed sufficient to completely characterise the system. Following Kohn [1], we have:

[2] "For his development of the density-functional theory", Kohn shared the 1998 Nobel Prize in Chemistry with John Pople.

Hohenberg-Kohn Theorem

Given a system of interacting electrons, the external potential $V(\mathbf{r})$ is uniquely determined by the ground state density $n(\mathbf{r})$ of the system, up to an additive constant. Another way of stating this is that the external potential $V(\mathbf{r})$ is a unique functional of the ground state density $n(\mathbf{r})$.

The proof of this theorem begins by assuming that this is not the case, and invokes the variational principle to arrive at a contradiction. One can refer to [1, 9] for further details. A corollary of this theorem then gives our result: if $n(\mathbf{r})$ can determine $V(\mathbf{r})$, then the system Hamiltonian H is determined uniquely, since the kinetic terms T and electron-electron interaction terms U (Eq. (2.2)) are *universal* to all systems of interacting electrons. Hence Ψ and quantities like E derived from H are determinable, and the system is completely characterised. In this context $V(\mathbf{r})$ could be $V_{nuc}(\mathbf{r})$, as in Eq. (2.2), or for example the potential due to some external electric field.

Why $n(\mathbf{r})$?

Perhaps one of the best reasons for choosing $n(\mathbf{r})$ as the fundamental quantity is that it is observable. For example, charge density analysis of X-ray diffraction data can be used to experimentally deduce the electron density. Kohn [1] discusses some fundamental difficulties that arise with regards to the computational complexity encountered when attempting to work with the exact, many-body wavefunction Ψ of Eq. (1.1). If we consider a set of single-particle states $\phi_i(\mathbf{r})$, $i = 1, 2, ..., q$, and expand Ψ in a basis of product states formed from these, this expansion will contain a total of q^N terms, where N is the number of electrons. As N increases, determining Ψ involves an energy minimisation with respect to an *exponentially* growing number of variables, and quickly becomes infeasible. Kohn [1] refers to this exponential dependence as an 'exponential wall' which severely limits the size of a system that can be studied with exact wavefunction methods. Improvements can of course be made through the use of better basis sets, but in general the problem remains that working with the exact wavefunction Ψ involves minimising with respect to a rapidly growing number of degrees of freedom as the system size increases. Density functional theory, as we will see in subsequent sections, allows $n(\mathbf{r})$ to be determined from a set of N single particle orbitals only, at a much reduced computational cost.

The explicit functional dependence of quantities like E on the density are not in general known. An early predecessor of DFT, Thomas-Fermi theory, was developed around an approximate explicit formula for E in terms of $n(\mathbf{r})$. Unfortunately, approximations made in Thomas-Fermi theory (and extensions of it) limit its accuracy too much to be useful in describing electronic structure [9]. In DFT, approximations to functionals like $E[n(\mathbf{r})]$ are still required, but the approach to these is slightly different, as we now discuss.

2.4 The Kohn-Sham equations and exchange-correlation functional

We refer extensively to Martin [9] in the development of this section. Let us begin by giving a more exact meaning to functionals like $E[n(\mathbf{r})]$. Here, we follow the *constrained search method* [1, 9], and define:

$$E[n(\mathbf{r})] \equiv \min_{\Psi \to n(\mathbf{r})} \langle \Psi | H | \Psi \rangle, \tag{2.9}$$

where the minimum is taken over all Ψ that give rise to $n(\mathbf{r})$ as in Eq. (2.8). Defining $E[n(\mathbf{r})]$ in this manner allows us to carry over the familiar variational principle into DFT:

$$E[n(\mathbf{r})] \geq E, \tag{2.10}$$

with E the true system ground-state energy. Equality occurs when $n(\mathbf{r})$ is the corresponding ground-state density.

Kohn and Sham ('KS') developed a means by which $E[n(\mathbf{r})]$ could be approximated. They introduced an auxiliary system of N independent electrons, with wavefunctions $\phi_i(\mathbf{r})$, such that the sum of the individual electron densities reproduces the full interacting system density:

$$n(\mathbf{r}) = \sum_{i=1}^{N} |\phi_i(\mathbf{r})|^2. \tag{2.11}$$

We note that this relation also holds true for the Hartree-Fock wavefunction of Eq. (2.3) with $\phi_i(\mathbf{r}) \to \psi_i(\mathbf{r})$. Let us now see how far we can get attempting to write down an expression for $E[n(\mathbf{r})]$ in terms of this auxiliary system. First, the kinetic energy T_s of the auxiliary system is:

$$T_s[n(\mathbf{r})] = -\frac{1}{2} \sum_{i=1}^{N} \int d^3r \; \phi_i{}^*(\mathbf{r}) \nabla^2 \phi_i(\mathbf{r}), \tag{2.12}$$

although this is not the same as the interacting system kinetic energy $\langle \Psi | T | \Psi \rangle$. We next expect a Coulomb-type contribution to the energy, as in the direct terms of the Hartree-Fock energy (Eq. (2.4)):

$$\begin{aligned} E_H[n(\mathbf{r})] &= \frac{1}{2} \sum_{i,j=1}^{N} \int d^3r d^3r' \; \phi_i{}^*(\mathbf{r}) \phi_j{}^*(\mathbf{r}') \frac{1}{|\mathbf{r} - \mathbf{r}'|} \phi_i(\mathbf{r}) \phi_j(\mathbf{r}') \\ &= \frac{1}{2} \int d^3r d^3r' \; \frac{n(\mathbf{r}) n(\mathbf{r}')}{|\mathbf{r} - \mathbf{r}'|}, \end{aligned} \tag{2.13}$$

in light of Eq. (2.11). Lastly, a contribution from an external potential like $V_{nuc}(\mathbf{r})$ is

expected. We persist with the notation $V(\mathbf{r})$ for such external potentials. In all then, we express the total energy as:

$$E[n(\mathbf{r})] = T_s[n(\mathbf{r})] + \int d^3r\ n(\mathbf{r})V(\mathbf{r}) + E_H[n(\mathbf{r})] + E_{xc}[n(\mathbf{r})]. \tag{2.14}$$

The last term in Eq. (2.14) introduces the *exchange-correlation* functional $E_{xc}[n(\mathbf{r})]$. This we have not yet specified. It is defined by Eq. (2.14), i.e., as the difference between the true functional $E[n(\mathbf{r})]$ and the terms from our auxiliary system that we have used to approximate it.

Some of the energy contributions we have not considered, and which must be reflected in $E_{xc}[n(\mathbf{r})]$, are:

(1) A description of electron exchange, as in the exchange terms of the HF energy Eq. (2.4).

(2) A cancellation of the self-interaction energy introduced by the Coulomb contribution for the energy in Eq. (2.13). These are the terms for which $i = j$, and in the HF energy of Eq. (2.4), cancel exactly between the direct and exchange terms.

(3) Electron correlation

(4) Some account for the difference in our auxiliary system kinetic energy Eq. (2.12) and the true interacting system kinetic energy.

Lastly, we come to the KS equations themselves. These determine the wavefunctions $\phi_i(\mathbf{r})$, referred to as the KS orbitals. To obtain these, we note that Eq. (2.14) must be stationary with respect to variations in density, in light of Eq. (2.10). Hence, these equations apply to the ground-state of our system. We vary $n(\mathbf{r})$ subject to the constraint the KS orbitals remain orthonormal. By Eq. (2.11), this also ensures that $\int d^3r\ n(\mathbf{r}) = N$, i.e., that particle number is conserved. Lagrange multipliers ϵ_i are introduced as they were in HF theory, and we find:

$$\left(-\frac{1}{2}\nabla^2 + V(\mathbf{r}) + \int d^3r'\ \frac{n(\mathbf{r}')}{|\mathbf{r}-\mathbf{r}'|} + V_{xc}(\mathbf{r})\right)\phi_i(\mathbf{r}) = \epsilon_i\phi_i(\mathbf{r}), \tag{2.15}$$

with the exchange-correlation potential given by

$$V_{xc}(\mathbf{r}) \equiv \delta E_{xc}[n(\mathbf{r})]/\delta n(\mathbf{r}). \tag{2.16}$$

Again, as in HF theory, the terms other than $-\frac{1}{2}\nabla^2$ in parentheses give an effective potential in which the N electrons of our auxiliary system move. We will denote this $V_{KS}(\mathbf{r})$.

The KS equations must be solved self-consistently for the orbitals and eigenvalues ϵ_i.

Once we have done this, the system (ground-state) energy is determined by:

$$E[n(\mathbf{r})] = \sum_{i=1}^{N} \epsilon_i - \int d^3r\, n(\mathbf{r}) V_{xc}(\mathbf{r}) - \frac{1}{2} \int d^3r d^3r'\, \frac{n(\mathbf{r}) n(\mathbf{r}')}{|\mathbf{r} - \mathbf{r}'|} + E_{xc}[n(\mathbf{r})]. \tag{2.17}$$

Hence, as is the case in HF theory, care must be taken when interpreting our Lagrange multipliers ϵ_i as 'energies'.

This approach to DFT − through the formulation and solution of the KS equations − is one of the most widely used approaches to practical DFT today.

2.5 Choice of the exchange-correlation functional

As with the total energy functional, the analytic dependence of the exchange-correlation functional on the density $n(\mathbf{r})$ is unknown, and so it needs to be approximated in some meaningful way for DFT to be implemented. We discuss some of the significant exchange-correlation functionals used in DFT in the following sections.

It is convenient to write the exchange-correlation energy as [1]:

$$E_{xc}[n(\mathbf{r})] = \int d^3r\, n(\mathbf{r}) \epsilon_{xc}[\mathbf{r}, n(\mathbf{r})], \tag{2.18}$$

with $\epsilon_{xc}[\mathbf{r}, n(\mathbf{r})]$ representing an exchange-correlation energy per particle. The dependence of ϵ_{xc} on $n(\mathbf{r})$ means that ϵ_{xc} is not the same as $V_{xc}(\mathbf{r}) = \delta E_{xc}[n(\mathbf{r})]/\delta n(\mathbf{r})$.

2.5.1 The Local Density Approximation

Consider the interacting homogeneous electron gas (HEG). As a straightforward approximation to $\epsilon_{xc}[n(\mathbf{r})]$, one might consider that its value is given, at each point $\mathbf{r}$, by ϵ_{xc} for a homogeneous electron gas of the same density: $\epsilon_{xc}[n(\mathbf{r})] = \epsilon_{xc}^{\mathrm{HEG}}[n(\mathbf{r})]$. This is known as the Local Density Approximation (LDA).

We introduce the local Seitz radius:

$$r_s = \left(\frac{3}{4\pi n(\mathbf{r})} \right)^{1/3}, \tag{2.19}$$

and split $\epsilon_{xc}^{\mathrm{HEG}}[n(\mathbf{r})]$ for the HEG into the sum of exchange and correlation energies per particle: $\epsilon_{xc}^{\mathrm{HEG}} = \epsilon_x^{\mathrm{HEG}} + \epsilon_c^{\mathrm{HEG}}$. HF theory gives $\epsilon_x^{\mathrm{HEG}}$ exactly: [9, 12]:

$$\epsilon_x^{\mathrm{HEG}} = -\frac{\frac{3}{4\pi} \left(\frac{9\pi}{4} \right)^{1/3}}{r_s}. \tag{2.20}$$

However, $\epsilon_c^{\mathrm{HEG}}$ is not known analytically except in the limits of very low and very high

density, where we find [9]:

$$\epsilon_c^{\mathrm{HEG}} = \begin{cases} a_1/r_s + a_2/{r_s}^{3/2} + a_3/r_s^2 + ..., & r_s \to \infty, \\ a_4 \ln(r_s) + a_5 + a_6 r_s \ln(r_s) + a_7 r_s + ..., & r_s \to 0, \end{cases} \tag{2.21}$$

for constants a_1 through a_7.

At arbitrary densities, $\epsilon_c^{\mathrm{HEG}}$ can be calculated using Quantum Monte-Carlo (QMC) methods. Within the framework and any approximations of QMC, the results of such calculations are expected to be accurate. Benchmark calculations of the HEG using this method were performed by Ceperley and Alder [13]. To obtain a useful functional for ϵ_{xc}, it is helpful to use an analytic formula that interpolates these calculated values and reproduces the known limits in Eq. (2.21). One such example is the parameterisation of Perdew and Zunger [14]:

$$\epsilon_{xc}[n(\mathbf{r})] = \begin{cases} -0.4582/r_s - 0.1423/(1 + 1.0529\sqrt{r_s} + 0.3334 r_s), & r_s \geq 1, \\ -0.4582/r_s - 0.0480 + 0.0311 \ln(r_s) - 0.0116 r_s + 0.0020 r_s \ln(r_s), & r_s \leq 1. \end{cases} \tag{2.22}$$

The reader may refer to Appendix B of Martin [9] for alternative parameterisations.

The LDA turns out to be quite accurate as an approximation, even though on the face of it we expect it to only be valid for slowly-varying densities. Part of the reason for this are particular properties of the exchange-correlation hole function which are satisfied by the LDA - we touch briefly on this in Sec. 2.5.3. The self-energy cancellation (note (2) of Sec. 2.4) is only partial in the LDA.

2.5.2 Gradient-corrected functionals

The goal of gradient-corrected functionals, or generalised gradient approximations (GGAs) is to introduce some dependence of the exchange-correlation energy on the gradient of the density. In doing so we expect to be able to better account for the exchange-correlation energy of a gas of electrons with inhomogeneous density.

For an electron gas of high but slowly-varying density, Ma and Brueckner [15] have shown analytically that the HEG correlation energy $\epsilon_c^{\mathrm{HEG}}$ can be corrected by adding:

$$\Delta\epsilon_c[n(\mathbf{r})] = 0.0042349 \int d^3r \frac{|\nabla n(\mathbf{r})|^2}{n(\mathbf{r})^{4/3}} [1 + O(n(\mathbf{r})^{-1/3} \ln(n(\mathbf{r}))) + O(n(\mathbf{r})^{-1/3})]. \tag{2.23}$$

Results such as these are used as benchmarks for GGAs. For example, the Perdew-Burke-Ernzerhof (PBE) form of the exchange-correlation functional [16] modifies the

LDA correlation energy by writing:

$$E_c[n(\mathbf{r})] = \int d^3r\, n(\mathbf{r})\, [\epsilon_c^{\mathrm{HEG}} + H(r_s, t)]\,, \tag{2.24}$$

with r_s as in Eq. (2.19), and t the quantity

$$t = \frac{1}{4}\left(\frac{\pi}{3}\right)^{1/6} \frac{|\nabla n(\mathbf{r})|}{n(\mathbf{r})^{7/6}}, \tag{2.25}$$

which encapsulates the gradient dependence of this functional. The function $H(r_s, t)$ is chosen to reproduce the result of Eq. (2.23) in the limit $t \to 0$, among other conditions.

The PBE functional modifies the HEG exchange energy by introducing first a slightly different gradient density variable than Eq. (2.25), namely:

$$s = \frac{|\nabla n(\mathbf{r})|}{2(3\pi^2)^{1/3} n(\mathbf{r})^{4/3}} \tag{2.26}$$

and then writing

$$E_x[n(\mathbf{r})] = \int d^3r\, n(\mathbf{r}) \epsilon_x^{\mathrm{HEG}} F_X(s). \tag{2.27}$$

The function $F_X(s)$ depends only on the gradient (or inhomogeneity) of the density, and we expect $F(s = 0) = 1$, i.e., the LDA exchange energy is recovered in the limit of a homogeneous density. Its exact functional form is determined by various conditions; for example, it is known that $F_X(s)$ depends quadratically on s in the limit of small s. The form for the PBE functional is:

$$F_X(s) = 1.804 - \frac{0.804}{1 + 0.273022 s^2}. \tag{2.28}$$

Broadly speaking, the PBE functional is expected to give more accurate energies than the LDA, since it was designed to satisfy only exact conditions that make a significant contribution to the total energy [16].

There are many different GGAs available which employ different functional forms. A useful way of comparing GGA functionals is to examine the forms they use for $F_X(s)$; this quantity is referred to as the *(exchange) enhancement factor* as it refers to the extent to which the given GGA enhances exchange over straightforward local exchange. We provide such a comparison in Fig. 2.1 for the Becke-88 (B88) [17], Perdew-Wang (PW91) [18], Perdew-Burke-Ernzerhof (PBE) [16], Wu-Cohen (WC) [19] and PBEsol [20] functionals. The enhancement factors certainly have different large-s behaviour (e.g., comparing the B88 and PW91 functionals), but it is worth noting that we do not generally encounter arbitrarily large density gradients in real materials or solids; as a rule of thumb the 'interesting range' for s is $0 \lesssim s \lesssim 3$ [19].

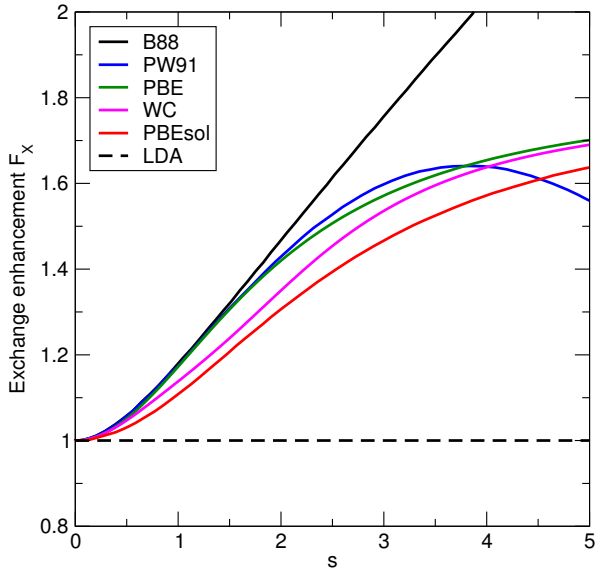

Figure 2.1: Comparison of exchange enhancement factors $F_X(s)$ (see Eq. (2.27)) for different GGA functionals as a function of the density gradient s (Eq. (2.26)). Gradients in the range $0 \lesssim s \lesssim 3$ are those typically encountered in solids. We adapt the B88 and PBEsol curves from Fig. 1 of Sun *et al.* [21], the PW91 curve is taken from Fig. 1 of Tran *et al.* [22], and the PBE and WC curves are drawn from their equations in [16] (i.e., Eq. (2.28)) and [19], respectively.

2.5.3 The return of Hartree-Fock: hybrid functionals

In Hartree-Fock theory, we already have an expression for exchange in terms of the HF orbitals - the 'Exchange terms' in Eq. (2.4). Let us denote those terms by E_X^{HF}. Can we use E_X^{HF} to construct a density functional, with Kohn-Sham orbitals now in place of HF orbitals? The answer is yes, and the class of *hybrid functionals* refers to those that incorporate some degree of this Hartree-Fock exchange. Typically, these functionals also use formulae for exchange and correlation taken from the LDA or other GGA-type functionals, in addition to HF exchange.

The motivation for incorporating HF exchange in a density functional is outlined by Becke [23] and appeals to the so-called *adiabatic connection formula*. We introduce this formula as follows. Let $\lambda \in [0, 1]$ be a continuous parameter, and consider the Hamiltonian:

$$H = T + V_\lambda + \lambda U. \tag{2.29}$$

This is a modified version of the electronic Hamiltonian Eq. (2.2), where the strength of electron-electron interactions (U) is scaled by λ. We denote the eigenfunctions of Eq. (2.29) by $|\Psi_\lambda\rangle$. The extra potential V_λ in (2.29) is defined so that the density that stems from $|\Psi_\lambda\rangle$ is equal to the density when $\lambda = 1$, which we take to correspond to the fully interacting system: $V_{\lambda=1}$ is the external potential (e.g., the nuclear potential $V_{nuc}(\mathbf{r})$ in Eq. (2.2)) and $|\Psi_{\lambda=1}\rangle$ is then the full many-body wavefunction. When $\lambda = 0$, we have a completely non-interacting system − our Kohn-Sham system − where $V_{\lambda=0}$

equals the Kohn-Sham potential V_{KS}, and $|\Psi_{\lambda=0}\rangle$ is just a Slater determinant of Kohn-Sham orbitals. We can apply perturbation theory to determine the change in energy dE_λ resulting from a small change in λ in Eq. (2.29), and in this way 'connect' the energies of fully interacting and Kohn-Sham systems via [24, 25]:

$$E_1 - E_0 = \int_0^1 dE_\lambda \tag{2.30}$$

$$= \int n(\mathbf{r})(\underbrace{V_{\lambda=1}(\mathbf{r}) - V_{\lambda=0}(\mathbf{r})}_{=V-V_{KS}})\, d^3r + \int_0^1 \langle\Psi_\lambda|\frac{1}{|\mathbf{r}-\mathbf{r}'|}|\Psi_\lambda\rangle\, d\lambda. \tag{2.31}$$

Given that the non-interacting system has $E_0 = T + \int n(\mathbf{r})V_{KS}(\mathbf{r})\, d^3r$, we arrive at an expression for the fully interacting energy E_1:

$$E_1 = T + \int n(\mathbf{r})V(\mathbf{r})\, d^3r + \int_0^1 \langle\Psi_\lambda|\frac{1}{|\mathbf{r}-\mathbf{r}'|}|\Psi_\lambda\rangle\, d\lambda \tag{2.32}$$

Comparing this to Eq. (2.14) leads to the following formula for the exchange-correlation energy:

$$E_{xc}[n(\mathbf{r})] = \int_0^1 \langle\Psi_\lambda|\frac{1}{|\mathbf{r}-\mathbf{r}'|}|\Psi_\lambda\rangle\, d\lambda - \frac{1}{2}\int \frac{n(\mathbf{r})n(\mathbf{r})}{|\mathbf{r}-\mathbf{r}'|}\, d^3r\, d^3r'. \tag{2.33}$$

We have given here the version of this connection formula as per Perdew *et al.* [25]. Other versions, such as that due to Becke [24], rewrite the expectation value in the first term of Eq. (2.33) in terms of an *exchange-correlation hole function* $h_{XC}(\mathbf{r}, \mathbf{r}')$, which gives a measure of the probability of finding an electron of a given spin at $\mathbf{r}$ and a second electron (possibly of different spin) at $\mathbf{r}'$. Studies of the properties of the hole function $h_{XC}(\mathbf{r}, \mathbf{r}')$ have helped explain the success of approximations such as the LDA and other functionals; for example it is found that these functionals satisfy certain exact properties of the exchange-correlation hole.

With Eq. (2.33) in mind, Becke [23] proposed that the integral over λ be simply approximated by its average value at the endpoints, thus writing:

$$E_{xc}[n(\mathbf{r})] = \sum_{\lambda=1,2} \frac{1}{2}\left(\langle\Psi_0|\frac{1}{|\mathbf{r}-\mathbf{r}'|}|\Psi_0\rangle - \frac{1}{2}\int \frac{n(\mathbf{r})n(\mathbf{r})}{|\mathbf{r}-\mathbf{r}'|}\, d^3r\, d^3r'\right). \tag{2.34}$$

For the case $\lambda = 0$ (the non-interacting case), the term in parentheses is simply E_X^{HF}, the HF exchange energy. Becke further proposed that the $\lambda = 1$ case (fully interacting) be simply approximated by some existing density functional (LDA, GGA), thereby creating a functional [25]:

$$E_{xc} = \frac{1}{2}E_X^{\mathrm{HF}} + \frac{1}{2}E_{xc}^{\mathrm{DFA}}, \tag{2.35}$$

where DFA is an existing density functional.

Subsequent work has given different formulae incorporating different amounts of exchange, correlation and HF exchange; for example Perdew *et al.* [25] proposed the form:

$$E_{xc} = E_{xc}^{\mathrm{DFA}} + \frac{1}{4}(E_X^{\mathrm{HF}} - E_x^{\mathrm{DFA}}), \tag{2.36}$$

based on calculated atomisation energies.

In this thesis, we have made use of the class of hybrid functionals proposed by Heyd, Scuseria and Ernzerhof (HSE) [26]. Heyd *et al.* use a splitting of the Coulomb interaction into short and long-range parts:

$$\frac{1}{|\mathbf{r}-\mathbf{r}'|} = \frac{\mathrm{erfc}(\omega|\mathbf{r}-\mathbf{r}'|)}{|\mathbf{r}-\mathbf{r}'|} + \frac{\mathrm{erf}(\omega|\mathbf{r}-\mathbf{r}'|)}{|\mathbf{r}-\mathbf{r}'|} \equiv \text{Short range (SR)} \; + \; \text{Long range (LR)}, \tag{2.37}$$

where erf and erfc are the error and complementary error functions, respectively, and ω controls the divide between short and long ranges. The HSE functional is then:

$$E_{xc}^{\mathrm{HSE}} = aE_X^{\mathrm{HF,SR}}(\omega) + (1-a)E_x^{\mathrm{PBE,SR}}(\omega) + E_x^{\mathrm{PBE,LR}}(\omega) + E_c^{\mathrm{PBE}}, \tag{2.38}$$

where a is a parameter. Specifically, we employ the HSE06 version of this functional, where $a = \frac{1}{4}$ and $\omega = 0.11$ [27]. The range separation for the HF exchange terms $E_X^{\mathrm{HF,SR}}(\omega)$ is accomplished with the replacement $1/|\mathbf{r}-\mathbf{r}'| \longrightarrow \mathrm{erfc}(\omega|\mathbf{r}-\mathbf{r}'|)/|\mathbf{r}-\mathbf{r}'|$ in E_X^{HF}. The range separation for PBE exchange is slightly trickier; this is carried out by scaling the exchange hole for the PBE functional (also using an error function), and then using this to recalculate the enhancement factor $F_X(s)$ of Eq. (2.28) for the PBE functional in the case of short or long ranges.

The use of hybrid functionals presents a difficulty when it comes to determining the Kohn Sham potential $V_{KS}(\mathbf{r})$. Because hybrid functionals depend explicitly on the KS orbitals (and only implicitly on the density), the functional derivative in Eq. (2.16) is not straightforward to carry out. There are a couple of options in this case. Formal manipulations using the chain rule can be used to express the exchange-correlation potential in terms of three alternative quantities: (i) $\delta E_{xc}/\delta\phi_i(\mathbf{r})$, the functional derivative of E_{xc} with respect to the KS orbitals, (ii) $G_i(\mathbf{r},\mathbf{r}')$, the one-electron Green's function corresponding to the orbital $\phi_i(\mathbf{r})$, and lastly (iii) the inverse of the density-response function $\chi^{-1}(\mathbf{r},\mathbf{r}')$ [28]. However, calculation of these quantities, particularly the inversion of the density-response function, is computationally demanding and numerically difficult to carry out. A further option is to allow the Kohn-Sham potential to be *nonlocal*, so that its action on an orbital will in general involve an integral over all space. Ref. [29] discusses some of these issues in further detail.

2.6 Forces, stress and structural relaxation

Techniques for calculating the forces on atomic nuclei, and methods for relaxing these forces to zero (and subject to fixed pressure constraints) are important tools in first principles calculations. As a central theme of this thesis is structure searching, we will often be dealing with new and unexpected structures that are not in equilibrium and need structural relaxation. Relaxed structures are also a prerequisite for other classes of calculations, such as those needed for determining the spectrum of phonons in a given structure.

The force acting on nucleus α at position $\mathbf{r}_\alpha$ is:

$$\mathbf{F}_\alpha = -\frac{\partial E}{\partial \mathbf{r}_\alpha}, \tag{2.39}$$

where E is the total energy. Evaluation of Eq. (2.39) can be done as follows. Let H be the electronic Hamiltonian of Eq. (2.2), and $|\Psi\rangle$ be an eigenstate of H. Then:

$$\begin{aligned}
\mathbf{F}_\alpha &= -\langle\Psi|\frac{\partial H}{\partial \mathbf{r}_\alpha}|\Psi\rangle - \langle\frac{\partial \Psi}{\partial \mathbf{r}_\alpha}|H|\Psi\rangle - \langle\Psi|H|\frac{\partial \Psi}{\partial \mathbf{r}_\alpha}\rangle - \frac{\partial E_{II}}{\partial \mathbf{r}_\alpha} \\
&= -\langle\Psi|\frac{\partial V_{nuc}(\mathbf{r})}{\partial \mathbf{r}_\alpha}|\Psi\rangle - \frac{\partial E_{II}}{\partial \mathbf{r}_\alpha} \\
&= -\int n(\mathbf{r})\frac{\partial V_{nuc}(\mathbf{r})}{\partial \mathbf{r}_\alpha}\, d^3r - \frac{\partial E_{II}}{\partial \mathbf{r}_\alpha}.
\end{aligned} \tag{2.40}$$

Going from the first equality to the second, the middle two terms on the RHS can be rewritten simply as $-E(\partial/\partial \mathbf{r}_\alpha)\langle\Psi|\Psi\rangle$ since $H|\Psi\rangle = E|\Psi\rangle$, and this is zero if $|\Psi\rangle$ is normalised [30]. Additionally, $V_{nuc}(\mathbf{r})$ is the only term in H that depends on the nuclear coordinates $\mathbf{r}_\alpha$, but we must re-introduce E_{II} (see the discussion preceding Eq. (2.2)) as this also depends on $\mathbf{r}_\alpha$. The third equality uses Eq. (2.11).

The straightforward interpretation of this is that once we have calculated $n(\mathbf{r})$ (for example using DFT), the forces are then able to be calculated from this density, at little extra cost. This statement is usually referred to as the *Hellmann-Feynman* theorem, or simply the *force* theorem [9].

Given a strain $\epsilon_{\alpha\beta}$, the stress tensor can be calculated from:

$$\sigma_{\alpha\beta} = -\frac{1}{V}\frac{\partial E}{\partial \epsilon_{\alpha\beta}}, \tag{2.41}$$

where V is the system volume. As explained in Neilson and Martin [31], the effect of a symmetric strain $\epsilon_{\alpha\beta}$ is 'felt' by a wavefunction $\Psi(\mathbf{r})$ as a rescaling of is coordinates, through the transformation $r_{i\alpha} \to r_{i\alpha} + \sum_\beta \epsilon_{\alpha\beta} r_{i\beta}$. Adjusting $\Psi(\mathbf{r})$ in this way and then calculating $E = \langle\Psi|H|\Psi\rangle$ allows us to use Eq. (2.41) to derive expressions for $\sigma_{\alpha\beta}$. These are more involved than for the forces, and contain contributions to stress from the kinetic energy, ion-electron and ion-ion interactions, the Hartree potential and the

exchange-correlation potential [31, 32, 33].

The final quantity for this section that we are interested in is the pressure, given by:

$$P = -\frac{1}{3}(\sigma_{11} + \sigma_{22} + \sigma_{33}). \tag{2.42}$$

The total energy E is a function of the nuclear positions $\mathbf{r}_\alpha$ only in the BO approximation. Relaxing a given structure is the process of moving the nuclei around so that E is minimised, i.e., so that

$$\frac{\partial E}{\partial r_{i\alpha}} = 0, \quad \text{for all nuclei } \alpha. \tag{2.43}$$

A corollary of this is that the forces on all nuclei are then zero by Eq. (2.39).

There are several techniques by which a function such as $E(\{\mathbf{r}_\alpha\})$ can be minimised with respect to its variables. In this thesis, all such minimisations have made use of the Broyden-Fletcher-Goldfarb-Shanno (BFGS) algorithm [34]. This algorithm proceeds by assuming a second-order Taylor expansion for E:

$$E(r_{i\alpha} + \Delta r_{i\alpha}) = E(r_{i\alpha}) + \sum_{i\alpha} \nabla E(\mathbf{r})|_{r_{i\alpha}} \Delta r_{i\alpha} + \frac{1}{2} \sum_{i\alpha,j\beta} \Delta r_{i\alpha} \mathbf{H}_{i\alpha,j\beta} \Delta r_{j\beta}, \tag{2.44}$$

where $\mathbf{H}_{i\alpha,j\beta}$ is the Hessian matrix, with elements:

$$\mathbf{H}_{i\alpha,j\beta} = \frac{\partial^2 E}{\partial r_{i\alpha} \partial r_{j\beta}}. \tag{2.45}$$

We then aim to (locally) minimise E with respect to $\Delta r_{i\alpha}$. The quantity $\nabla E(\mathbf{r})|_{r_{i\alpha}}$ is calculatable, being just the forces, but the Hessian is treated as an unknown quantity which is initialised and then iteratively updated as the algorithm progresses.

2.7 Phonons: putting the nuclear motion back

We neglected the kinetic energy of the nuclei in making the Born-Oppenheimer approximation. However, this energy can be important, for example if we are considering two different crystal structures lying very close in energy. Accounting for nuclear motion also allows us to calculate phonon dispersion relations, which can be compared to (for example) experimental inelastic neutron scattering studies. Finally, nuclear motion also allows us to explore the thermodynamic properties of a structure.

The energy eigenvalues of the electronic Hamiltonian Eq. (2.2) depend parametrically on the nuclear coordinates: $E = E(\mathbf{r}_\alpha)$. Assuming we have solved the electronic problem (i.e., determined E), we can write down a Hamiltonian describing the motion

of our M nuclei under the influence of the field generated by the N electrons:

$$H = \left(\sum_{\alpha=1}^{M} -\frac{1}{2M_\alpha} {\nabla_\alpha}^2 \right) + E(\mathbf{r}_\alpha : \alpha = 1, 2, ..., M). \tag{2.46}$$

Although it is possible to calculate $E(\mathbf{r}_\alpha)$ for arbitrary nuclear positions $\mathbf{r}_\alpha$, the functional dependence of E on these parameters is not always explicitly known.

However, if the nuclei are assumed to undergo *small* displacements, we can expand E in a Taylor series in those displacements. We introduce the notation $r_{(p\alpha)i}$ to denote the i-th Cartesian component of the position of nucleus α. An extra index p, meaning 'primitive cell', is added here for the case of periodic systems, and is used to label the cell inside which nucleus α resides; this is not required for isolated systems. The Taylor series for E is then:

$$\begin{aligned} E(r_{(p\alpha)i} + \Delta r_{(p\alpha)i}) = E(r_{(p\alpha)i}) &+ \sum_{p\alpha i} \frac{\partial E}{\partial r_{(p\alpha)i}} \Delta r_{(p\alpha)i} \\ &+ \frac{1}{2} \sum_{p\alpha i} \sum_{p'\alpha' i'} \frac{\partial^2 E}{\partial r_{(p\alpha)i} \partial r_{(p'\alpha')i'}} \Delta r_{(p\alpha)i} \Delta r_{(p'\alpha')i'} \\ &+ \text{ Higher order terms,} \end{aligned} \tag{2.47}$$

where the sums are carried out over all primitive cells p (of which there are infinitely many), all nuclei α (M in total) and all Cartesian directions i.

We usually restrict ourselves to the case where the positions $r_{(p\alpha)i}$ of the nuclei correspond to a relaxed structure, i.e., where all forces on the nuclei are zero, so that the first-order term in Eq. (2.47) is then also zero. This is the main difference between the expansions of Eqs. (2.44) and (2.47): the former is not expanded about an equilibrium point.

2.7.1 Harmonic phonons

Specialising further, and retaining terms up to second order only in Eq. (2.47), gives us a theory of *harmonic* phonons [10].

To understand the resulting nuclear motion in this case, we proceed by simply writing down the classical equations of motion for the nuclei. We use the notation:

$$\Phi_{ii'}(p\alpha, p'\alpha') = \frac{\partial^2 E}{\partial r_{(p\alpha)i} \partial r_{(p'\alpha')i'}} \tag{2.48}$$

for the second derivatives of E; $\Phi_{ij}(p\alpha, p'\alpha')$ are referred to as the (interatomic) *force*

constants [35]. We then have:

$$M_\alpha \frac{d^2 \Delta r_{(p\alpha)i}}{dt^2} = -\frac{\partial E}{\partial \Delta r_{(p\alpha)i}} = -\sum_{p'\alpha' i'} \Phi_{ii'}(p\alpha, p'\alpha') \Delta r_{(p'\alpha')i'}. \tag{2.49}$$

We further assume a harmonic or wave-like solution to this equation for the nuclear displacements $\Delta r_{(p\alpha)i}$ of the form:

$$\Delta r_{(p\alpha)i} = \frac{A_{\alpha i}(\mathbf{q})}{\sqrt{M_\alpha}} \exp[i(\mathbf{q}.\mathbf{r}_p - \omega t)], \tag{2.50}$$

where $\mathbf{r}_p$ is the position of the origin of the p-th primitive cell, $\mathbf{q}$ a wavevector, and $A_{\alpha i}(\mathbf{q})$ the amplitude of the displacements, scaled by $\sqrt{M_\alpha}$. This amplitude does not depend on the primitive cell p. Maradudin and Vosko [36] provide a detailed symmetry-based analysis as to the origin of Eq. (2.50); this essentially relies on the fact that the interatomic force constants of Eq. (2.48) are unchanged upon the addition of an integer L to both p and p', due to translational symmetry in periodic structures. Substituting this into Eq. (2.49) gives:

$$\begin{aligned} -M_\alpha\, \omega^2 \frac{A_{\alpha i}(\mathbf{q})}{\sqrt{M_\alpha}} &= -\sum_{p'\alpha' i'} \Phi_{ii'}(p\alpha, p'\alpha') \frac{A_{\alpha' i'}(\mathbf{q})}{\sqrt{M_{\alpha'}}} \exp[i\mathbf{q}.(\mathbf{r}_{p'} - \mathbf{r}_p)] \\ \implies \omega^2 A_{\alpha i}(\mathbf{q}) &= \sum_{\alpha' i'} \left(\frac{1}{\sqrt{M_\alpha M_{\alpha'}}} \sum_{p'} \Phi_{ii'}(p\alpha, p'\alpha') \exp[i\mathbf{q}.(\mathbf{r}_{p'} - \mathbf{r}_p)] \right) A_{\alpha' i'}(\mathbf{q}). \end{aligned} \tag{2.51}$$

The quantity in parentheses is referred to as the *dynamical matrix*:

$$D_{ii'}(\alpha, \alpha'; \mathbf{q}) = \frac{1}{\sqrt{M_\alpha M_{\alpha'}}} \sum_{p'} \Phi_{ii'}(p\alpha, p'\alpha') \exp[i\mathbf{q}.(\mathbf{r}_{p'} - \mathbf{r}_p)], \tag{2.52}$$

which is, as per the discussion above, independent of p. We can for example set $p = 0$ as our 'reference cell', and let $\mathbf{r}_p$ simply be the origin of our coordinate system [35]. The sum implied in Eq. (2.52), and the presence of the complex exponential means that the dynamical matrix is usually described as the (spatial) Fourier transform of the interatomic force constants $\Phi_{ii'}(p\alpha, p'\alpha')$.

The values of $D_{ii'}(\alpha, \alpha'; \mathbf{q})$ can be organised into a square $3N \times 3N$ matrix [10], and Eq. (2.51) becomes an eigenvalue problem [37]:

$$\sum_{\alpha' i'} D_{ii'}(\alpha, \alpha'; \mathbf{q}) A_{\alpha' i' \nu}(\mathbf{q}) = \omega_\nu(\mathbf{q})^2 A_{\alpha i \nu}(\mathbf{q}). \tag{2.53}$$

We hence find that the vibrational frequencies ω of Eq. (2.50) can be obtained from the *eigenvalues* of the dynamical matrix; the index ν ranges from 1 to $3N$ and enumerates these eigenvalues. The (scaled) amplitudes $A_{\alpha i}$ of Eq. (2.50) are the corresponding

eigenvectors, and represent the normal modes of vibration.

The thrust of the above analysis is therefore the following: under the action of a harmonic potential, nuclei undergo motion which can be decomposed into $3N$ normal modes of vibration, whose amplitudes and frequencies are governed by the eigenvectors and eigenvalues respectively of the dynamical matrix.

The fact that the dynamical matrix eigenvalues are actually $\omega_\nu(\mathbf{q})^2$ indicates that, for $\omega_\nu(\mathbf{q})$ to be real, they must be positive. When this is not the case, we are said to have *imaginary* or 'negative' phonon frequencies, and it indicates that a particular phonon normal mode (displacement of nuclei) can lower the lattice energy. This, in turn, can indicate an instability in our equilibrium structure, and also means that our analysis in the following thermodynamics section cannot be used.

2.7.2 Thermodynamics

The analysis leading to the dynamical matrix in the previous section is essentially classical, and at this point we apply quantum and statistical mechanics to access thermodynamic properties. The vibrating nuclei are treated as a set of $3N$ harmonic oscillators, with frequencies given by the dynamical matrix. The partition function Z describing our system can be calculated from the known quantum harmonic oscillator energy levels, and from this, typical thermodynamic relations give us the phonon free energy F, internal energy U and phonon pressure P:

$$F = -\frac{1}{\beta}\log(Z), \quad U = -\frac{\partial}{\partial\beta}\log(Z), \quad P = -\left(\frac{\partial F}{\partial V}\right)_T, \quad \beta = \frac{1}{k_B T}. \tag{2.54}$$

In the case of a periodic solid, the free energy is explicitly:

$$F_{phon} = \frac{1}{2}\sum_{\nu=1}^{3N}\frac{1}{\Omega_{\text{BZ}}}\int \omega_\nu(\mathbf{q})\, d^3q + k_B T \sum_{\nu=1}^{3N}\frac{1}{\Omega_{\text{BZ}}}\int \ln(1-\exp(-\omega_\nu(\mathbf{q})/k_B T))\, d^3q, \tag{2.55}$$

where k_B is Boltzmann's constant and T the temperature. The integration is carried out over the Brillouin zone, which has (reciprocal-space) volume Ω_{BZ}. The first term here, which is the only one surviving for $T = 0$, is the usual zero-point energy. We comment that for calculation purposes, integrals over the Brillouin zone in Eq. (2.55) are replaced with finite sums on grids of q-points. We will meet this concept again in Section 2.8.3.

2.7.3 Beyond the harmonic approximation

We clarify a minor point of terminology here before discussing ways of going beyond the harmonic approximation. So far, we have used the term 'harmonic approximation' to refer to the truncation of Eq. (2.47) to quadratic order. This terminology is sometimes

instead used to refer to the *quasiharmonic approximation* (QHA), which is a separate but distinct approximation that stems from assuming the harmonic approximation applies at each volume V. We discuss the QHA in much more detail when we come to apply it; see for example Sec. 4.5.3.

There are cases when the truncation of Eq. (2.47) to harmonic order is not accurate, and we need to consider *anharmonicity*. This is usually the case in systems with light atoms, which can be expected to vibrate further from their equilibrium positions, or in systems at high temperature. There are a few options available in these cases.

One possibility is to simply keep more terms in Eq. (2.47), as done in Ref. [38]; however, the number of terms that need to be calculated in that equation grows quickly with the number of higher order terms. The stochastic self-consistent harmonic approximation (SSCHA) method of Errea, Calandra and Mauri [39] instead minimises the energy of a trial harmonic Hamiltonian; the effects of anharmonicity are thus included in the trial Hamiltonian. The vibrational self-consistent field (VSCF) approach of Monserrat *et al.* [40] is a further option: in this method, operators (such as energy) are expanded in normal-mode coordinates. Finally, anharmonicity can also been addressed using path-integral molecular dynamics [41].

2.7.4 Practical calculation schemes

If we want to access the phonon frequencies $\omega_\nu(\mathbf{q})$ of Eq. (2.53), we need a practical scheme to accomplish one of two things: (i) calculation of all relevant interatomic force constants (Eq. (2.48)), from which the dynamical matrix can then be constructed (Eq. (2.52)) and diagonalised to yield the $\omega_\nu(\mathbf{q})$, or (ii) some method for determining the dynamical matrix directly, and then diagonalising it.

We discuss option (i) first. Note that first derivatives of the energy E are relatively straightforward to calculate through the Hellmann-Feynman theorem – see Section 2.6 – but second derivatives of E are more involved. In the *direct* or *supercell* method, which is the method we use in this thesis, the force constants $\Phi_{ii'}(p\alpha, p'\alpha')$ are computed by direct displacement of the nuclei, and the second derivative is calculated numerically [42].

Let u be a small displacement, which we apply to nucleus α located in cell p along the Cartesian direction i, so that $\Delta r_{(p\alpha)i} = u$ and all other nuclei are undisplaced. Then we have:

$$\Phi_{ii'}(p\alpha, p'\alpha') = \frac{\partial^2 E}{\partial r_{(p\alpha)i} \partial r_{(p'\alpha')i'}} \approx \frac{1}{2u} \left(\frac{\partial E}{\partial r_{(p'\alpha')i'}}\bigg|_{\Delta r_{(p\alpha)i}=u} - \frac{\partial E}{\partial r_{(p'\alpha')i'}}\bigg|_{\Delta r_{(p\alpha)i}=-u} \right). \tag{2.56}$$

This provides a practical scheme to calculate $\Phi_{ii'}(p\alpha, p'\alpha')$: we impose the displacement $\Delta r_{(p\alpha)i} = u$ on our system, and calculate the force (first energy derivative) on nucleus

$(p'\alpha')$ in the i'-direction. This is repeated for a displacement of $-u$. Since we are evaluating the second derivative numerically, we could principle calculate it from a single small displacement, but Eq. (2.56) is numerically more accurate. In practical calculations, the displacement u is of the order 0.01 bohr.

There are two related difficulties with carrying this out in practice. First, there are in principle an infinite number of force constants $\Phi_{ii'}(p\alpha, p'\alpha')$, because the indices p and p' run over an infinite number of cells. The sum over p' in Eq. (2.52) is then also an infinite sum. Second, the act of displacing a nucleus in a periodic lattice means that all periodic images of that nucleus are also displaced, when working under periodic boundary conditions. This is undesirable and will affect the values obtained for the force constants.

Both of these difficulties are dealt with using supercells. The idea is this: nucleus α' in cell p' will not experience a force due to a small displacement of nucleus α in cell p, provided that cells p and p' are sufficiently far apart, so that the corresponding force constant is zero. This decay in force constant can in fact be as rapid as $1/d^5$, where d is the distance between nuclei, but it is system-dependent [43]. Hence, a supercell containing multiple copies of the original cell is constructed large enough so that the influence of a displaced nucleus at its centre has decayed sufficiently at its edges. The force constants are then determined by total energy calculations on this supercell.

In terms of option (ii) discussed at the beginning of this section, the dynamical matrix $D_{ii'}(\alpha, \alpha'; \mathbf{q})$ can be calculated at arbitrary $\mathbf{q}$ directly, without determining the force constants first, using density functional perturbation theory (DFPT) [44]. This provides another route to phonon properties - we can specify a grid of $\mathbf{q}$-points, and use DFPT to calculate $\omega_\nu(\mathbf{q})$ on this grid of points, after which calculations such as that in Eq. (2.55) for the phonon free energy can be carried out.

2.7.5 Supercell cutoff schemes

When applying the supercell method, a cutoff scheme must be used on the force constants before we use them to calculate the dynamical matrices of Eq. (2.52). We discuss how this works in the following.

We note first that the force constants we actually get from a practical supercell calculation, which we will denote by $\overline{\Phi}_{ii'}(p\alpha, p'\alpha')$, are:

$$\overline{\Phi}_{ii'}(p\alpha, p'\alpha') = \Phi_{ii'}(p\alpha, p'\alpha') + \sum_{L\neq 0} \Phi_{ii'}((p+L)\alpha, p'\alpha'), \tag{2.57}$$

because of the displacements of all periodic images of a nucleus that occur in periodic boundary condition calculations. Ye *et al.* refer to this quantity as the *cumulant* force constant (CFC) [35]. Here, we have adjusted our notation slightly so that p and p' index primitive cells only within our supercell, and L indexes entire supercells. The

calculated force constants $\overline{\Phi}_{ii'}(p\alpha, p'\alpha')$ are periodic with supercells, in the sense that for different supercells M and M', we have $\overline{\Phi}_{ii'}((p+M)\alpha, (p'+M')\alpha') = \overline{\Phi}_{ii'}(p\alpha, p'\alpha')$; this is not a property of the actual force constants $\Phi_{ii'}(p\alpha, p'\alpha')$.

In the *spherical* cutoff scheme, calculated force constants $\overline{\Phi}_{ii'}(p\alpha, p'\alpha')$ are set to zero if nuclei $p\alpha$ and $p'\alpha'$ are separated by more than a specified cutoff distance. In this case, the distance between nucleus $p\alpha$ and $p'\alpha'$ is the minimum distance between $p\alpha$ and all supercell-periodic repeats of $p'\alpha'$. The remaining non-zero force constants are then used in Eq. (2.52) in place of $\Phi_{ii'}(p\alpha, p'\alpha')$ for a calculation of the dynamical matrix, and the sum over p' in that equation is finite.

The *cumulant* cutoff scheme instead introduces an approximate dynamical matrix $\overline{D}_{ii'}(\alpha, \alpha'; \mathbf{q})$, defined by [35, 45]:

$$\overline{D}_{ii'}(\alpha, \alpha'; \mathbf{q}) = \frac{1}{\sqrt{M_\alpha M'_\alpha}} \sum_{p'} \overline{\Phi}_{ii'}(p\alpha, p'\alpha') \exp[i\mathbf{q}.(\mathbf{r}_{p'} - \mathbf{r}_p)], \tag{2.58}$$

which can then be used to calculate phonon frequencies. As before, p' is restricted to primitive cells within the supercell. This definition is in the same spirit as the spherical cutoff method, but the calculated force constants $\overline{\Phi}_{ii'}(p\alpha, p'\alpha')$ have not been spherically truncated.

Eq. (2.58) has a special advantage over the spherical cutoff method. Consider the set of wavevectors $\mathbf{q}$ that satisfy

$$\mathbf{q}.\mathbf{R}_\alpha = 2n_\alpha\pi, \quad n_\alpha \in \mathbb{Z}, \quad \alpha = 1, 2, 3, \tag{2.59}$$

where $\mathbf{R}_\alpha$ is a lattice vector of our particular supercell. Then, for such $\mathbf{q}$:

$$\begin{aligned}
\overline{D}_{ii'}(\alpha, \alpha'; \mathbf{q}) &= \frac{1}{\sqrt{M_\alpha M'_\alpha}} \sum_{p'} \overline{\Phi}_{ii'}(p\alpha, p'\alpha') \exp[i\mathbf{q}.(\mathbf{r}_{p'} - \mathbf{r}_p)] \\
&= \frac{1}{\sqrt{M_\alpha M'_\alpha}} \sum_{Lp'} \Phi_{ii'}((p+L)\alpha, p'\alpha') \exp[i\mathbf{q}.(\mathbf{r}_{p'} - \mathbf{r}_p)] \\
&= \frac{1}{\sqrt{M_\alpha M'_\alpha}} \sum_{Lp'} \Phi_{ii'}(p\alpha, (p'-L)\alpha') \exp[i\mathbf{q}.(\mathbf{r}_{p'} - \mathbf{R}_L - \mathbf{r}_p)] \\
&= D_{ii'}(\alpha, \alpha'; \mathbf{q}),
\end{aligned} \tag{2.60}$$

because a sum over all supercells L and primitive cells within each supercell p' is the same as a sum over all possible primitive cells. Here, $\mathbf{R}_L$ is a vector to the origin of the L-th supercell. Hence, for wavevectors satisfying Eq. (2.59), the approximate dynamical matrix of Eq. (2.58) is equal to the exact dynamical matrix. Such wavevectors are referred to as *commensurate*, and through the cumulant cutoff scheme, we expect to recover the exact phonon frequencies $\omega_\nu(\mathbf{q})$ at these wavevectors.[3] The cumulant

[3] An important exception are phonons at the Γ point, $\mathbf{q}$=(0,0,0). This wavevector is commensurate

cutoff scheme is the main method we have used for performing phonon frequency and related calculations in this thesis.

2.8 Plane wave density functional theory

2.8.1 Outline

We aim to give an overview of some of the practical aspects behind a solution to the KS equations (2.15). This essentially involves two main steps:

- Expanding the KS orbitals in a particular basis
- Self-consistently solving the resulting equations

In this report, our computational work has made extensive use of CASTEP [47], a FORTRAN-based code which implements the plane-wave pseudopotential approach to DFT calculations. An extensive review of this type of calculation is given by Payne *et al.* [48], which we refer to frequently in the following.

2.8.2 Basis sets

A number of options present themselves as a choice of basis for the KS orbitals: we can use for example plane waves, Slater or Gaussian atomic orbitals [49], or wavelets [50].

We discuss here the use of plane waves, which is the only basis set used in this thesis. Advantages of plane waves include:

- They are *systematic* (not overcomplete): the exact basis set limit is approached as more plane waves are used
- The delocalised nature of the waves: no Pulay forces arise (to be discussed shortly)
- Plane waves are naturally periodic: ideal for crystalline systems

The periodicity of this basis set is evidently not advantageous for looking at a non-periodic system such as an isolated molecule. This can be circumvented by embedding the system in a larger supercell, which is still periodic but where the molecule is 'padded' by vacuum [48].

The plane wave basis set is comprised of functions $\exp(i\mathbf{G}.\mathbf{r})$, with $\mathbf{G}$ a reciprocal lattice point. The density $n(\mathbf{r})$ is periodic in the lattice, and so the KS potential $V_{KS}(\mathbf{r})$ is also periodic. Hence Bloch's theorem applies to the KS orbitals $\phi_i(\mathbf{r})$, so

with any supercell. However, in systems with non-vanishing Born effective charges, the dynamical matrices at Γ have non-analytic contributions that are not fully captured by the supercell formalism [46].

these orbitals have the plane wave expansion:

$$\phi_{i,\mathbf{k}}(\mathbf{r}) = e^{i\mathbf{k}.\mathbf{r}} \sum_{\mathbf{G}} c_{i,\mathbf{G}} e^{i\mathbf{G}.\mathbf{r}} = \sum_{\mathbf{G}} c_{i,\mathbf{G}} e^{i(\mathbf{k}+\mathbf{G}).\mathbf{r}}. \tag{2.61}$$

For this expansion to be complete, the sum over $\mathbf{G}$ should be over *all* reciprocal lattice points. In practice, a finite number of plane waves must be used. We introduce a cut-off energy E_{cut}, and include a plane wave in the expansion above if

$$\frac{1}{2}|\mathbf{k}+\mathbf{G}|^2 \leq E_{cut}, \tag{2.62}$$

under the assumption that the KS orbitals have a negligible component along plane waves with a kinetic energy higher than E_{cut}. An estimate of the number of plane waves that satisfy this requirement (for a given $\mathbf{k}$) is $(\Omega/6\pi^2)(2E_{cut})^{3/2}$, where Ω is the real-space cell volume.

The choice of E_{cut} depends on the system under consideration and the type of pseudopotential (also to be discussed shortly) being used. We must therefore converge quantities such as the total energy with respect to this parameter.

Writing out the KS equations (2.15) in this basis set gives:

$$\sum_{\mathbf{G'}} \left[\frac{1}{2}|\mathbf{k}+\mathbf{G}|^2 \delta_{\mathbf{G}\mathbf{G'}} + V_{KS}(\mathbf{G}-\mathbf{G'}) \right] c_{i,\mathbf{k}+\mathbf{G'}} = \epsilon_i c_{i,\mathbf{k}+\mathbf{G}}. \tag{2.63}$$

where

$$V_{KS}(\mathbf{G}-\mathbf{G'}) = \frac{1}{\Omega} \int d^3r \; e^{-i(\mathbf{G}-\mathbf{G'}).\mathbf{r}} V_{KS}(\mathbf{r}). \tag{2.64}$$

The integral of Eq. (2.64) is over a single cell.

Thus the problem of solving the KS equations comes down to diagonalising the Hamiltonian matrix on the LHS of Eq. (2.63), yielding the plane wave expansion coefficients $c_{i,\mathbf{k}+\mathbf{G}}$ and KS orbital eigenvalues ϵ_i.

The use of basis sets presents extra considerations when it comes to calculating forces (Sec. 2.6). If we use a complete basis set (of any kind), we can obtain the exact ground-state wavefunction $|\Psi\rangle$ and the second and third terms in the first line of Eq. (2.40) will indeed vanish. In practice, we usually work with incomplete or truncated basis sets for which $|\Psi\rangle$ then becomes only an approximate wavefunction. If the basis set is *independent* of $\mathbf{r}_\alpha$, then these terms in Eq. (2.40) remain zero and we do not need to consider them. However, if we use a basis set that consists (for example) of atomic orbitals that do depend on $\mathbf{r}_\alpha$, then we must evaluate these terms. The contribution $-\langle d\Psi/d\mathbf{r}_\alpha|H|\Psi\rangle - \langle\Psi|H|d\Psi/d\mathbf{r}_\alpha\rangle$ to the calculated force is known as the *Pulay* force; Pulay himself called this the *wavefunction* force [51].

2.8.3 Sampling in k-space

With a plane-wave basis set, calculating quantities such as the total energy requires us to integrate (with respect to $\mathbf{k}$) over our simulation cell's Brillouin zone. For example, the KS eigenvalues ϵ_i can be determined at each $\mathbf{k}$ using Eq. (2.63), and the first term of Eq. (2.17) then represents an integral over the Brillouin zone:

$$\frac{1}{\Omega_{\mathrm{BZ}}} \sum_i \int d^3k \; \epsilon_i(\mathbf{k}), \tag{2.65}$$

where the sum i is carried out over the occupied KS orbitals, and Ω_{BZ} is the Brillouin zone volume.

In practice, the KS eigenvalues are calculated at a finite set of $\mathbf{k}$-points only, and integrals such as Eq. (2.65) approximated by a sum. A method of choosing which $\mathbf{k}$-points to use is therefore required. The set of $\mathbf{k}$-points:

$$\mathbf{k} = \sum_{i=1}^{3} \frac{2r_i - N_i - 1}{2N_i} \mathbf{b}_i : r_i \in \{1, 2, ..., N_i\} \tag{2.66}$$

is known as a *Monkhorst-Pack* (MP) grid [52], and is the $\mathbf{k}$-point sampling method we have used in this report. The three integers N_1, N_2 and N_3 specify the size of the grid along the three reciprocal-space lattice vectors $\mathbf{b}_1$, $\mathbf{b}_2$ and $\mathbf{b}_3$.

We can make a significant computational saving here by appealing to symmetries, if any, present in the reciprocal lattice. If a symmetry operation of the reciprocal lattice maps some of the $\mathbf{k}$-points of Eq. (2.66) onto one another, then an explicit calculation of (say) the energy is only needed at one of these $\mathbf{k}$-points.

As with the cut-off energy E_{cut}, quantities like the total energy need to be converged with respect to the number of $\mathbf{k}$-points in our grid.

2.8.4 Self-consistency

Conceptually, the most straightforward means of solving the KS equations in a basis (see for example Eq. (2.63)) is to simply write down the KS Hamiltonian in that basis and diagonalise it. There are, however, several considerations. A large basis set, which is usually required for plane waves, could generate a Hamiltonian matrix that is far too large to store in computer memory. Conventional matrix diagonalisation techniques generally give us access to the full spectrum of eigenvalues and eigenvectors, and this is unnecessary − we only require the lowest-lying eigenvalues of the KS Hamiltonian. For this reason, iterative techniques are used instead. These do not require us to store the full Hamiltonian matrix, but only require an efficient means of calculating $H|\phi\rangle$ in our basis, for arbitrary states $|\phi\rangle$. Iterative techniques include the steepest-descents (SD) and conjugate-gradient (CG) methods, which can be used to update initial guesses for the Kohn-Sham orbitals $\phi_i(\mathbf{r})$ [48].

The KS Hamiltonian is dependent on $n(\mathbf{r})$, so we need a self-consistent solution to the KS equations. Whenever the orbitals $\phi_i(\mathbf{r})$ are updated or modified using a series of SD or CG steps, the density $n(\mathbf{r})$ and KS Hamiltonian need to be recalculated to reflect this change. One way of doing this is to use a *density-mixing* scheme, where the new (recalculated) density is expressed as a function (usually a weighted sum) of densities from previous iterations. This affords numerical stability and accelerated convergence in iterative schemes [53].

2.9 Pseudopotentials

Atomic wavefunctions can oscillate considerably in the vicinity of nuclei, due to the singular nature of the Coulomb potential. Expanded in terms of plane waves, an extremely large number of waves will be needed to accurately represent these oscillations [48]. On the other hand, the region close to the atomic nuclei is home to the atom's *core* electrons. In general, an explicit treatment of core electrons isn't required, since they do not partake in chemical bonding except for example under extremes of pressure. We can account for this by replacing the core electrons and singular Coulomb potential by a smoother function: a pseudopotential. This allows a more feasible number of plane waves to be used in calculations. An illustration showing the fundamentals of the pseudopotential idea is given in Fig. 2.2.

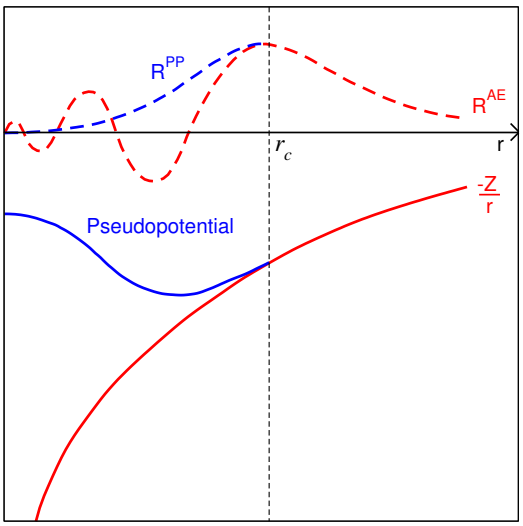

Figure 2.2: Illustration of the concept of a pseudopotential. In the presence of the strong Coulomb potential $-Z/r$, the radial component of the wavefunction R^{AE} generally contains nodes and relatively high frequency oscillations near the atomic core (left hand side of the figure), requiring a large plane wave basis set to adequately represent it. A pseudopotential replaces the Coulomb interaction in the core region with a much smoother function, giving a nodeless 'pseudo wavefunction' R^{PP} instead. A cutoff radius r_c divides the core and external regions, and the pseudo and actual wavefunctions match beyond r_c. Figure taken from Fig. 5 of Payne *et al.* [48].

In constructing a pseudopotential for a given atom, we segregate electrons into 'core'

and 'valence' with the aim of reproducing valence electron energies. A reference all-electron calculation without a pseudopotential is carried out first, usually on the atomic ground state for an isolated neutral atom, and the results are used to build the pseudopotential.

In doing this, we assume that the core wavefunctions of an isolated atom bear some resemblance to the core wavefunctions of the same atom in a molecule or solid. In fact, the kinetic energy of core states (and hence the core wavefunctions) can change by several eV in going from the isolated atom to a solid. The work of von Barth and Gellatt [54] shows that, in spite of this, the errors in the total energy arising from 'frozen' cores is small, and is only felt at second-order in the charge−pseudo charge density differences.

2.9.1 DFT in detail for a single, spherically symmetric atom

The first step in generating a pseudopotential is carrying out an all-electron calculation for the atom in question, using DFT. The pseudopotential we create will be particular to the choice of exchange correlation functional used. We solve the Kohn-Sham equations (2.15):

$$\left(-\frac{1}{2}\nabla^2 + V_{KS}(\mathbf{r})\right)\phi_i^{\mathrm{AE}}(\mathbf{r}) = \epsilon_i^{\mathrm{AE}}\phi_i^{\mathrm{AE}}(\mathbf{r}), \tag{2.67}$$

to yield all-electron (AE) Kohn-Sham orbitals $\phi_i^{\mathrm{AE}}(\mathbf{r})$ and eigenvalues ϵ_i^{AE}. The external potential $V(\mathbf{r})$ appearing in $V_{KS}(\mathbf{r})$ (see Eq. 2.15) is the full Coulombic nuclear potential for the atom at hand: $V(\mathbf{r}) = -Z/r$. We usually specialise to the case of spherical symmetry: assuming that the all-electron density $n(\mathbf{r})$ is spherically symmetric, the Hartree and exchange-correlation potentials (and hence $V_{KS}(\mathbf{r})$) are likewise spherically symmetric. Solutions to Eq. (2.67) can then be separated into radial and angular parts. We replace the reference index i with the usual nlm quantum numbers and write:

$$\phi_i^{\mathrm{AE}}(\mathbf{r}) = R_{n,l}^{\mathrm{AE}}(r)Y_{l,m}(\theta,\phi), \tag{2.68}$$

where:

$$\left(-\frac{1}{2}\frac{d^2}{dr^2} + \frac{l(l+1)}{2r^2} + V_{KS}(r)\right) rR_{n,l}^{\mathrm{AE}}(r) = \epsilon_{n,l}^{\mathrm{AE}}\, rR_{n,l}^{\mathrm{AE}}(r) \tag{2.69}$$

is the radial equation for $R_{n,l}^{\mathrm{AE}}(r)$, and $Y_{l,m}(\theta,\phi)$ are spherical harmonics. Solving Eq. (2.69) typically requires numerical methods.

The density is to be calculated from Eq. (2.11). The eigenvalues $\epsilon_{n,l}^{\mathrm{AE}}$ are independent of m ($-l \leq m \leq l$), so we can have $2(2l+1)$ (with spin) electrons at the energy $\epsilon_{n,l}^{\mathrm{AE}}$. Let us order the eigenvalues $\epsilon_{n,l}^{\mathrm{AE}}$ by energy; we then fully occupy these with $2(2l+1)$

electrons each, until we reach the highest occupied $\epsilon^{\mathrm{AE}}_{n,l}$ where we place the remaining electrons. Denoting this highest occupied energy by ϵ_N, the density is therefore [55]:

$$\begin{aligned} n(r) &= \sum_{\text{Occupied } n,l} \frac{f_{nl}}{2l+1} \sum_{m=-l}^{l} |R^{\mathrm{AE}}_{n,l}(r) Y_{l,m}(\theta,\phi)|^2 \\ &= \sum_{\text{Occupied } n,l} f_{nl} \frac{1}{4\pi} R^{\mathrm{AE}}_{n,l}(r)^2, \end{aligned} \tag{2.70}$$

where f_{nl} is an occupation number for $\epsilon^{\mathrm{AE}}_{n,l}$, equalling $2(2l+1)$ for $\epsilon^{\mathrm{AE}}_{n,l} < \epsilon_N$, and lying between 0 and $2(2l+1)$ for $\epsilon^{\mathrm{AE}}_{n,l} = \epsilon_N$. Note that the sum over m is carried out even for the energy ϵ_N in order to yield a spherically symmetry $n(r)$, even though ϵ_N may not be fully occupied with $2(2l+1)$ electrons [56].

2.9.2 Constructing a pseudopotential

We expect that the radial components $R^{\mathrm{AE}}_{n,l}(r)$ in Eq. (2.69) will contain nodes, particularly for higher angular momentum states. Our goal is to replace the all electron radial functions $R^{\mathrm{AE}}_{n,l}(r)$ with much smoother 'pseudo orbital' functions $R^{\mathrm{PP}}_{n,l}(r)$. The corresponding eigenvalue $\epsilon^{\mathrm{AE}}_{n,l}$ is to remain the same. This is carried out in practice by following some prescription (of which we will mention a couple of examples shortly) to generate $R^{\mathrm{PP}}_{n,l}(r)$ given $R^{\mathrm{AE}}_{n,l}(r)$, and then inverting the radial equation (2.69) to obtain the corresponding potential:

$$V^{\mathrm{PP}}_{scr,n,l}(r) = \epsilon^{\mathrm{AE}}_{n,l} - \frac{l(l+1)}{2r^2} + \frac{1}{2rR^{\mathrm{PP}}_{n,l}(r)} \frac{d^2}{dr^2}[rR^{\mathrm{PP}}_{n,l}] \tag{2.71}$$

$V^{\mathrm{PP}}_{scr,n,l}(r)$ replaces the all-electron Kohn-Sham potential $V_{KS}(r)$ and is referred to as a *screened pseudopotential* [55, 57]. The valence charge density is to be calculated from from the pseudo orbitals $R^{\mathrm{PP}}_{n,l}(r)$ using Eq. (2.70) with $R^{\mathrm{AE}}_{n,l}(r) \to R^{\mathrm{PP}}_{n,l}(r)$, and with the sum restricted to valence n,l pairs only, yielding a valence density $n^{\mathrm{PP}}(r)$. A couple of important features can be noted regarding Eq. (2.71): if we want the screened pseudopotential to be free of any singularities, we should avoid nodes in $R^{\mathrm{PP}}_{n,l}(r)$ (i.e., places where $R^{\mathrm{PP}}_{n,l}(r) = 0$), and if we want the screened pseudopotential to be continuous, then $R^{\mathrm{PP}}_{n,l}(r)$ needs a continuous second derivative [57].

Unscreening a pseudopotential to obtain a (bare) ionic pseudopotential is a subtle procedure. Conceptually, we want to remove valence electron interactions from our screened pseudopotential, so that these interactions can be calculated self-consistently when we use the pseudopotential in other environments. As a first attempt, we can do this by just subtracting out the Hartree and exchange-correlation potentials arising from the valence density $n^{\mathrm{PP}}(r)$, and write the unscreened ionic pseudopotential as:

$$V^{\mathrm{PP}}_{n,l}(r) = V^{\mathrm{PP}}_{scr,n,l}(r) - V_H[n^{\mathrm{PP}}(r)] - V_{xc}[n^{\mathrm{PP}}(r)]. \tag{2.72}$$

The resulting pseudopotential retains the core−valence electron interactions of the isolated atom; hence, this is a reasonable unscreening provided that the core−valence charge density overlap does not change considerably when the pseudopotential is used in a different environment [58]. In situations when this is not the case, more sophisticated unscreening procedures are required, such as those proposed by Louie *et al.* [59] where part or all of the *core* density is used in the unscreening procedure (as opposed to just the valence density). These techniques give rise to so-called *non-linear core corrections*.

We then gather up all our unscreened pseudopotentials and write the overall pseudopotential, now using operator notation, as:

$$V^{\mathrm{PP}}(r) = \sum_{l,m} V^{\mathrm{PP}}_{n,l}(r)|Y_{l,m}(\theta,\phi)\rangle\langle Y_{l,m}(\theta,\phi)| \tag{2.73}$$

which, when acting on a state, first projects onto the spherical harmonics, then applies the corresponding l-dependent ionic pseudopotential.

2.9.3 Different recipes

Here, we examine some explicit recipes for pseudopotential construction.

The work of Hamann, Schlütter and Chiang [60] introduced the concept of 'norm-conserving' pseudopotentials. For this class of pseudopotential, we introduce an angular-momentum dependent cut-off radius $r_{c,l}$, measured relative to the position of the nucleus, and list the following requirements of the pseudopotential:

- Pseudo-wavefunction energies for valence electrons should match those from an all-electron reference calculation. This is implicit in Eq. (2.71).
- The pseudo and all-electron wavefunctions for valence electrons agree for $r \geq r_{c,l}$.
- *Norm conservation.* The integrated charge within $r_{c,l}$ is the same for the pseudo and all-electron wavefunctions.
- The logarithmic derivatives of the pseudo and all-electron wavefunctions agree at $r = r_{c,l}$. This ensures the pseudopotential is 'smooth' across $r_{c,l}$, as it ensures the pseudo wavefunction and its radial derivative are continuous at $r = r_{c,l}$. Further, the first derivatives of these logarithmic derivatives with respect to energy agree at $r = r_{c,l}$.

One of the key results of Ref. [60] is that the norm conservation condition (third bullet point) implies the equality of the first energy logarithmic derivatives (second part of fourth bullet point). The latter is important when it comes to pseudopotential *transferability*: it ensures that the logarithmic derivatives of the pseudo and all-electron wavefunctions remain equal in at least a small energy window about the reference energies $\epsilon^{\mathrm{AE}}_{n,l}$, which helps when we use our pseudopotential in different environments [57].

In the scheme of Kerker [61], the form:

$$R_{n,l}^{\mathrm{PP}}(r) = \begin{cases} r^l \exp(\alpha r^4 + \beta r^3 + \gamma r^2 + \delta), & r < r_{c,l}, \\ R_{n,l}^{\mathrm{AE}}(r), & r \geq r_{c,l}. \end{cases} \tag{2.74}$$

is proposed for the (radial) pseudo-orbitals. The exponential helps ensure a nodeless pseudo-orbital in the core region. The four free parameters α, β, γ and δ are then chosen to satisfy the norm conservation condition, and equality of the pseudo-orbitals, and their first and second derivatives at $r_{c,l}$ with all-electron orbitals.

The shape of the pseudopotential inside the core region dictates how quickly the total energy calculated with it converges with an increasing number of plane waves. Troullier and Martins [57] found that screened pseudopotentials which are 'flat' at $r = 0$ (i.e., which have a zero second derivative) tend to give good convergence properties. They therefore extended the Kerker scheme to have:

$$R_{n,l}^{\mathrm{PP}}(r) = \begin{cases} r^l \exp(c_{12} r^{12} + c_{10} r^{10} + c_8 r^8 + c_6 r^6 + c_4 r^4 + c_2 r^2 + c_0), & r < r_{c,l}, \\ R_{n,l}^{\mathrm{AE}}(r), & r \geq r_{c,l}, \end{cases} \tag{2.75}$$

giving rise to the widely-used class of *Troullier-Martins pseudopotentials*. The seven adjustable parameters c_0 through c_{12} are chosen so as to satisfy norm conservation, the continuity of the pseudo- and all-electron orbitals at $r_{c,l}$ up to and including the fourth derivative, and the 'flat at origin' condition $\frac{d^2}{dr^2} V_{scr,n,l}^{\mathrm{PP}}(r) = 0$ for $r = 0$. An example of pseudopotentials generated for carbon following this scheme can be seen in Fig. 2.3.

A further recipe which also attempts to create pseudopotentials with rapid convergence properties is that of Rappe *et al.* [62]. In this scheme, the pseudo-orbitals are expressed in terms of Bessel functions in the core region, and are chosen so as to minimise the total kinetic energy of the pseudo-orbitals beyond a certain Fourier cutoff, denoted q_c.

2.9.4 Relativistic effects

Core electrons, particularly in heavy atoms, are subject to relativistic effects. This is much less of a problem for valence electrons. An added feature of the pseudopotential formalism is that relativistic effects for the core can be built in to the pseudopotential itself; the valence electrons are then treated non-relativistically in subsequent calculations.

In practice, this is accomplished by modifying Eq. (2.69) for the all-electron calculation so that it includes relativistic effects, such as relativistic corrections to the kinetic energy, spin-orbit coupling and the Darwin term. In the case where we average over

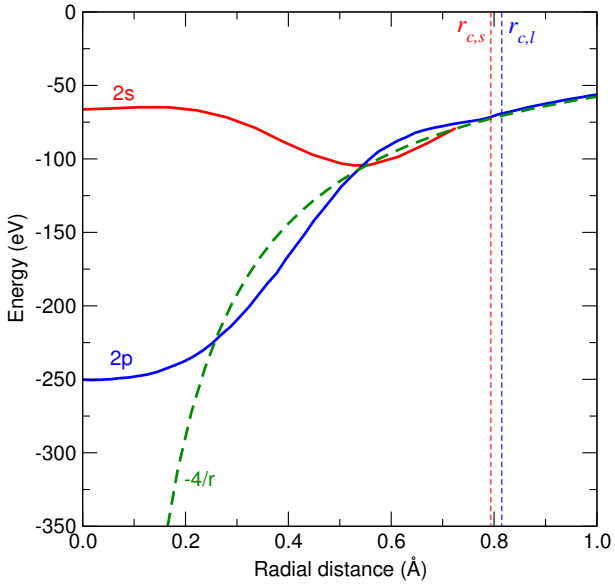

Figure 2.3: Pseudopotentials generated for carbon ($Z = 6$) in the Troullier-Martins scheme. The (unscreened) ionic pseudopotentials $V^{\mathrm{PP}}_{2,s}(r)$ and $V^{\mathrm{PP}}_{2,p}(r)$ (see Eq. (2.72)) are denoted by '2s' and '2p' respectively, and use cutoff radii of $r_{c,s} = 0.794$ Å and $r_{c,l} = 0.815$ Å (shown by the vertical dashed lines). $1s$ states are treated as core states, and the Coulombic potential $-4/r$ for the core region is shown for comparison. Adapted from Fig. 2 of Troullier and Martins [57].

spin-orbit coupling, we obtain a so-called *scalar relativistic equation* [55]:

$$\left(-\frac{1}{2M(r)}\frac{d^2}{dr^2} - \frac{1}{4M(r)^2c^2}\frac{dV_{KS}(r)}{dr}r\frac{d}{dr}\frac{1}{r} + \frac{l(l+1)}{2M(r)r^2} + V_{KS}(r)\right) rR^{\mathrm{AE}}_{n,l}(r) \tag{2.76}$$

$$= \epsilon^{\mathrm{AE}}_{n,l}\, rR^{\mathrm{AE}}_{n,l}(r), \quad \text{where} \quad M(r) = 1 + \frac{\epsilon^{\mathrm{AE}}_{n,l} - V_{KS}(r)}{2c^2}, \tag{2.77}$$

in place of Eq. (2.69). Blue highlighting is used to showcase the differences between this equation and Eq. (2.69). One can also consult the original work of Koelling and Harmon [63] for a form of this equation that is not averaged over spin. The bulk of the pseudopotentials used in this thesis treat relativistic effects at this (scalar) level of theory.

2.9.5 Lifting norm conservation: ultrasoft pseudopotentials

Not all atomic orbitals are amenable to softening within the norm-conserving pseudopotential scheme. The classic example are O $2p$ orbitals, where it is found that the pseudo-orbitals generated in norm-conserving schemes are not greatly different from all-electron orbitals [64]. However, the constraint of norm conservation can be relaxed. Pseudopotentials developed along this line include *ultrasoft* pseudopotentials, introduced by Vanderbilt [64], which further reduce the number of plane waves required to see energy convergence. To accommodate the loss of norm-conservation, the pseudo-orbitals are constructed to be non-orthogonal and the Kohn-Sham equations become a generalised eigenvalue problem. The ultrasoft pseudopotentials used in this thesis

are all of the Vanderbilt type.

2.9.6 Impact on forces

When it comes to calculating forces in the manner of Eq. (2.40), note that the use of pseudopotentials modifies the electronic problem so that $n(\mathbf{r})$ is now only the valence electron density, and $V_{nuc}(\mathbf{r})$ is replaced by a non-local operator. In practice, this just means that the step taken at the third $=$ in Eq. (2.40) is not possible, and we need the individual KS orbitals *as well as* $n(\mathbf{r})$ itself to calculate forces.

2.10 Closing remarks

This chapter focussed on density functional theory and the practical aspects required of DFT calculations.

We discussed Hartree-Fock theory in Sec. 2.2, followed by a general outline of density functional theory in Sec. 2.3. Kohn-Sham DFT and the associated KS equations were introduced in Sec. 2.4, followed by a review of different approximations to the exchange-correlation functional $E_{xc}[n(\mathbf{r})]$ in Sec. 2.5.

In Section 2.6, we looked at how forces and stress can be calculated in DFT, as well as how structures can be relaxed to equilibrium. Section 2.7 detailed how calculations of phonon normal modes and frequencies can be carried out, focussing mainly on the harmonic approximation. Section 2.8 discussed the use of plane-wave basis sets in DFT, and Section 2.9 described pseudopotentials, which are an important tool when using plane-wave basis sets in reducing the basis size.

Chapter 3

Crystal structure searching

3.1 Introduction

Deducing the arrangement of individual atoms in a material is a crucial first step towards elucidating its properties. Experimental techniques using x-ray and electron diffraction data can be used for this purpose, and such data can then be used as a starting point for electronic structure calculations such as DFT. The use of diamond-anvil cells and laser heating in conjunction with these diffraction techniques also allows us access to structural information at high temperatures and pressures.

Considerable work has been done on approaching crystal structure using computational techniques. There are a number of situations where computational approaches are beneficial, for example:

- In materials design, where prototyping many new materials and determining their structures experimentally can be costly and time-consuming
- In places where experimental data is incomplete, for example if only the stoichiometry or space group (but not individual atomic positions) are known from data
- In cases where experimental data is currently impossible to obtain, for example conditions of very high temperature or pressure.

In this chapter we outline different ways in which computational searches have been applied to the problem of determining crystal structure. *Ab initio* random structure searching (AIRSS), outlined below in Section 3.3, is the approach we have applied in the work of Chapters 4, 5 and 6.

3.2 The potential energy surface

Given a collection of M atoms in a periodic cell, we need $3M$ variables to describe all their positions (one for each Cartesian direction), and 6 variables to describe the lattice itself through the variables a, b, c, α, β and γ: a total of $3M + 6$ variables. However, because of translational invariance in the lattice, the total number of *in-*

dependent variables is $3M + 3$, and so we can view the total energy of a particular atomic configuration as a function of $3M + 3$ variables [65]. The multidimensional 'surface' formed by sweeping out these $3M + 3$ variables over their relevant ranges, and calculating the energy in each case is referred to as the potential energy surface (PES).

We are looking for *minima* in the PES: atomic configurations giving rise to low energies. In ideal circumstances (for example, excluding rapid quenching from high temperatures), the ground-state for a collection of M atoms corresponds to the configuration of *least* energy: the global minimum of the PES. As such, crystal structure prediction is a global optimisation problem, and as we shall see in this Chapter, the methods used to carry out this global optimisation are very different from the techniques used to find local minima, such as those discussed in Sec. 2.6. We remark that local minima of the PES are also relevant when we are interested in metastable configurations. If we are working under conditions of finite temperature or pressure, 'energy' should be replaced by a relevant thermodynamic potential such as enthalpy or Gibbs free energy.

We can think of the PES as being made up of *basins of attraction*: sets of configurations for which downward relaxation in energy, for example by a steepest-descents algorithm, leads to the same energy minima [66]. We give a schematic example in Fig. 3.1 below. This simple example shows energy E as a function of only 2 variables, which we have called x and y.

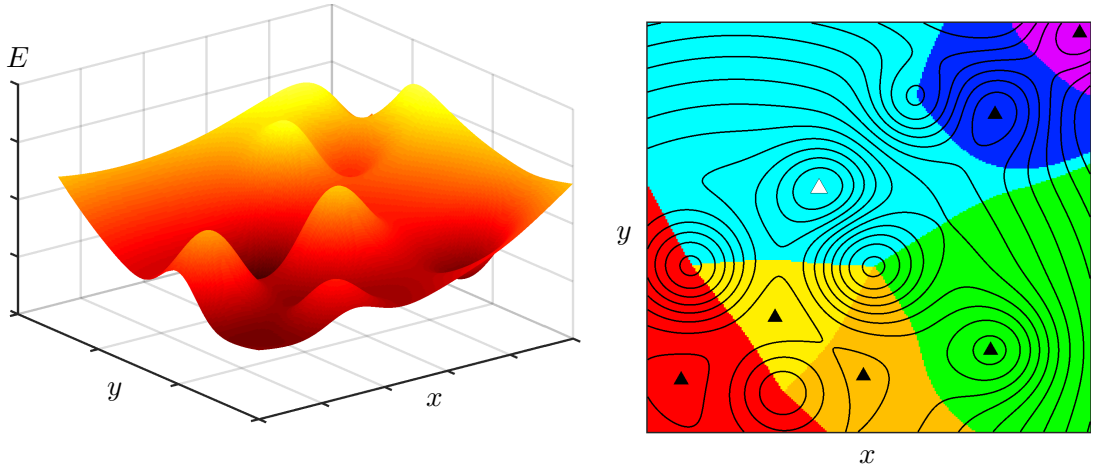

Figure 3.1: (*Left*) An illustrative potential-energy surface in two dimensions. Here the z-axis represents energy. (*Right*) Corresponding contour map of the surface. Minima are marked with a ▲, and the global minimum is marked △. The coloured regions illustrate basins of attraction for their corresponding local minima.

At first sight, locating the global minimum of the PES is a daunting prospect. To be certain of its location, one should perform an exhaustive visit of all local minima of the PES. However, the number of local minima increases *exponentially* with M [66].

Fortunately, a set of quite general principles regarding the PES can be deduced, which are helpful when it comes to finding the global minimum. We follow [66] and list some of these below:

(*i*) Symmetry. If the crystal configuration has some symmetries, the number of independent variables among our total of $3M + 3$ is reduced. As a general rule, both very low and very high energy minima are associated with symmetric structures.

(*ii*) Not all of the PES is worth exploring. Configurations where atoms are very close to each other will result in high energies.

(*iii*) Global or deep minima tend to have large basins of attraction.

(*iv*) The Bell-Evans-Polanyi principle. This implies that a neighbouring minimum is likely to have a lower energy than our current minimum if the barrier between the two minima is small. This principle also implies that low-energy minima tend to 'cluster' into groups known as *funnels*.

A practical searching scheme should therefore take advantage of these general principles, for example by restricting searches to structures with a minimum number of symmetry operators, or avoiding configurations with very short bond lengths. Symmetry is a particularly powerful tool in focusing searches; there are even some systems of sufficiently high symmetry that a 2-dimensional PES, which we used only illustratively in Fig. 3.1, can be useful. Graphene is one such example [67].

3.3 Random structure searching

Sampling the PES randomly offers a straightforward and unbiased method for structure searching. 'Unbiased' is to be understood here in the sense that no previous *structural* information is required in order to generate random structures; for example we do not need to take into account coordination numbers between different atoms. Some bias does inevitably arise in the method from the particular technique used to evaluate the total energy, and from the method used to relax a given structure to equilibrium. These biases are not particular to the random search method, but hold true for crystal structure prediction in general. If prior information is known about the system then this may be incorporated into the searches. In this section, we discuss *ab initio* random structure searching (AIRSS), an implementation of random structure searching by Pickard and Needs [66]. AIRSS has proved to be a very powerful tool in predicting new structures, several of which have subsequently been found experimentally; see for example Ref. [68]. A central tenet of random structure searching is point (*iii*) of Sec. 3.2: we anticipate that the global minimum of the PES has a large basin of attraction. Random samples are therefore more likely to end up in this basin than in the basin of other (local) minima in the PES.

The following steps are carried out in random structure searching:

(1) Generate a random structure. In practice, given (*ii*) of Sec. 3.2, this is actually a random *sensible* structure [66], in the sense that its bond lengths and lattice parameters should be such that atoms are not too close together. We usually specify minimum atom-atom separations, with the goal of avoiding high energy configurations. An alternative strategy could be to evaluate the unrelaxed energy for a random configuration (provided it is computationally efficient to do so) and reject the structure if this energy exceeds a certain threshold [69].

(2) Calculate the energy of the structure and relax to an energy minimum. This can be done through DFT calculations, or using other (possibly less expensive) means such as empirical pair-potentials.

(3) Continue this until a large pool of structures is found and rank by energy.

Figure 3.2 illustrates schematically the random structure searching technique.

When using DFT calculations for searches, we typically use a 'coarse' (less strict) energy cutoff and **k**-point sampling density while searching, to reduce computational cost. Once a pool of structures has accumulated, low-energy structures are refined using stricter energy cutoffs and **k**-point sampling. Searches and energy minima relaxations on individual structures are independent, and the method is suitable for high-throughput calculations.

An extension of the AIRSS algorithm known as 'shaking' involves applying a perturbation to an already relaxed structure, which constitutes a local minimum in the PES, to see if a neighbouring minimum can be accessed. This is intended to take advantage of point (*iv*) in Sec. 3.2.

When applying the random search technique, there is the question of how many structures should be relaxed before searching is ceased. In light of (*iii*) in Sec. 3.2, we could reasonably expect the global minimum structure to turn up a number of times, if we have performed a sufficiently large number of relaxations. This can be used as a halting criteria for the AIRSS algorithm, i.e., searching is stopped after the same lowest-energy structure turns up a certain number of times.

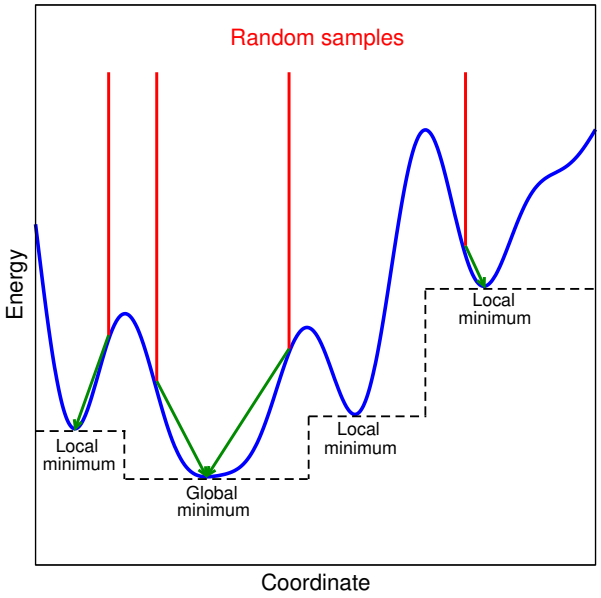

Figure 3.2: Schematic illustrating the random sampling technique. Random samples (red) are dropped onto a PES (blue), and then relaxed to their nearest local minimum (green arrows). Also shown with black dashed lines is the effective PES that results from performing local optimisation. See Figs. 3.1 and 3.2 of Ref. [65] for similar diagrams.

The remaining sections of this chapter detail further computational methods for crystal structure prediction. In Chapters 4, 5 and 6, where we apply the random search technique, we will provide further information about different aspects of random structure searching and its practical application.

3.4 Algorithms based on the Metropolis criteria

3.4.1 Simulated annealing

The use of simulated annealing (SA) as a tool for structure prediction borrows ideas from physical annealing. To use an example of Woodley and Catlow [70], consider a material in its melted state. Its constituent atoms are disordered, but it will crystallise in an ordered structure as the temperature is lowered, as long as the temperature is not lowered too abruptly. Otherwise, the material may quench to a glass-like state or to a structure that is not the global minimum in energy.

To apply simulated annealing, we introduce a *cost function* – for example, the energy – and minimise this through a simulated annealing algorithm, which proceeds as follows. We begin at a 'synthetic' temperature, T, and initialise the crystal structure in some starting configuration. This can be chosen at random. A new candidate structure is then created, for example through random perturbations of some or all of the atoms in the previous configuration, by swapping certain atoms, or by adjusting the lattice constants [71]. The new structure is then accepted or rejected according to a Metropolis criterion. Denoting the value of our cost function by E, and its current

value by E_c, this criteria is:

`IF` E is smaller in the new structure (i.e., $E < E_c$), accept the structure

`ELSE` Uniformly generate a random number $p \in [0, 1]$ and then accept the new structure if $\exp(-(E - E_c)/T) < p$, otherwise reject the structure

We start our annealing process with a high temperature T and repeat the above steps, decreasing temperature slowly until $T = 0$. It is typical to carry out several simulated annealing runs. More sophisticated versions of the SA algorithm involve *parallel tempering*, where concurrent SA runs are carried out at different temperatures. The Metropolis criteria above can be used to propose a move between two different runs, such as swapping the current configuration (structure) with another run, or swapping the current temperature [65].

As our illustrative PES of Fig. 3.1 shows, using a purely 'descending' algorithm like steepest-descents from a given starting configuration tends to lead us to the nearest local minimum. The simulated annealing algorithm instead permits 'uphill' steps in energy whenever $T > 0$, with the probability of accepting a move uphill decreasing as $T \to 0$. In this way, the algorithm can explore a large portion of the PES at high T to begin with. A practical implementation of annealing must weigh the benefits of decreasing T slowly against the computational cost of doing so. Should T be decreased too quickly, the algorithm can become 'trapped' in a local energy minima and may therefore not recover the global minimum in energy.

Various changes to the basic SA algorithm outlined above, such as different cost functions, or different techniques for generating new structures, can be introduced depending on the types of structures at hand. It is instructive to review a couple of examples of SA in the literature for concreteness.

Bulk boron nitride

The work of Doll *et al.* used SA to search for bulk structures of boron nitride [72]. The cost function in this work is energy, as calculated with Hartree-Fock using Gaussian basis sets. New structures were generated by moving single atoms (70%), swapping atoms (10%), altering the lattice parameters (15%), and relocating the cell origin (5%). A total of 12,500 SA steps were used, decreasing T from 1.00 eV to 0.78 eV, whereupon the system was quenched by setting T to 0 eV for a further 5,000 steps. A total of 329 annealing runs were carried out. This methodology succeeded in finding the experimentally known hexagonal, zinc blende and wurtzite BN structures, as well as four different energetically competitive ones.

Zeolite structures

Brouwer and Horvath [73] apply SA to determine zeolite (SiO_2) crystal structures, employing a cost function based on *geometric* considerations, which is designed to favour configurations typically encountered in SiO_2 structures (such as expected bond

lengths and angles). This is used to recover the structure of three known zeolites.

Polymorph Predictor software

At the time of writing, the 'Polymorph Predictor' module of the commercially-available `Materials Studio` software suite implements SA to predict the structure of molecular crystals. This software uses user-supplied molecular building blocks and force-fields to compute the total energy (as the cost function) [74].

3.4.2 Conformation-family Monte Carlo (CFMC)

Pillardy *et al.* introduce the CFMC method in Ref. [69], with a view toward molecular crystals. The cost function is energy, as calculated using force-field approaches. A key concept introduced by the CFMC method is to keep track of the histories of structures generated during a search, and to group these into *families*. All structures in a family are crystallographically equivalent, i.e., they are the same structure, but represented with different atomic fractional coordinates and lattice parameters.

The CFMC search is initialised by creating a set of structures randomly and grouping them into families. These are ranked in energy, and a structure is picked from the lowest-energy family, the 'generative family', which we denote by F. This is then modified to create a new structure by adjusting molecules through translation, rotation (changing the Eulerian angles of a molecule), or perturbing the unit cell parameters. An extra modification, more specific to the CFMC scheme, is *averaging*: a new structure is crafted by mixing the existing structure with another structure, either from the same or a different family, e.g., by averaging the fractional coordinates of the two. The energy of the new structure is evaluated, and it will either result in the creation of a new family, or be classifiable within the set of existing families. Letting it belong to the family F', a Metropolis SA-like step is used to decide whether F' should now replace F as the generative family, based on energies, and the algorithm starts over.

The above scheme was applied in Ref. [69] to 9 molecular solids sourced from a crystal structure database. The CFMC method was able to recover the original structures as well as several alternative low-energy configurations, taking into account accuracies in the force-fields for these solids.

3.4.3 Basin hopping

The term *basin hopping* tends to be a synonym for the 'Monte Carlo plus energy minimization (MCM)' algorithm [65], which is why we list it here. In this technique, the PES is 'transformed' into discrete regions corresponding to its basins of attraction (see the dashed lines in Fig. 3.2); in practice this simply means that all candidate structures are always locally relaxed. We perform random perturbations of a structure on this transformed PES, accepting or rejecting moves according to the Metropolis criteria, but not annealing in T.

Wales and Scheraga [75] instead use the term 'basin hopping' to refer to the class of algorithms formed by combining the PES transformation with a step-taking scheme, which could be a genetic algorithm, simulated annealing, and so on. The emphasis is on the fact that the transformed PES is a more useful object than the original PES, regardless of the step-taking scheme at hand.

3.5 Minima hopping

The minima hopping method, as detailed by Goedecker [76], and Goedecker and Amsler [77], exploits molecular dynamics (MD) runs in order to explore the PES. The parameters controlling the MD runs are updated as the algorithm progresses, depending on the outcome of completed MD runs, and a 'history' of visited minima is maintained.

First, an MD run is commenced with a given 'current' structure M_c, and with kinetic energy E_K. This run is halted after a specifiable number of potential energy maxima have been crossed. The structure at this point is locally relaxed, yielding a new structure M. Then:

`IF` $M = M_c$ (we have 'fallen' back into the minima containing our starting structure), `OR` M is in our history of minima, we increase E_K. The rationale here is that we wish to escape M_c (in the former case), or move away from already-visited minima (in the latter case). At this point the algorithm restarts; another MD run begins with the new E_K starting from the same M_c.

`ELSE` We have arrived at a new minimum, and E_K is decreased.

In the case of a new minimum, we make the replacement $M \to M_c$ if the energy of M does not exceed M_c by a certain threshold. This threshold is then decreased, M added to the history, and a new MD run starts. Otherwise, we increase the threshold, then start a new MD run. It is also possible to treat this step instead using a Metropolis criteria [65], but note we do not anneal in T.

The algorithm presented in Ref. [76] proposes that the kinetic energy increases/decreases be $\approx 5\%$, and the threshold increases/decreases be $\approx 2\%$. Tests of this method on a 38-atom Lennard-Jones cluster showed that 830 minima were visited before finding the global minimum in energy. Subsequent work [77] looked at a 64-atom unit sell of silicon using interatomic potentials; runs successful in finding the ground state structure (diamond) visited an average of 13,000 (non-distinct) minima.

A software implementation of the minima hopping algorithm can be found in the 'Minhocao' package distributed as part of the BIGDFT software suite.[1]

[1] At the time of writing, this code could be obtained from the BIGDFT wiki: http://www.bigdft.org/.

3.6 Evolutionary and genetic algorithms

Evolutionary algorithms (EAs) approach the PES global minimum problem using mechanisms inspired by biological evolution [65]. The basic principle is that a population − in this case, of crystal structures − can be progressively evolved and improved over many generations to create a new set of structures. As is the case with SA, 'improvement' is measured by some cost function.

EAs proceed by initialising a starting population of crystal structures, for example through random sampling. We calculate the cost function for each of these and rank them. *Variation operators* are then applied to a certain (specifiable) set of the population − for example, the best 60% of the population, as determined by the cost function − to create new structures. The remaining (40% in this example) structures are discarded, in a 'survival of the fittest' mode of thinking. Examples of variation operators are [65, 78, 79]:

(*i*) *Heredity*: cuts of random thickness and orientation are taken from two 'parent' structures and assembled to create a new 'child' structure. Lonie and Zurek also use the descriptor *crossover* or simply 'cut-and-splice' for this operator [78]. The idea behind this operator is that child structures can inherit energetically optimal substructural units from parent structures, with the goal of creating more favourable structures.

(*ii*) Lattice *mutation*: apply a set of random strains to distort the cell lattice constants

(*iii*) Permutations and atom swapping: exchange sets of chemically distinct atoms within the structure

(*iv*) *Ripple* (periodic displacement) operator: this implements a sinusoidal wave-like displacement of atoms in a cell, so that atoms in some regions undergo large displacements and atoms in other regions have very small displacements. The motivation for such an operator comes from the observation of certain naturally occurring crystal structures possessing a wave-like structural motif [78].

The new generation of structures is then re-ranked using the cost function, and we proceed to the next generation.

An important consideration in EAs is how the *diversity* of the population changes as we evolve through generations. Ideally, we would maintain a relatively high diversity at each generation so that radically new crystal structures (from those in a given generation) can still be produced. The work of Oganov *et al.* provides a 'quasientropy' metric for diversity, allowing it to be monitored as the EA progresses [79]. Implementations of EAs for crystal structure prediction can be found for example in the XtalOpt [78], USPEX [80], and GASP codes [81], as well as in the work of Abraham and Probert

[82, 83].[2]

As we did for SAs, we comment on a couple of concrete example applications of EAs in detail. Oganov *et al.* [84] applied EAs to search for new structures formed by elemental boron at high pressures. The cost function was the relaxed energy, as calculated using DFT with the PBE exchange-correlation functional. The EA searches used population sizes of 10-50 structures, with larger populations employed for structures with more atoms in the unit cell. Generally, $\gtrsim 30$ generations of evolution were carried out, with the best structures turning up in $\lesssim 20$ generations. The heredity and lattice mutation operators were used in a %85/%15 split (swapping not being applicable).

Shamp *et al.* [85] have used EAs to search for stable phosphorous hydrides PH_n, $n = 1-6$ formed at high pressure (≈ 200 GPa), again with relaxed DFT-PBE energies as the cost function. A wide variety of population sizes were used, ranging from 53-1702.

3.7 Particle Swarm Optimisation

The principles behind the Particle Swarm Optimisation (PSO) technique, as applied to crystal structure prediction, are given for example by Wang *et al.* [86]. This method involves a population (a 'flock' or 'swarm') of structures which are permitted to move around on the potential energy surface. The 'movement' of one member of the flock is coupled to the motion of all other members, and in particular is influenced by those members of the flock that are in low energy areas of the PES. In this way, the flock is permitted to explore the PES widely before converging on the global minimum in energy.

A key aspect of the method is how movement − corresponding to the generation of new structures − is controlled in the PSO algorithm. We proceed as follows. The flock is initialised with a random set of structures, which are then structurally relaxed and ranked according to 'cost'. A subset of these (e.g., as with EAs, the best 60%) are selected to create new structures.

We now introduce some notation [86]. Let $x^t_{i,j}$ be the coordinates of structure i in the flock, so that j indexes the atomic positions, and t labels the generation number. Each $x^t_{i,j}$ is assigned an abstract 'velocity' $v^t_{i,j}$. For generation 1, as with the structures themselves, these are chosen randomly. We also introduce $\text{pbest}^t_{i,j}$, the coordinates of structure i after it has undergone local relaxation, and gbest^t_j, the coordinates of the best structure in the swarm at generation t. The velocities $v^t_{i,j}$ are updated according to:

$$v^{t+1}_{i,j} = \omega v^t_{i,j} + c_1 r_1 (\text{pbest}^t_{i,j} - x^t_{i,j}) + c_2 r_2 (\text{gbest}^t_j - x^t_{i,j}). \tag{3.1}$$

[2] At the time of writing, the XtalOpt, USPEX and GASP codes were available from http://xtalopt.github.io/, http://uspex-team.org/uspex/overview, and http://gasp.mse.ufl.edu/, respectively.

Ultimately, the coefficients ω, $c_1 r_1$ and $c_2 r_2$ in this equation are in principle adjustable parameters for the PSO method. The quantities c_1 and c_2 are referred to as the self-confidence factor (c_1) and the swarm-confidence factor (c_2); in practice, these are set equal ($c_1 = c_2 = 2$ [86]) and the parameters r_1 and r_2 are randomly generated in [0,1], a technique intended to avoid the PSO algorithm becoming trapped in local minima. The quantity ω is referred to as the 'inertia weight' and in practice is reduced linearly from the value 0.9 (for the first generation) to 0.4 (for the final generation). In this way, the new velocity $v_{i,j}^{t+1}$ is a weighted sum of the old velocity $v_{i,j}^{t}$, and the distances of the structure $x_{i,j}^{t}$ from both its local minimum, $(\text{pbest}_{i,j}^{t} - x_{i,j}^{t})$, and the swarm's global minimum $(\text{gbest}_{j}^{t} - x_{i,j}^{t})$. Finally, the structures themselves are updated using:

$$x_{i,j}^{t+1} = x_{i,j}^{t} + v_{i,j}^{t+1}, \tag{3.2}$$

which alters the atomic positions; the original lattice parameters (unit cell) are not changed [87]. A new swarm of structures is thus created, and the algorithm repeats. A schematic of the PSO algorithm can be found in Fig. 3.3.

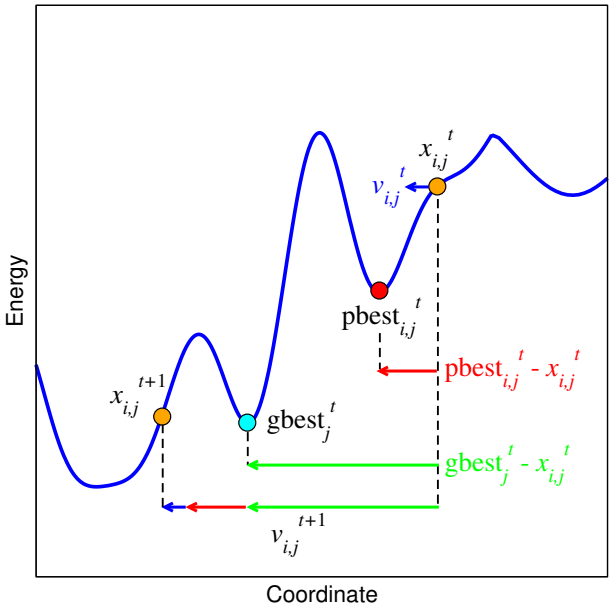

Figure 3.3: One-dimensional schematic showing the PSO update step, going from generation t to generation $t+1$. A structure $x_{i,j}^{t}$ (top-right orange circle) has velocity $v_{i,j}^{t}$ (blue arrow), and yields a further structure $\text{pbest}_{i,j}^{t}$ (red circle) after local optimisation. The lowest energy structure in the swarm at this generation is shown by gbest_{j}^{t} (cyan circle). A new velocity, $v_{i,j}^{t+1}$, is calculated for the structure according to Eq. (3.1) and shown pictorially as the sum of the blue, red and green arrows. This yields a new structure, $x_{i,j}^{t+1}$, through Eq. (3.2). For the sake of simplicity, we have set $\omega = c_1 r_1 = c_2 r_2 = 1$ in Eq. (3.1). See Fig. 2 of Wang *et al.* [86] for a similar diagram.

As is the case for EAs, preserving diversity in the swarm is important. One way of doing this is to add a certain percentage of randomly generated structures to the swarm at each generation [87].

As well as introducing the method, Wang *et al.* [86] demonstrate that using swarm sizes of $20 - 30$, several of the known structures of elemental Li, C, Si and Mg at various pressures up to 100 GPa are produced by the PSO method in ≤ 30 generations of the algorithm. The energy and relaxation calculations are performed with DFT-LDA. A further example of its use can be found in Ref. [88], where PSO methods are used to search for high-pressure phases of CO_2 up to 1,200 GPa. Swarms of 30 structures are used, with the lowest 60% being used at each step to create the next generation and 40% being introduced randomly. Runs took a total of 50 generations.

A software implementation of the PSO method can be found in the CALYPSO code [87].[3]

3.8 Data Mining

We are in an era where large databases, collecting experimental and theoretical results for crystal structures, are now available. Examples include the Inorganic Crystal Structure Database (ICSD) [89] (∼170,000 entries), the Materials Genome Project [90] (∼49,000 entries) and the Cambridge Structural Database [91] (∼680,000 entries). These databases can be mined for structural analogues. For example, Lyle *et al.* [92] used data mining alongside random sampling to predict new SiO_2 and TiO_2 structures formed at megabar pressures. To do this, the ICSD was queried for AB_2 type compounds, the replacements A→{Si,Ti} and B→O were made, and the resulting structures relaxed.

Structure and *energy* information, if available in a database, can also be mined through machine-learning or regression style approaches. Curtarolo *et al.* [93] describe a technique where a database of binary alloys and their calculated formation energies can be used to predict the energies of new alloys; such information could be used to inform a structural search.

3.9 Closing remarks

The methods presented in this chapter represent the enormous diversity and creativity with which physicists and chemists have risen to the challenge of crystal structure prediction. It is not an exhaustive survey of all possible methods available in the field, however, we have attempted to showcase a set of algorithms in detail, and furnish these with some concrete examples. The ongoing development, application and refinement of techniques for CSP continues to be a thriving area of research.

[3] At the time of writing, this code is available from `http://www.calypso.cn/`.

Chapter 4

High-pressure beryllium, magnesium and calcium fluorides

In this chapter, we investigate three group-II difluoride compounds: BeF_2, MgF_2 and CaF_2 using structure searches and DFT calculations. These compounds have a number of optical uses, some form naturally as minerals, and they are isoelectronic (and therefore structurally similar) to several other AB_2 compounds such as SiO_2 and TiO_2. The text of this chapter largely follows the work published in:

J. R. Nelson, R. J. Needs, and C. J. Pickard
High-pressure phases of group II difluorides: polymorphism and superionicity
Physical Review B **95**, 054118 (2017).

4.1 Introduction

The Group-II difluorides form materials with a wide variety of technological uses. BeF_2, and mixtures of it with further fluorides and difluorides, are used to create glasses for use in infrared photonics, which have excellent transmittance in the UV. BeF_2 glass itself has a large bandgap of 13.8 eV [94, 95]. BeF_2 is chemically stable and is employed as a mixture component in nuclear reactor molten salts, where it is useful as a coolant, and is also capable of dissolving fissile materials [96]. MgF_2 is birefringent with a wide wavelength transmission range, and is used in the manufacture of optical components such as polarizers [97]. CaF_2 also offers a high transmittance across a wide range of wavelengths and is used in optical systems, as well as an internal pressure standard [98, 99]. MgF_2 and CaF_2 occur naturally as the minerals sellaite and fluorite, therefore high pressure modifications of these compounds are of interest in geophysics.

Group-II difluorides have 16 valence electrons per formula unit, and are isoelectronic to other AB_2 compounds of industrial or geophysical significance, such as TiO_2 and SiO_2. As such, these compounds share many similar crystal structures, albeit stable at different pressures. Because of this structural similarity, Group-II difluorides have

been investigated as structural analogues of silica phases [100]. BeF_2 is particularly similar to silica at low pressures [101], as in addition to being isoelectronic, the fluoride (F^-) and oxide (O^{2-}) ions have similar radii and polarisabilities, and the Be/F and Si/O atomic radii ratios are similar at ≈ 0.3 [102]. MgF_2 has also been explored as a model for higher pressure silica phases [103].

We are interested in the structures and phases of Be-, Mg- and CaF_2 at ambient and elevated pressures, and the implications of such phases for other AB_2 compounds. Our approach to determining stable phases in these compounds will use computational structure searching alongside density functional theory (DFT) calculations, and we explore the pressure range 0−70 GPa.

Justification for the use of DFT methods at these high pressures usually comes from observed agreement between experimental results at high pressures, or more advanced electronic structure methods, and the results of DFT calculations. For example, the work of Driver *et al.* has shown good agreement between DFT-calculated phase transition pressures in silica, and accurate Quantum Monte−Carlo calculations and experimental results [104]. The PBE exchange-correlation functional was used in this work. However, care does need to be taken when using pseudopotentials at high pressures; we must ensure that the pseudopotential cutoff radii r_c (see e.g. Fig. 2.2) are chosen small enough so that the core regions for the pseudopotentials of neighbouring atoms do not overlap.

4.2 Methods

4.2.1 Electronic structure calculations

All calculations are carried out with version 8.0 of the CASTEP plane−wave pseudopotential DFT code (Sec. 2.8.1).

Our calculations of enthalpy vs. pressure curves in this chapter, lattice parameters, and supercell phonon calculations all use default Vanderbilt-type ultrasoft pseudopotentials (Sec. 2.9.5) for Be, Mg, Ca, F, Si and O as generated internally by the CASTEP code and the Perdew−Burke−Ernzerhof (PBE) exchange−correlation functional (Sec. 2.5.2). The core radii of these pseudopotentials are found to be sufficiently small for our high pressure calculations. A plane−wave cutoff of 800 eV, Monkhorst-Pack Brillouin zone sampling density of at least $2\pi \times 0.04$ Å^{-1} (Sec. 2.8.3), grid scale of 2 (for representing the density) and fine grid scale of 2.5 (grid for ultrasoft core or augmentation charges) are used in these calculations.

To obtain the plane−wave cutoff and Brillouin zone sampling density mentioned here, we test the convergence of total energy differences between a small set of crystal structures with progressively increasing plane−wave cutoff and Brillouin zone sampling densities. The parameters we use in this Chapter are chosen to ensure that these

energy differences are converged to <1 meV/f.u.

Calculations of phonon frequencies use the finite−displacement supercell method in CASTEP (Sec. 2.7.4), and the cumulant force constant matrix cutoff scheme (Sec. 2.7.5). Details of the supercell sizes used in these finite−displacement phonon calculations are given in subsequent sections.

Bandgap calculations in this chapter are carried out with norm−conserving pseudopotentials, which are required in order to use hybrid density functionals (Sec. 2.5.3) in CASTEP. Generation strings for these potentials are taken from the version 16.0 CASTEP Norm-Conserving Pseudopotential ('NCP') library, and used in version 8.0 of the code. Our calculations use the 'HSE06' variant of the Heyd-Scuseria-Ernzerhof hybrid functional (Eq. (2.38)), a plane−wave cutoff of 1600 eV, a Brillouin zone sampling density of at least $2\pi \times 0.1$ Å^{-1}, and grid and fine grid scales of 2 and 2.5 respectively.

The use of the HSE06 functional is expected to generally improve the accuracy of bandgap calculations carried out with DFT, though at a greater computational cost. We therefore adopt the following calculation strategy: structures are first relaxed with the PBE functional, norm-conserving pseudopotentials, a basis set cutoff of 1600 eV and a Brillouin zone sampling of $2\pi \times 0.1$ Å^{-1}. The HSE06 functional is then used with PBE-relaxed geometries for a self-consistent calculation of the electronic bands of the structure. Our stress calculations indicate that the use of the HSE06 functional with PBE geometries gives rise to small forces of $\lesssim 0.1$ eV/Å on each atom. Electronic density of states calculations are performed using the OPTADOS code [105, 106, 107].

4.2.2 Classical molecular dynamics calculations

As we will discuss in subsequent sections of this chapter, we carry out some classical molecular dynamics simulations for CaF_2. These simulations are performed using the LAMMPS classical molecular dynamics code [108]. In these simulations, pairwise potentials for the Ca−Ca, Ca−F and F−F interaction energies are taken from Zeng *et al.* [109], and have the form:

$$V_{\mathrm{X-Y}}(r) = \frac{Z_{\mathrm{X}} Z_{\mathrm{Y}}}{r} - \frac{C_{\mathrm{XY}}}{r^6} + A_{\mathrm{XY}} e^{-r/\rho_{\mathrm{XY}}}, \tag{4.1}$$

where $Z_{\mathrm{Ca}} = +2$ and $Z_{\mathrm{F}} = -1$ are the ionic charges for Ca and F, respectively. We have $A_{\mathrm{FF}} = 2058.994$ eV, $A_{\mathrm{CaF}} = 1717.441$ eV, $\rho_{\mathrm{FF}} = 0.252$ Å, $\rho_{\mathrm{CaF}} = 0.287$ Å, $C_{\mathrm{FF}} = 16.703$ eVÅ^6 and $C_{\mathrm{CaF}} = 0.102$ eVÅ^6, with all other parameters zero. We exclude the effect of the 'shell model' in [109]. A recent study by Faraji *et al.* [110] has shown that this potential (without shell effects) reasonably reproduces the enthalpy differences between various CaF_2 polymorphs when compared against DFT calculations, even at pressures up to 80 GPa. Periodic boundary conditions are assumed, and, apart from the Coulomb interaction in Eq. (4.1), all other interactions are cut off at a distance of 12 Å.

4.2.3 Searches

The *ab initio* random structure searching (AIRSS) technique (Sec. 3.3) is used to search for Group-II difluoride structures at three pressures: 15, 30 and 60 GPa. Minimum atom-atom separations are chosen based on short AIRSS runs; for example, for BeF_2, we specify the three pairwise separations Be−Be, Be−F and F−F. We can also impose symmetry constraints on our generated structures such that low symmetry structures are not considered. This strategy tends to speed up the searches because such low-symmetry structures are unlikely to have low energies according to Pauling's principle [111, 112], although we note that we do allocate at least part of our searching time to check low symmetry structures, for completeness. Examples of the use of AIRSS in previous structure prediction studies (some of which were conducted alongside experimental results) can be found in Refs. [4, 68, 113, 114]. We limit our searches to a maximum of 8 formula units (24 atoms) per cell.

As well as searches for new BeF_2, MgF_2 and CaF_2 structures, we also carry out variable stoichiometry structure searching at 60 GPa only, to examine the possibility of other thermodynamically stable compositions. We carry out these searches over 29 different stoichiometries X_nF_m, X = Be, Mg, Ca. This total includes structure searches for the elements alone (n=1, m=0) and also includes the n=1, m=2 difluoride stoichiometry.

In addition to AIRSS, we supplement our searches with a set of 15 known AB_2-type structures taken from a variety of compounds. These are listed overleaf in Table 4.1, and constitute an attempt at very small-scale data mining (Sec. 3.8).

Table 4.1: List of known AB_2 structures used in our structure searches. Atoms are swapped appropriately, for example Si→Be, O→F, and the resulting structure is then relaxed with DFT. Structures are taken from the Inorganic Crystal Structure Database (ICSD) [89] or from literature. We give the 5-digit ICSD reference number in the former case. The space group ('SG') is given in Hermann-Mauguin ('HG') notation as well as space group number. Z is the number of formula units in the cell.

Compound	SG (HM)	SG	Lattice	Z	Name(s)	Ref.
HfO_2	$P2_1/c$	14	monoclinic	4	Baddeleyite	60903
SiO_2	$P2_1/c$	14	monoclinic	32	Coesite-II	[115]
SiO_2	$C2/c$	15	monoclinic	8	Coesite-I	[115]
SiO_2	$C2/c$	15	monoclinic	6	Moganite	67669
BeF_2	$C2/c$	15	monoclinic	6	–	[116]
SiO_2	$Pnnm$	58	orthorhombic	2	$CaCl_2$-type	26158
SiO_2	$Pbcn$	60	orthorhombic	4	α-PbO_2 [(a)]	[117]
TiO_2	$Pbca$	61	orthorhombic	8	Orthorhombic-I, OI	[118]
ZrO_2	$Pnma$	62	orthorhombic	4	Cotunnite, Ortho-II ($PbCl_2$)	[119]
SiO_2	$P4_12_12$	92	tetragonal	4	α-cristobalite	75300
SiO_2	$P4_2/mnm$	136	tetragonal	2	Rutile, β-PbO_2, Plattnerite	9160
SiO_2	$P3_121$	152	trigonal	3	α-quartz	27745
SiO_2	$P6_222$	180	hexagonal	3	β-quartz	31088
SiO_2	$Pm\bar{3}m$	221	cubic	46	Melanophlogite	159046[(b)]
SiO_2	$Fd\bar{3}m$	227	cubic	2	β-cristobalite	77458

[(a)] Has a number of aliases: Seifertite (SiO_2), Scrutinyite (α-PbO_2), Columbite (TiO_2)

[(b)] Interstitial carbon atoms (representing methane) were removed from this structure

4.3 Beryllium difluoride

4.3.1 Results of variable stoichiometry searches

At 60 GPa, elemental beryllium has the α-Be hexagonal closed-packed (hcp) structure, space group $P6_3/mmc$ [120]; we also verify that this is the case directly through structure searches. We find a molecular crystal comprised of F_2 molecules with space group $Cmce$ to be the lowest enthalpy fluorine structure at 60 GPa, and this applies also to the Mg-F and Ca-F variable stoichiometry searches to be presented later in this chapter. This structure matches that used in the caesium fluoride searches of Ref. [121].

Our variable stoichiometry searches yield a set of Be_nF_m structures for integer n and m, as well as structures for Be and F. To establish which stoichiometries are thermodynamically stable at a given pressure, we construct a *convex hull* based on the calculated enthalpies of these structures. Along the x-axis, we show the molar ratio of fluorine present in the compound: for Be_nF_m, this is the quantity $m/(n+m)$. It runs from 0 (no F, pure Be) to 1 (pure F, no Be). On the y-axis, we plot the formation

enthalpy (per atom) for the compound from elemental Be and F. This is the quantity:

$$\Delta H = \frac{H(\mathrm{Be}_n\mathrm{F}_m) - H(\mathrm{Be}) - H(\mathrm{F})}{n+m}, \tag{4.2}$$

where $H(...)$ stands for the enthalpy of the species ..., as calculated from DFT. The quantities $H(\mathrm{Be})$ and $H(\mathrm{F})$ should be taken from the lowest-enthalpy structure for these elements.

Once we have done this, straight lines connecting the elements to the lowest values of ΔH are drawn, forming the convex hull. Stoichiometries that are part of this hull are said to be 'on the hull' and are thermodynamically stable. All other stoichiometries are thermodynamically unstable to compounds that are on the hull.

The results of doing this for the Be-F system at 60 GPa is shown in Fig. 4.1. Only the lowest-enthalpy structure at each stoichiometry has been plotted using Eq. (4.2). Of the 29 stoichiometries searched, only BeF_2 is found to be stable at this pressure, and in the following sections we will focus only on the BeF_2 stoichiometry.

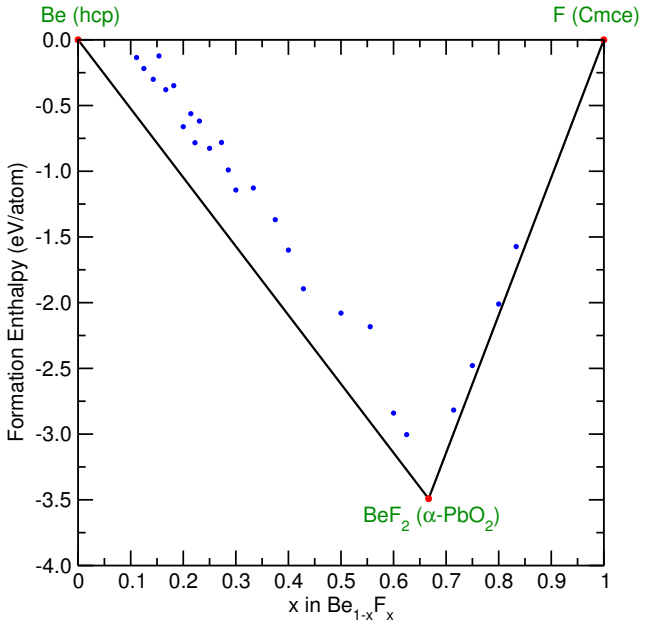

Figure 4.1: Convex hull for the Be-F system at 60 GPa.

4.3.2 Low−pressure results

Beryllium fluoride (BeF_2) has several thermodynamically accessible phases which have been obtained in experimental studies. At temperatures below its melting point (820 K) and pressures at or below atmospheric pressure, the α-quartz, β-quartz, α-cristobalite, β-cristobalite and glass phases of BeF_2 have been prepared under various conditions [122, 123].

Our results from structure searching calculations at low pressures (0−8 GPa) are summarised in Fig. 4.2(a), which shows the static-lattice enthalpies of several BeF_2 structures as a function of pressure.

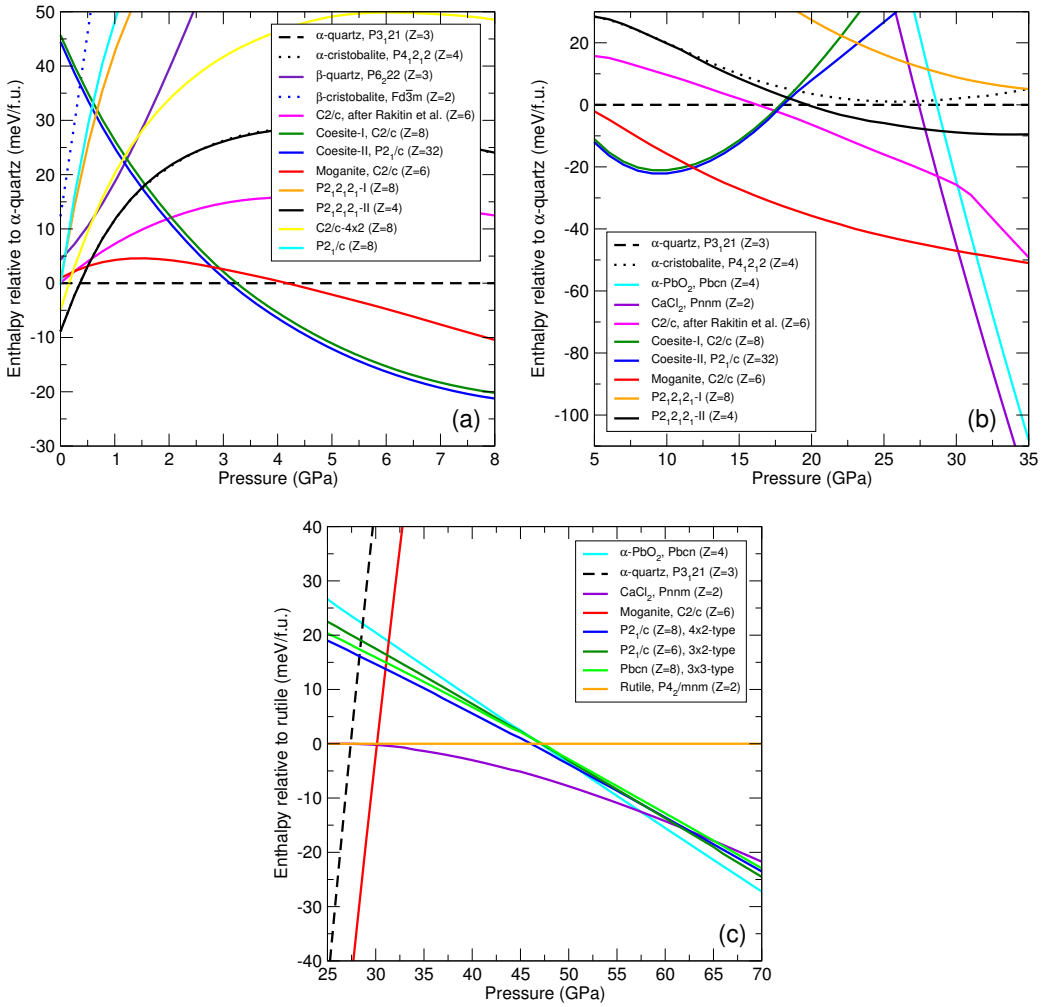

Figure 4.2: Static lattice enthalpies for BeF_2 calculated with the PBE functional over the pressure ranges (a) 0−8 GPa, (b) 5−35 GPa and (c) 25−70 GPa. In (a) and (b), enthalpies are shown relative to the α-quartz phase, while in (c) they are shown relative to the rutile phase.

Beryllium fluoride shows extensive polymorphism at low pressures; we find at least 10 structures for BeF_2 (all those shown in Fig. 4.2(a), except Coesite-I and Coesite-II) lying within about 20 meV/f.u. of one another at 0 GPa. The α- and β-quartz, and α- and β-cristobalite structures are part of this set of 10 structures. Within our current calculational framework (DFT−PBE), the α-cristobalite structure is lowest in enthalpy at 0 GPa, lying 8.9 meV/f.u. below α-quartz, but other low enthalpy structures are also of interest as they can be stabilised by temperature. There is some experimental evidence for as-yet-unknown high-temperature low-pressure BeF_2 phases [124], and metastable structures produced in our searches provide useful reference

crystal structures that could be matched to available experimental data at elevated temperatures.

We remark here that the PBE functional may not provide a completely accurate energy ordering for these structures at low pressure. For example in silica, DFT−PBE also predicts that the α-cristobalite structure has a lower enthalpy than the α-quartz structure at 0 GPa, but the latter is the experimentally observed ground state structure. However, as we noted in Sec. 4.1, high pressure phase transition pressures in silica calculated with PBE are in excellent agreement with accurate Quantum Monte−Carlo calculations [104], so we anticipate that the PBE functional will perform well at high pressure.

A recent study by Rakitin *et al.* found a $C2/c$ structure for BeF_2 which is close in enthalpy to α-quartz at 0 GPa [116]. Results using AIRSS produce five further polymorphs for BeF_2, labelled 'Moganite', $P2_12_12_1$-I, $P2_12_12_1$-II, $C2/c$−4×2 and $P2_1/c$ in Fig. 4.2(a), which have static-lattice enthalpies of +0.9, +0.4, −8.9, −4.9 and −0.3 meV/f.u. relative to the α-quartz phase at 0 GPa. We discuss each of these in more detail below.

The 'Moganite' polymorph, which turned up in our searches (and was also included in our set of 15 AB_2 structures in Table 4.1) is BeF_2 in the silica moganite structure with Si→Be and O→F. This has space group $C2/c$ and 6 formula units of BeF_2 in the primitive cell.

At the pressures shown in Fig. 4.2(a), the $P2_12_12_1$-II polymorph has space group symmetry $P4_32_12$ (#96), and is actually an enantiomer of α-cristobalite. A mirror-image transformation $(x, y, z) \rightarrow (-y, -x, z)$, i.e., a reflection of atomic positions in the (110) plane, relates the two structures. This situation is entirely analogous to SiO_2, where rigid-unit phonon modes (RUMs) distort the β-cristobalite structure to one of either $P4_12_12$ symmetry (our α-cristobalite) or to $P4_32_12$ symmetry (our $P2_12_12_1$-II). Coh *et al.* [125] employ the notation $\tilde{\alpha}_1$ and $\tilde{\alpha}_1'$ respectively for these two cristobalite structures. Enthalpy-pressure curves for the α-cristobalite and $P2_12_12_1$-II structures lie on top of one another in Fig. 4.2(a), and our calculations give the overall change in enthalpy going from β-cristobalite to $\tilde{\alpha}_1$ or $\tilde{\alpha}_1'$ as −21.2 meV/BeF_2; the equivalent quantity is −34.4 meV/SiO_2 in silica. Above 11 GPa, the $P2_12_12_1$-II structure distorts to the lower space group symmetry $P2_12_12_1$ (#19), and the enthalpy curves for it and the α-cristobalite structure start to diverge (Fig. 4.2(b)).

4.3.3 Open framework structures

The $P2_12_12_1$-I, $C2/c$−4×2 and $P2_1/c$ structures in Fig. 4.2(a) are low-density polymorphs which are previously unreported in BeF_2. The notation '$C2/c$−4×2' refers to the fact that this structure is a low-pressure variant of the '$P2_1/c$ (Z=8), 4×2-type' structure shown in Fig. 4.2(c).

Our DFT−PBE calculations show that these polymorphs are energetically relevant in silica, where they lie 5.5, 15.7 and 5.9 meV/SiO_2 in energy below α-quartz at 0 GPa, which suggests them as likely silica polymorphs as well. The monoclinic angle in the $P2_1/c$ structure is close to 90°, hence we also investigate a higher symmetry version of this structure with $Pnma$ symmetry, whose enthalpy is found to be 2.2 meV/SiO_2 below α-quartz (this structure is not shown in Fig. 4.2(a)). We give the lattice parameters for these four structures in Tables 4.2, 4.3, 4.4 and 4.5 as silica structures at 0 GPa. All four structures have Z=8 (24 atoms) in their conventional unit cells.

Table 4.2: Calculated lattice parameters for the $C2/c - 4 \times 2$ structure. The cell below has full HM symbol $C12/c1$.

Lattice parameters (Å, deg.)			Atom	Atomic coordinates x	y	z	Wyckoff site
a=8.940	b=5.031	c=8.977	Si	0.1877	0.1694	0.3129	8f
α=90.000	β=111.563	γ=90.000	O	0.2055	0.5806	0.7058	8f
			O	0.0000	0.0798	0.2500	4e
			O	0.2500	0.2500	0.5000	4d

Table 4.3: Calculated lattice parameters for the $P2_1/c$ structure. The cell below has full HM symbol $P12_1/n1$ (ITA unique axis b, cell choice 2).

Lattice parameters (Å, deg.)			Atom	Atomic coordinates x	y	z	Wyckoff site
a=8.583	b=9.626	c=5.207	Si	0.0618	0.1781	0.2632	4e
α=90.000	β=89.958	γ=90.000	Si	0.3654	0.3576	0.2649	4e
			O	0.1448	0.0263	0.2455	4e
			O	0.1914	0.2978	0.2191	4e
			O	0.4278	0.3066	0.5443	4e
			O	0.4830	0.3001	0.0441	4e

Table 4.4: Calculated lattice parameters for the $P2_12_12_1$-I structure.

Lattice parameters (Å, deg.)			Atom	Atomic coordinates x	y	z	Wyckoff site
a=5.195	b=8.519	c=9.560	Si	0.2933	0.6088	0.8607	4a
α=90.000	β=90.000	γ=90.000	Si	0.7068	0.1942	0.3192	4a
			O	0.7237	0.1042	0.4693	4a
			O	0.9249	0.3308	0.3101	4a
			O	0.5746	0.7739	0.2020	4a
			O	0.2499	0.5688	0.3056	4a

Table 4.5: Calculated lattice parameters for the *Pnma* structure.

Lattice parameters (Å, deg.)			Atom	Atomic coordinates x	y	z	Wyckoff site
a=9.415	b=5.285	c=8.683	Si	0.6850	0.2500	0.5529	4c
α=90.000	β=90.000	γ=90.000	Si	0.3577	0.2500	0.6389	4c
			O	0.5303	0.2500	0.6363	4c
			O	0.3087	0.2500	0.8176	4c
			O	0.2041	0.4997	0.0538	8d

We also query the ICSD [89] and International Zeolite Association (IZA) [126] crystal structure databases to check if these four structures are already known or predicted for SiO_2.

Our $C2/c$−4×2 structure matches #75654 in the ICSD, which is 'Structure 8' in the simulated annealing structure prediction work of Boisen *et al.* [127], after the latter is relaxed using DFT. However, we find no matching SiO_2 structures in these databases for our $P2_12_12_1$-I, $P2_1/c$ and *Pnma* structures. We use the TOPOS code [128] to examine the topology of the underlying silicon network in all three structures, and this analysis shows that all three are of the 'sra SrAl2 CeCu2 ABW; 4/4/o1' topological type, which is to say the same as the (*Imma*-symmetry) ABW zeolite. They have framework densities of 18.9, 18.6 and 18.5 Si/1000Å^3 respectively; these values can be compared to α-quartz, which has 24.9 Si/1000Å^3. The ABW silica structure itself is slightly less dense at 17.6 Si/1000Å^3, with an enthalpy 3.9 meV/SiO_2 above α-quartz.

While BeF_2 and SiO_2 share many chemical similarities (as mentioned in Sec. 4.1), the Be−F bond is much weaker than the Si−O bond, resulting in a lower melting point and hardness for BeF_2 [122]. Nevertheless, our results show that BeF_2 also supports open framework zeolite-like structures, and highlights the utility of searching for potential zeolite structures in model systems such as BeF_2. The large number of polymorphs we encounter lying close to one another in energy suggest BeF_2 as a potential tetrahedral framework material. The work of Zwijnenburg *et al.* reached a similar conclusion by considering selected known SiO_2 structures for BeF_2 [129], though we remark that our use of structure searching in this chapter was able to recover previously unknown BeF_2 polymorphs in an even tighter energy window.

4.3.4 High−pressure results

Our structure searching calculations show that the application of pressure (0.4 GPa) favours the α-quartz phase, as seen in Fig. 4.2(a). Between 3.1 and 3.3 GPa, the silica 'coesite-I' or 'coesite-II' structure [115] with Z=8 or 32 then becomes the lowest-enthalpy structure for BeF_2. We find that over the pressure range 0−18 GPa, the coesite-I and II structures are nearly identical. The coesite-II structure is close to a supercell of coesite-I, but the atomic positions in coesite-II deviate slightly from those

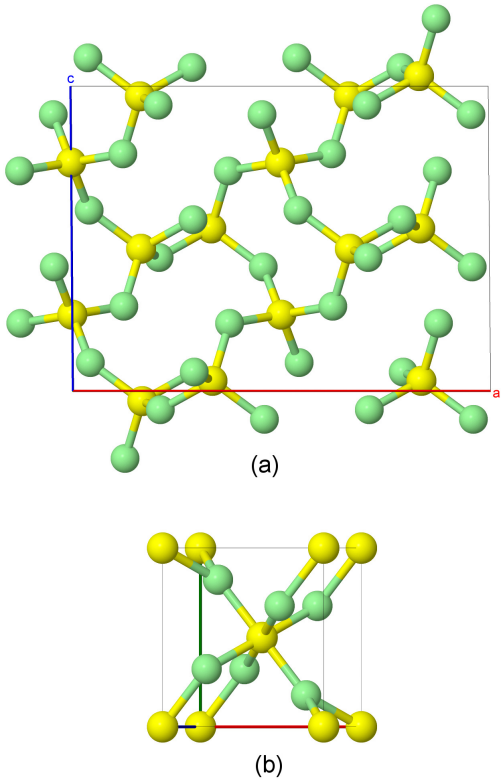

Figure 4.3: (a) BeF_2 in the $C2/c$ moganite phase at 20 GPa with four-fold coordinated Be atoms, viewed down the b (and in this case, monoclinic) axis. The lattice a and c axes point horizontal and almost vertical in the page, respectively. (b) BeF_2 in the $Pnnm$ $CaCl_2$ phase at 50 GPa, with six-fold coordinated Be atoms. Beryllium atoms in yellow, fluorine atoms in green. Lattice parameters and atomic positions for these structures are given in the main text.

expected for a perfect supercell, and the coesite-II structure lies consistently about 1 meV/BeF_2 below coesite-I over this pressure range. The coesite-I phase has been found in experimental studies on BeF_2, at 3 GPa and ≈1100 K [124].

The work of Rakitin *et al.* [116] reported that a new structure of $C2/c$ symmetry then becomes stable between 18 and 27 GPa; our calculations instead show that BeF_2 is most stable in the silica moganite structure, which also has $C2/c$ symmetry, between 11.6 and 30.1 GPa; see Fig. 4.2(b). We show the moganite structure in Fig. 4.3(a). At 20 GPa, for a conventional unit cell with full Hermann-Mauguin (HM) symmetry $C12/c1$, we calculate the lattice parameters a=12.008 Å, b=4.191 Å and c=7.103 Å with a monoclinic angle β=125.818°. Be atoms occupy the $4e$ (0.0000, 0.9572, 0.2500) and $8f$ (0.1658, 0.3268, 0.1989) Wyckoff sites, while F atoms occupy the $8f$ (0.2909, 0.1705, 0.2289), (0.1237, 0.1811, 0.3455) and (0.0421, 0.2694, 0.9492) sites. As a small technical note, the moganite structure depicted in Fig. 4.3(a) uses different lattice vectors to those just discussed here; its lattice is instead obtained using the relations $\mathbf{a}' = \mathbf{a} + \mathbf{c}$, $\mathbf{b}' = -\mathbf{b}$, $\mathbf{c}' = -\mathbf{c}$. This gives a structure with full HM symbol $I12/c1$ and a smaller monoclinic angle ($\beta = 90.446°$).

Above 30.1 GPa, we find that the orthorhombic $CaCl_2$ structure with space group $Pnnm$ becomes stable (Fig. 4.2(b)), eventually giving way to the denser α-PbO_2 structure above 57.5 GPa (Fig. 4.2(c)). BeF_2 in the $CaCl_2$ structure is depicted in Fig. 4.3(b). At 50 GPa, we calculate the lattice parameters a=3.796 Å, b=3.959 Å and c=2.445 Å, and Be atoms occupy the $2a$ (0.0000, 0.0000, 0.0000) Wyckoff site, while F atoms occupy the $4g$ (0.2736, 0.3233, 0.0000) site.

We give the electronic and phonon DOS for the BeF_2 in the moganite and $CaCl_2$ structures in Fig. 4.4. A Gaussian smearing of 0.25 eV is used for the electronic DOS, and we set the valence band maximum (VBM) to 0 eV. The majority contributor (species and orbital) to each feature in this DOS is labelled in Fig. 4.4(a). In both structures, the valence bands consist of fluorine $2p$ orbitals, while the conduction bands come from unoccupied p orbitals in beryllium. The dynamic stability of the predicted structures is indicated by the phonon DOS ((b) in Fig. 4.4) for these structures having no protrusion into negative (imaginary) frequencies, shown as grey regions in that figure.

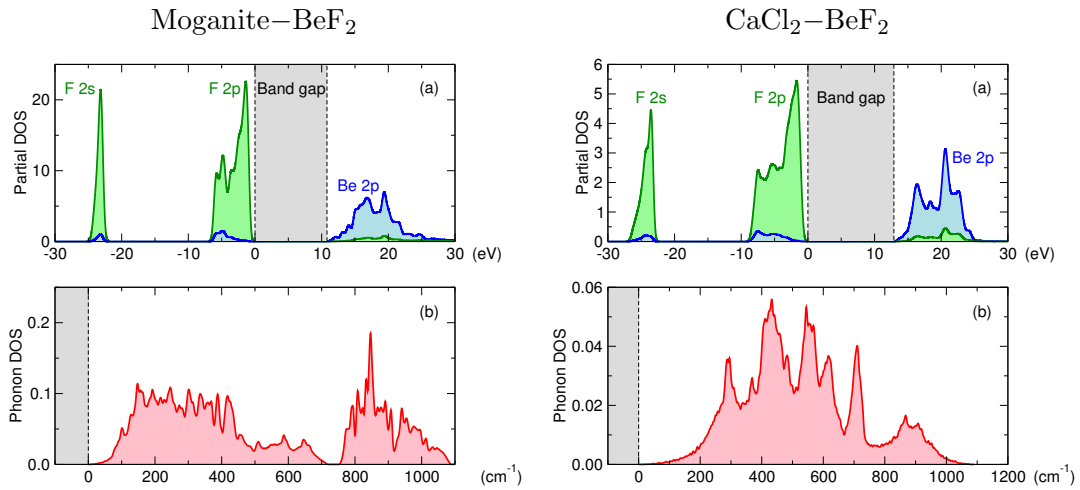

Figure 4.4: Electronic (a) and phonon (b) density of states for the moganite−BeF_2 phase at 20 GPa (left panel), and for the $CaCl_2$−BeF_2 phase at 50 GPa (right panel). A 4×4×3 (864 atom) and 4×4×6 (576 atom) supercell is used for the moganite and $CaCl_2$ phonon calculations, respectively.

As can be seen in Fig. 4.2(c), the enthalpy-pressure curve for the $CaCl_2$ structure emerges smoothly from that for the rutile structure (space group $P4_2/mnm$), which is also the case in silica, where a ferroelastic phase transition occurs between these two structures near 50 GPa [130]. For BeF_2 at the static lattice level, our calculations exclude the stability of the rutile structure over the pressure range 0−70 GPa, though we note that this phase lies only a fraction of a meV per BeF_2 higher in enthalpy than the $CaCl_2$ phase at 30.1 GPa.

Earlier studies [116, 131] have already examined a number of the BeF_2 structures

discussed here. However, the stability of BeF_2 in the moganite and $CaCl_2$ structures is new, and according to our calculations dominates the high-pressure phases of BeF_2 over the pressure range 11.6−57.5 GPa.

Fig. 4.2(c) also shows a band of three enthalpy-pressure curves, labelled *Pbcn* (Z=8), $P2_1/c$ (Z=6) and $P2_1/c$ (Z=8), whose energy lies in close proximity to the α-PbO_2 curve. These three structures emerged from our searches and have a similar, but slightly lower density than the α-PbO_2 phase for BeF_2. They are close to stability at 60 GPa, but are not predicted to be stable over the pressure range 0−70 GPa. We identify these phases as members of the class of silica polymorphs introduced by Teter *et al.* [132], which are a set of structures described as intermediaries to the $CaCl_2$ and α-PbO_2 silica phases. Our *Pbcn* (Z=8) and $P2_1/c$ (Z=6) structures correspond to the '3 × 3' and '3 × 2' structure types, while our $P2_1/c$ (Z=8) structure is not explicitly discussed in Ref. [132] and would be referred to as '4 × 2' type. We will encounter these phases again in our results for MgF_2.

Summary

To briefly summarise our search results for BeF_2 discussed so far, we predict the following series of pressure-induced phase transitions at the static-lattice level:

$$\alpha\text{-cristobalite}\,(P4_12_12) \xrightarrow{0.4\text{ GPa}} \alpha\text{-quartz}\,(P3_121) \xrightarrow{3.1/3.3\text{ GPa}} \text{Coesite-I/II}\,(C2/c)$$
$$\xrightarrow{11.6\text{ GPa}} \text{Moganite}\,(C2/c) \xrightarrow{30.1\text{ GPa}} CaCl_2\,(Pnnm) \xrightarrow{57.5\text{ GPa}} \alpha\text{-}PbO_2\,(Pbcn),$$

with the labelled arrows showing the calculated transition pressures. Our searches also demonstrate numerous metastable polymorphs for BeF_2, both at low pressure (Sec. 4.3.3) and high pressures (this section).

4.3.5 Optical bandgaps in BeF_2

As mentioned in Sec. 4.1, BeF_2 has a large bandgap at ambient pressure and is used in a number of optical applications. We examine the optical bandgap in BeF_2 as a function of pressure, with the results shown in Fig. 4.5.

Optical bandgaps in BeF_2 are calculated for the α-quartz, coesite-I, moganite, $CaCl_2$ and α-PbO_2 structures, over the pressure ranges for which these structures are calculated to be stable at the static-lattice level. We have excluded the small stability range of α-cristobalite BeF_2 (0−0.4 GPa), and use the coesite-I structure instead of coesite-II on the grounds that these two structures are almost identical at low pressures.

The optical gap is found to be tunable, increasing by around 0.06 eV/GPa over the pressure range 0−70 GPa. We expect BeF_2 to therefore maintain its high UV transmittance with increasing pressure, with potentially useful high pressure applications.

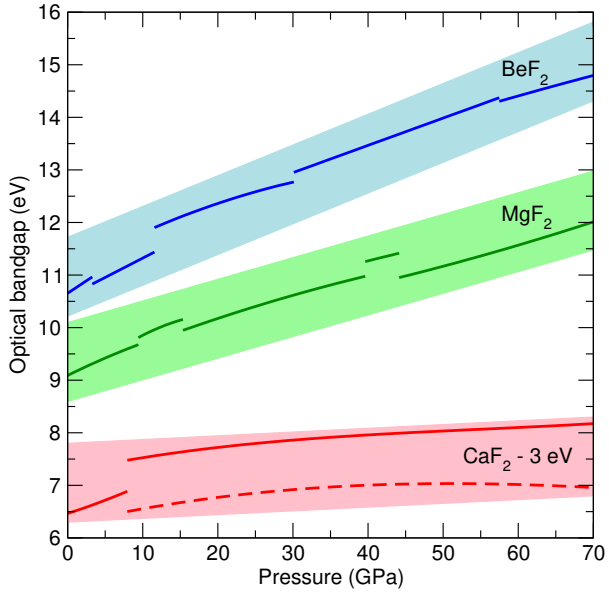

Figure 4.5: Optical bandgaps in Be-, Mg- and CaF_2 within the pressure range 0−70 GPa as calculated using the HSE06 functional. For visibility, the bandgaps in CaF_2 have been shifted down by 3 eV. Discontinuities in the solid curves are due to phase transitions between different structures, while the shaded regions serve to guide the eye. The dashed curve in CaF_2 corresponds to the $P\bar{6}2m$ phase, which is not stable at the static lattice level but which we predict is stabilised by temperature.

4.4 Magnesium difluoride

4.4.1 Results of variable stoichiometry searches

Elemental magnesium undergoes a phase transition from hcp to bcc between about 45 and 60 GPa. Within this pressure range, the coexistence of the hcp and bcc phases is observed at low temperatures [133]. Our PBE−DFT calculations find that the hcp−Mg phase is very slightly lower in enthalpy than bcc−Mg at 60 GPa, so we use the hcp−Mg phase in our Mg-F convex hull calculations.

We construct the convex hull for the Mg-F system as per Sec. 4.3.1, with the results shown in Fig. 4.6. As was the case for BeF_2, MgF_2 is the only stable stoichiometry in the Mg-F system at 60 GPa. We again focus only on the MgF_2 difluoride stoichiometry in subsequent sections.

4.4.2 Difluoride structure searches

MgF_2 adopts the rutile $P4_2/mnm$ structure at room temperature and pressure. X-ray diffraction experiments indicate a transformation to the $CaCl_2$ structure at 9.1 GPa, then to a pyrite structure with space group $Pa3$ and Z=4 near 14 GPa, and have also recovered a mixture of α-PbO_2 and rutile MgF_2 upon decompression [103]. DFT calculations, including those of this chapter, find that the $CaCl_2$ structure is never stable for MgF_2 and instead predict the α-PbO_2 structure to have a window of stability

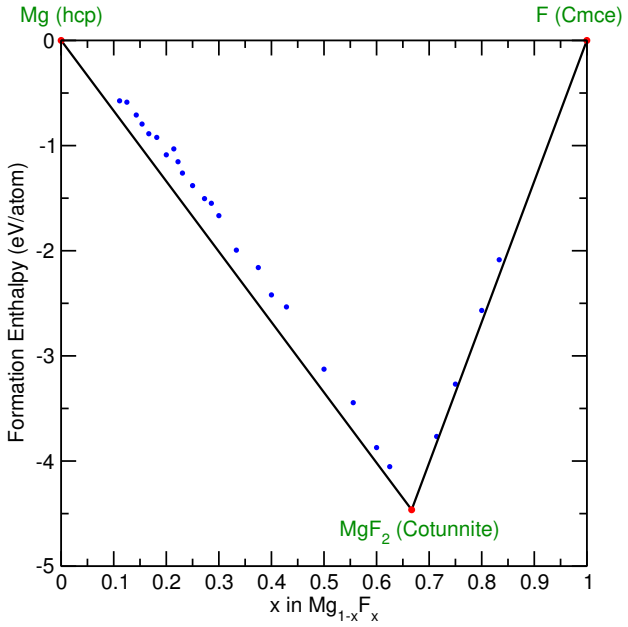

Figure 4.6: Convex hull for the Mg-F system at 60 GPa.

between 10 and 15 GPa, with the $CaCl_2$ structure slightly higher in enthalpy.

The results from our structure searches are given in Fig. 4.7. Based on our static-lattice results, we predict the following sequence of stable structures and phase transitions with rising pressure:

$$\text{Rutile}\,(P4_2/mnm) \xrightarrow{9.4\ \text{GPa}} \alpha\text{-PbO}_2\,(Pbcn) \xrightarrow{15.4\ \text{GPa}} \text{Pyrite}\,(Pa3)$$
$$\xrightarrow{39.6\ \text{GPa}} \text{O-I}\,(Pbca) \xrightarrow{44.1\ \text{GPa}} \text{Cotunnite}\,(Pnma).$$

Previous theoretical studies [134, 135] have already considered the rutile, α-PbO_2, pyrite and cotunnite phases of MgF_2. In the present work, we find that the *Pbca* O-I 'orthorhombic-I' structure, which has been reported experimentally for TiO_2 near 30 GPa [118], is also stable for MgF_2 between 39.6 and 44.1 GPa. This structure is depicted in Fig. 4.8. At 42 GPa, the calculated lattice parameters of this structure are a=4.782 Å, b=4.556 Å and c=8.863 Å; Mg atoms occupy the 8c (0.9586, 0.2259, 0.8870) Wyckoff site, and F atoms occupy the 8c (0.1099, 0.1721, 0.2008) and (0.2339, 0.9977, 0.4653) sites.

The electronic and phonon DOS for O-I−MgF_2 can be seen in Fig. 4.9, with the orbitals labelled as in Fig. 4.4.

Experimental studies on MgF_2 have reported an unidentified 'Phase X' stable in the pressure range 49−53 GPa and at 1500−2500 K between the pyrite and cotunnite phases [136]. Our enthalpy calculations identify the O-I structure as the thermodynamically most likely candidate for Phase X, though the authors of Ref. [136] note some difficulty in indexing x-ray diffraction data for Phase X to an orthorhombic structure,

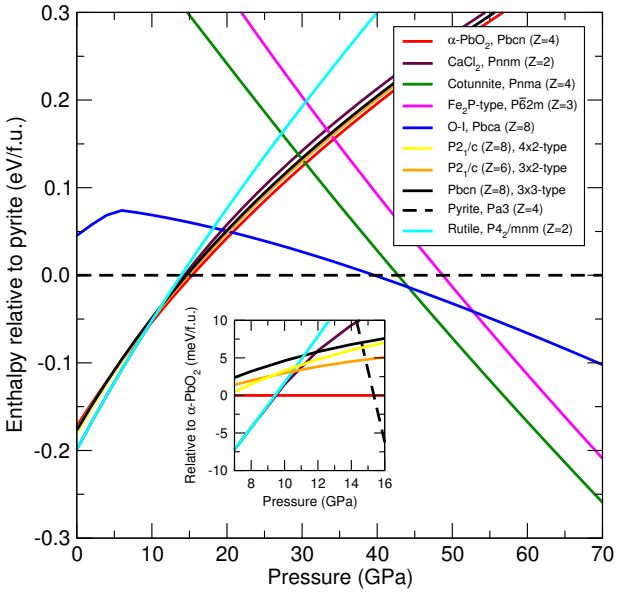

Figure 4.7: Static-lattice enthalpies and results from structure searches on MgF_2 over the pressure range 0−70 GPa. The inset plot shows the small enthalpy differences between a few phases in the vicinity of 10 GPa. Enthalpies are shown relative to the pyrite (main figure) and α-PbO_2 (inset) phases.

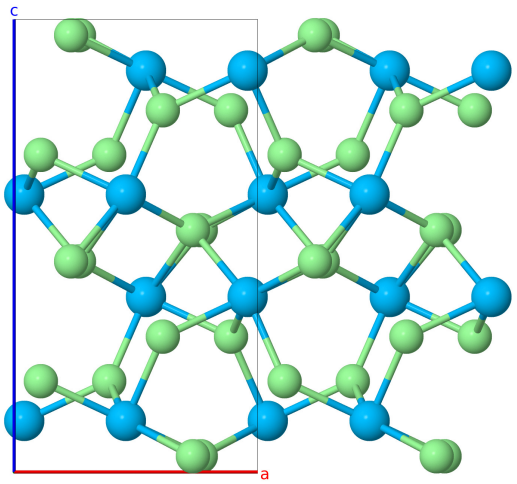

Figure 4.8: 2×1×1 slab of MgF_2 in the *Pbca* 'orthorhombic-I' structure (Z=8), which we predict to be stable between 39.6 and 44.1 GPa. This view looks down the b axis. Magnesium atoms in blue, fluorine atoms in green.

possibly due to a mixture of phases being present. The baddeleyite structure (see Table 4.1) was also discussed as a possibility in Ref. [136], however we find this structure to be energetically unfavourable. We do not find any other energetically competitive structures near 50 GPa.

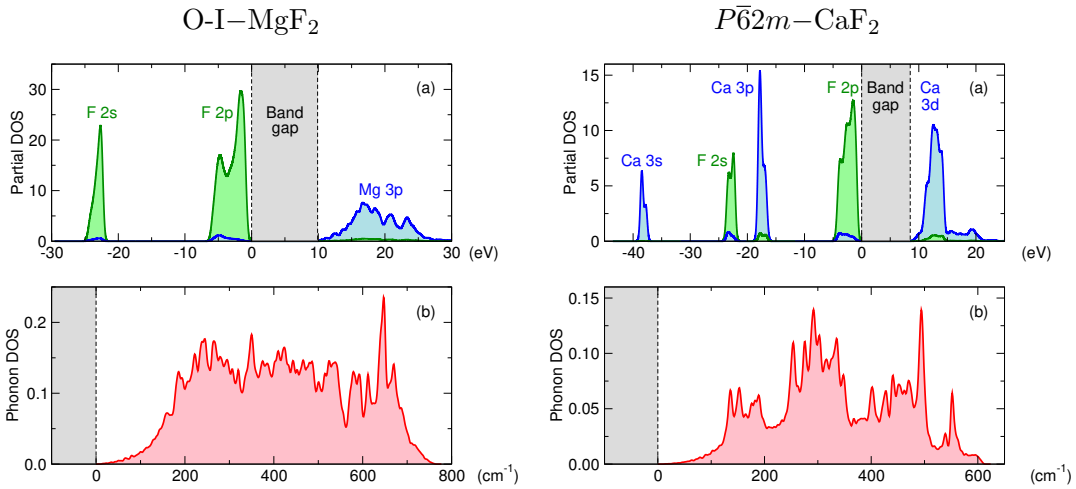

Figure 4.9: Electronic (a) and phonon (b) density of states for the O-I−MgF_2 phase at 42 GPa (left panel), and for the $P\bar{6}2m$-CaF_2 phase at 30 GPa (right panel). A 4×3×2 (576 atom) and 3×3×6 (486 atom) supercell is used for the O-I and $P\bar{6}2m$ phonon calculations, respectively.

4.4.3 MgF_2 as a silica analogue

Silica and its stable polymorphs are of paramount importance in geophysics and planetary sciences. As well as a mineral in its own right, it is expected to be formed from the breakdown of post-perovskite $MgSiO_3$ at terapascal pressures. SiO_2 follows a very similar set of phase transitions to MgF_2 with increasing pressure [137], with the Si coordination number rising from 6 in rutile at ambient pressures to a predicted 10 in an $I4/mmm$ structure near 10 TPa [92]. As pointed out by previous authors, several features of high pressure silica can readily be modelled in MgF_2, but at much lower pressures [103, 136]. For example, the α-PbO_2 → pyrite transition in SiO_2, which our calculations find occurs at 217 GPa, takes place at a much lower pressure of 15.4 GPa in MgF_2. Near 690 GPa and for $T \gtrsim 1000$ K, a pyrite → cotunnite transition is also predicted for SiO_2 [138]; the analogous transition occurs at 44.1 GPa in MgF_2.

As mentioned in Sec. 4.3.4, Teter *et al.* [132] have introduced a class of SiO_2 polymorphs intermediate to $CaCl_2$ and α-PbO_2. At least one member of this class of polymorphs has been synthesised in SiO_2, the '3×2' type $P2_1/c$ structure [139]. The $P2_1/c$ (Z=6), $P2_1/c$ (Z=8) and $Pbcn$ (Z=8) structures of BeF_2 depicted in Fig. 4.2(c) are members of this class, and also turn up in our MgF_2 searches (Fig. 4.7 and its inset). Our calculations show that these polymorphs are closest to stability near 10 GPa in MgF_2, compared to ≈100 GPa in SiO_2 suggesting that, as with other features of silica, they

could be studied experimentally at much lower pressures in MgF_2. We show the enthalpies of some of these polymorphs in Fig. 4.10 in both MgF_2 and SiO_2 to highlight their similar energy ordering.

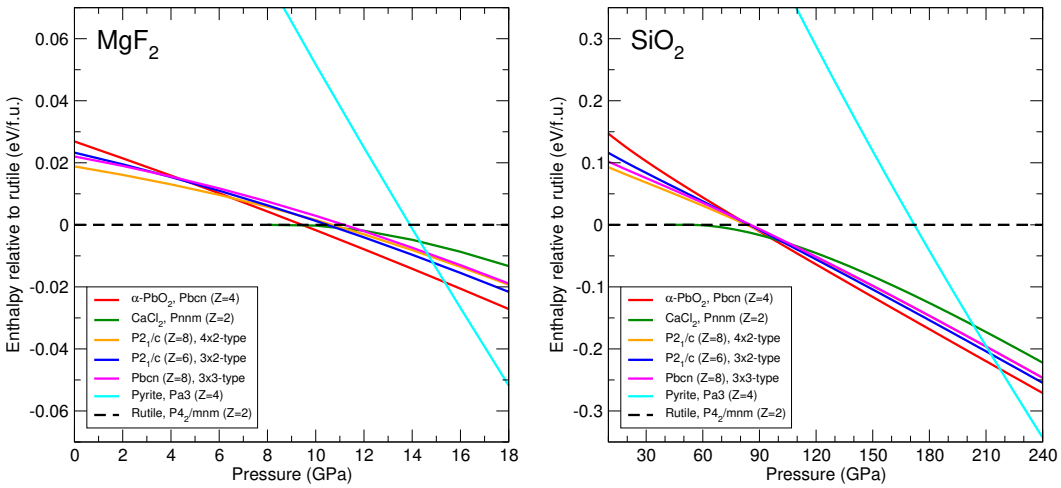

Figure 4.10: Enthalpies of selected MgF_2 and SiO_2 structures shown side-by-side for comparison. MgF_2 models several of the higher pressure phases and phase transitions encountered in SiO_2, but at much lower pressures. Note the different pressure and energy scales.

4.4.4 Optical gaps in MgF_2

Fig. 4.5 shows the optical bandgap in MgF_2 as a function of pressure. Bandgaps are shown for the rutile, α-PbO_2, pyrite, O-I and cotunnite structures. As was found for BeF_2, the optical gap in MgF_2 is tunable with pressure, rising by about 0.04 eV/GPa over 0−70 GPa.

4.5 Calcium difluoride

4.5.1 Results of variable stoichiometry searches

DFT and structure searching calculations predict that the β-tin $I4_1/amd$-symmetry structure is the lowest enthalpy phase for calcium at 60 GPa [140], and we also confirm this with our structure searches. The β-tin phase is well known to be slightly at odds with experimental results, which instead observe simple cubic calcium (or distorted versions of it) at 60 GPa [141], although the β-tin phase has been synthesised near 35 GPa. Our calculated Ca-F convex hull is shown in Fig. 4.11, and we have carried out our convex hull calculations with the lowest enthalpy DFT phase for calcium (β-tin). These results show that both CaF_2 and CaF_3 are stable stoichiometries at 60 GPa.

The predicted CaF_3 structure at 60 GPa is cubic with $Pm\bar{3}n$ symmetry, and the same structure has in fact been previously predicted for high-pressure aluminium hydride

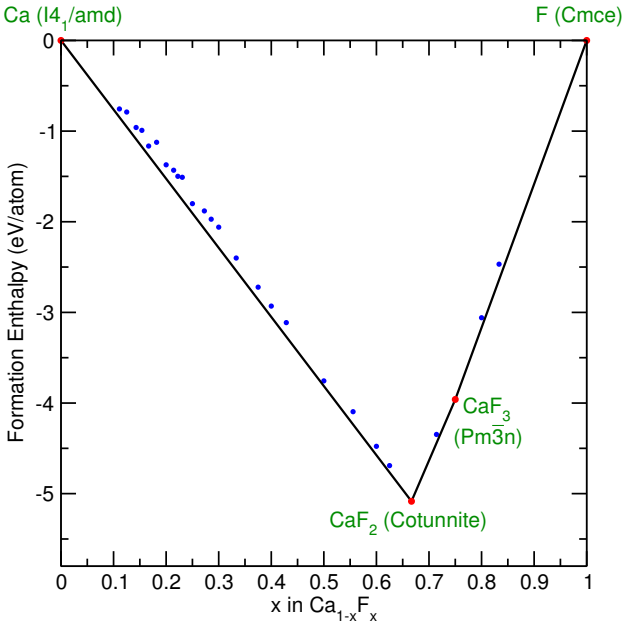

Figure 4.11: Convex hull for the Ca-F system at 60 GPa.

(AlH_3) [113]. In the present chapter, we have not examined the properties of high-pressure CaF_3 further, and in the following sections we again focus only on the CaF_2 difluoride stoichiometry.

4.5.2 Difluoride structure searches

CaF_2 crystallizes in the cubic $Fm\bar{3}m$ 'fluorite' structure (Z=4, α-CaF_2) under ambient conditions. The compound has a high-temperature phase above about 1400 K, known as β-CaF_2, and melts near 1700 K at low pressures [142]. A high-pressure modification above 8−10 GPa (γ-CaF_2) is also known, with CaF_2 taking on the orthorhombic $Pnma$ cotunnite structure (Z=4) [143].

The β phase has attracted considerable interest because it exhibits superionicity, with F^- ions as the diffusing species [144]. A number of other compounds in the same fluorite (or 'anti-fluorite') variants of this structure, such as Li_2O, are also superionic conductors [145]. Such materials are of great technological interest, with applications in solid-state battery design. A recent study has shown that the superionic transition temperature in CaF_2 can be decreased through applied stress [146].

Our results from structure searching in CaF_2 are shown in Fig. 4.12. Unlike BeF_2 and MgF_2, we find that the potential energy surface for CaF_2 is relatively simple, with very few polymorphs for this compound over the pressure range 0−70 GPa. At the static lattice level of theory, we identify only the sequence of stable phases and transitions:

$$\text{Fluorite } (Fm\bar{3}m) \xrightarrow{7.9 \text{ GPa}} \text{Cotunnite } (Pnma).$$

The calculated fluorite → cotunnite transition pressure here is in agreement with ex-

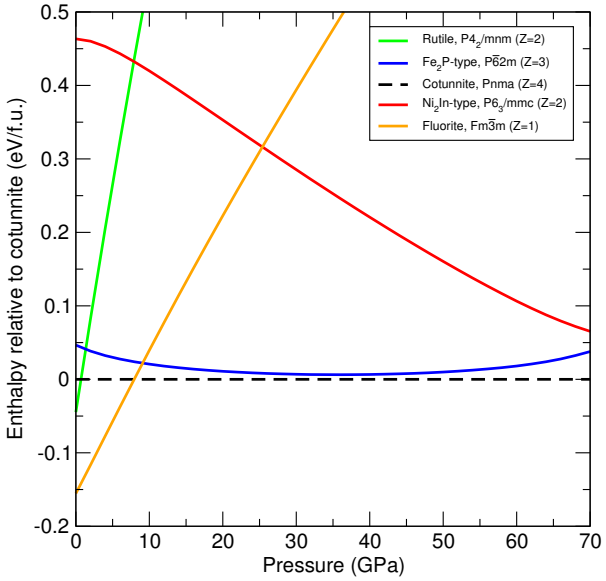

Figure 4.12: Results from structure searches on CaF_2 over the pressure range 0−70 GPa: static-lattice enthalpies relative to the *Pnma* (γ) CaF_2 phase.

perimental results [143].

Experimental studies have also shown a transition from γ-CaF_2 to an Ni_2In-type structure in the pressure range 63−79 GPa with laser heating [147], consistent with the convergence of the red and black-dashed curves in Fig. 4.12.

Our results in Fig. 4.12 reveal a hexagonal phase for CaF_2 with $P\bar{6}2m$ symmetry which is close to stability, lying only 6 meV/CaF_2 higher in enthalpy than the γ phase near 36 GPa. The enthalpy curves for the $P\bar{6}2m$ and γ phases in Fig. 4.12 indicate that these two structures have very similar densities, with $P\bar{6}2m$ slightly denser at pressures below 36 GPa and becoming less dense than γ-CaF_2 at higher pressures. The $P\bar{6}2m$ phase has the Fe_2P structure, which has also been predicted for SiO_2 at very high pressures (>0.69 TPa) and low temperatures [138]. We show the γ and $P\bar{6}2m$ structures in Fig. 4.13. We also give the lattice parameters of this structure in the table below, and show its electronic and phonon DOS in Fig. 4.9.

Table 4.6: Calculated lattice parameters for CaF_2 in the $P\bar{6}2m$ phase at 30 GPa.

Lattice parameters (Å, deg.)			Atom	Atomic coordinates x	y	z	Wyckoff site
a=5.697	b=5.697	c=3.255	Ca	0.0000	0.0000	0.5000	1b
α=90.000	β=90.000	γ=120.000	Ca	0.3333	0.6666	0.0000	2c
			F	0.7433	0.0000	0.0000	3f
			F	0.4126	0.0000	0.5000	3g

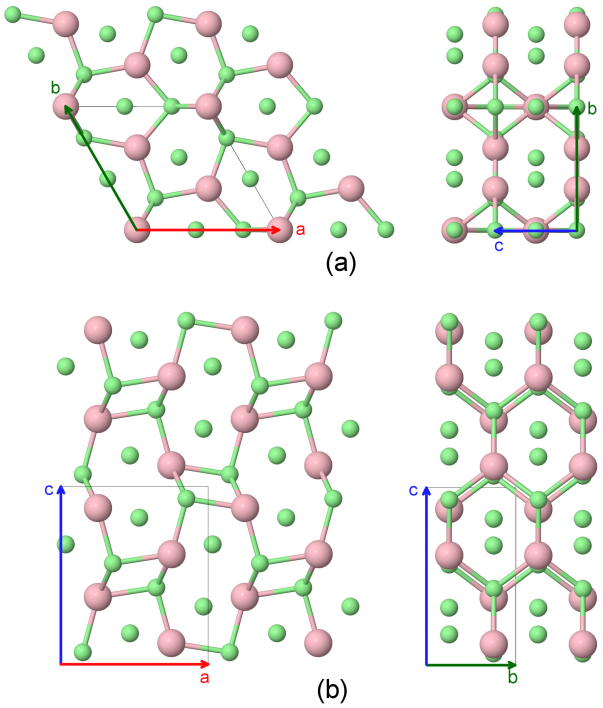

Figure 4.13: 2×2×2 slabs of (a) our predicted $P\bar{6}2m$ structure, and (b) the $Pnma$ structure (phase γ) of CaF_2. Calcium atoms are in red, fluorine atoms in green. In both (a) and (b), the right-hand view is obtained from the left-hand view by rotating the structure by 90° about an axis running vertically up the page.

4.5.3 Pressure-temperature phase diagram for CaF_2

The effects of nuclear zero-point motion and temperature are often important and affect the relative stability of crystal phases, particularly in cases where there are two or more structures lying very close in energy [148, 149]. Given the small enthalpy difference between the $P\bar{6}2m$ and γ CaF_2 phases, we investigate the Gibbs free energy of these structures as a function of pressure, as well as that of $Fm\bar{3}m$-CaF_2. These calculations use the *quasiharmonic approximation* (QHA), which we discuss in more detail below.

We start by performing finite-displacement harmonic phonon calculations (Secs. 2.7.1 and 2.7.4) at several different volumes for the three CaF_2 structures under consideration. We use 5×5×5 (375 atom), 3×3×6 (486 atom), and 5×3×3 (540 atom) supercells for the $Fm\bar{3}m$, $P\bar{6}2m$ and $Pnma$ structures, respectively. Volumes corresponding to the following static-lattice pressures are used for these calculations (all in GPa):

$Fm\bar{3}m$:	−6,	−4,	−2,	0,	4,	8,	12,	16,	20	
$P\bar{6}2m$:	10,	20,	30,	40,	50,	60,	70			
$Pnma$:	0,	2,	6,	10,	20,	30,	40,	50,	60,	70

These results give us the phonon frequencies $\omega_\nu(\mathbf{q})$ at a variety of volumes for each structure.

We are interested in the phonon free energy as a function of volume and temperature, $F(V,T)$. To calculate it, we assume that we can use Eq. (2.55) for $F(V,T)$ at each volume we have calculated the phonon frequencies $\omega_\nu(\mathbf{q})$. This is the essence of the QHA: we assume that the phonon frequencies $\omega_\nu(\mathbf{q})$ depend on V only (and not T), and we calculate harmonic phonon frequencies at each V.[1]

We fit the resulting free energies calculated with the QHA using a polynomial in V, at each temperature T. For the $Fm\bar{3}m$ and $P\bar{6}2m$ structures, the calculated $F(V,T)$ values vary reasonably slowly with volume and are well reproduced by a quadratic in V. For the $Pnma$ structure, we find that the calculated $F(V,T)$ values tend to initially increase rapidly with decreasing volume, but then increase less rapidly at lower volumes (at fixed T). A cubic polynomial in V is therefore used to capture this trend. We show the calculated $F(V,T)$ values, and the corresponding polynomial fits, in Fig. 4.14.

Some insight into this behaviour of $F(V,T)$ in the $Pnma$ structure can be found by looking at the dependence of the lattice parameters of all three structures on V. For $Fm\bar{3}m$ and $P\bar{6}2m$, the lattice parameters steadily decrease on compression. The $Pnma$ structure, however, shows slightly unusual behaviour on compression in that lattice parameter a initially decreases, but then starts increasing for static-lattice pressures above 56 GPa, while lattice parameter c decreases more rapidly at that pressure as well (Fig. 4.15).

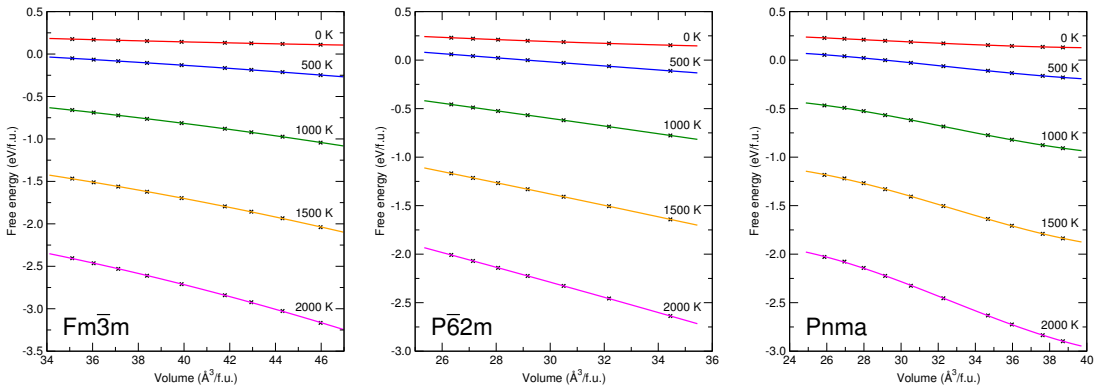

Figure 4.14: Phonon free energies $F(V,T)$ for the $Fm\bar{3}m$ (*left*), $P\bar{6}2m$ (*middle*) and $Pnma$ (*right*) structures of CaF_2, as a function of volume and of temperature. The small '×' marks indicate values from supercell calculations, while the solid curves show the resulting polynomial fits.

As well as providing relaxed geometries for our calculations, static-lattice calculations give us sets of enthalpies H, volumes V and static-lattice pressures P_{st} as calculated using Eqs. (2.41) and (2.42); the latter quantity is sometimes referred to as the *electron* pressure. Within the QHA, at a given volume V, the corresponding Gibbs free energy

[1] Specifically, in the way we have used this approximation here, this is referred to as the *statically-constrained* quasiharmonic approximation, because the structures we use at each volume V are relaxed in the static-lattice approximation only [150], and the phonon pressure and stress is taken to be isotropic.

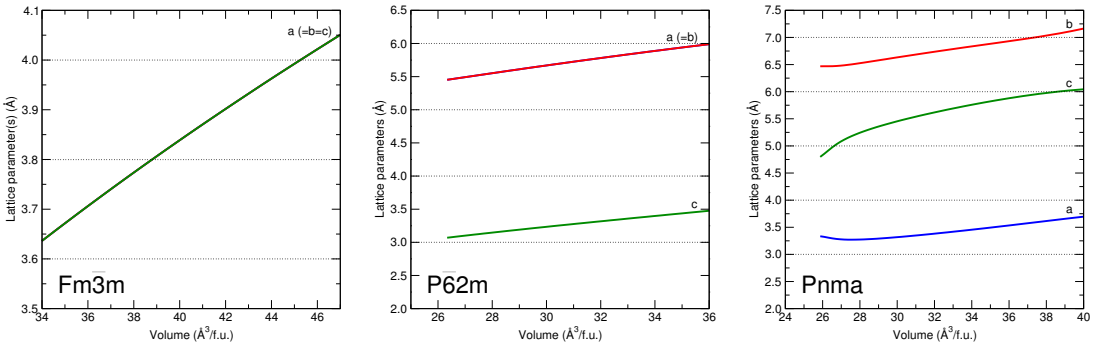

Figure 4.15: Lattice parameters of the $Fm\bar{3}m$ (*left*), $P\bar{6}2m$ (*middle*) and $Pnma$ (*right*) structures of CaF_2 as a function of volume, calculated at the static lattice level. The lattice parameter for $Fm\bar{3}m$ is given for the primitive cell (Z=1, a=b=c, α=β=γ=60°); the lattice parameter for the corresponding conventional cell (Z=4) is $\sqrt{2}$ times larger. Our simulation cell for the $Pnma$ structure has $a < c < b$, and is actually in the alternative $Pmcn$ setting for that space group (#62).

is the sum of the electronic enthalpy and phonon Gibbs free energy:

$$G(V,T) = H(V) + F(V,T) + P_{ph}V, \tag{4.3}$$

and the corresponding pressure P at that volume is:

$$P = P_{st} + P_{ph}, \tag{4.4}$$

where $P_{ph} \equiv -\partial F(V,T)/\partial V$ is the phonon pressure.

We carry out our calculations of $G(V,T)$ and P using these equations, and selecting the lowest Gibbs free energy structure at each temperature and pressure gives the phase diagram shown in Fig. 4.16. We do not carry out any calculations of the melting temperature of CaF_2; instead, the dotted-black solid-liquid phase boundary in Fig. 4.16 is taken from a simple linear fit to results appearing in the work of Cazorla *et al.* [151], although we note that the melting temperature of the $P\bar{6}2m$ structure discussed here is not assessed in that work.

On the basis of our calculated phase diagram, we predict that the $P\bar{6}2m$-CaF_2 structure is stabilised by temperature, in the region $P \gtrsim 10$ GPa and $T \gtrsim 1500$ K.

Both the $Fm\bar{3}m$ and $P\bar{6}2m$ structures develop unstable or 'negative' phonon modes at sufficiently large volumes (see the discussion following Eq. (2.53)). For $Fm\bar{3}m$-CaF_2, these first occur at a static-lattice pressure between -7 and -6 GPa; for $P\bar{6}2m$ they first occur between 0 and 1 GPa. Cazorla *et al.* also report unstable phonon modes for $Fm\bar{3}m$-CaF_2 above 4.5 GPa [151], however we do not encounter any such instabilities in our calculations. We find no unstable phonon modes in γ-CaF_2. In Fig. 4.16, black dashed lines are used to divide the regions of stability for the $Fm\bar{3}m$ and $P\bar{6}2m$ structures in two. At temperatures below the lines, these phases have volumes corre-

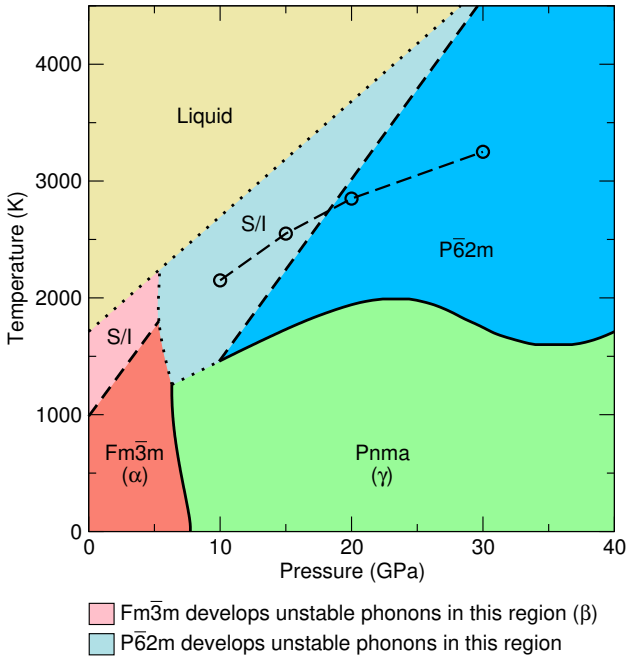

Figure 4.16: Calculated quasiharmonic phase diagram of CaF_2. We find the known $Fm\bar{3}m$ (α) and $Pnma$ (γ) phases at low temperature, but our calculations indicate that a previously unreported phase of $P\bar{6}2m$ symmetry becomes stable at high temperature and pressure. Dashed lines show boundaries due to unstable phonons at the quasiharmonic level, and per the discussion in the text, 'S/I' indicates the superionic regions of the phase diagram. The set of four open circles ○ connected by dashed lines show the predicted temperatures for the $P\bar{6}2m \rightarrow Im\bar{3}m$ substructural rearrangement of the Ca sublattice from classical MD simulations; see Sec. 4.5.5 for further discussion.

sponding to stable phonons, while above the lines they exhibit unstable phonon modes, and their Gibbs free energies are extrapolations of quasiharmonic results. Dotted lines separate regions where one or both phases have unstable phonon modes, with the exception of the solid-liquid boundary.

We have also looked at whether using a different fit form for our free energies (other than a polynomial in V) affects the phase diagram. For example, the authors of Ref. [138] calculate phase diagrams for SiO_2, $MgSiO_3$ and $CaSiO_3$ by fitting the *total* free energy to a Birch-Murnaghan equation of state (EOS) [152]. In our notation, we would write $H(V) = U(V) + P_{st}V$ in Eq. (4.3) where U is the internal energy, and the total free energy is the quantity $U(V) + F(V,T)$. We find that this alternative method does not change the topology of our calculated phase diagram but it does cause a small shift in the phase boundaries.

4.5.4 Validity of the quasiharmonic approximation

The (calculated) volume coefficient of thermal expansion:

$$\alpha(P,T) \equiv \frac{1}{V}\left(\frac{\partial V}{\partial T}\right)_P \tag{4.5}$$

can be used to assess the validity of the QHA. According to the criteria of Karki *et al.* [153] and Wentzcovitch *et al.* [154], we can consider the QHA valid at temperatures lower than the higher temperature inflection point in $\alpha(P,T)$, i.e., where

$$\left[\frac{\partial^2\alpha(P,T)}{\partial T^2}\right]_P \tag{4.6}$$

changes sign. At temperatures beyond this point, we generally find that $\left[\frac{\partial^2\alpha(P,T)}{\partial T^2}\right]_P \geq 0$ and the QHA is expected to be less applicable with further increases in temperature as anharmonic phonon effects become more important.

For the $Fm\bar{3}m$ and $P\bar{6}2m$ structures, Fig. 4.17 shows $\alpha(P,T)$ at a variety of pressures. The aforementioned inflection point in $\alpha(P,T)$ is shown using open circles at each pressure. Fitting the resulting (P,T) coordinates of these inflection points gives us the validity rule:

$$T\ (K) \leq 28P\ (\text{GPa}) + 453 \tag{4.7}$$

for our use of the quasiharmonic approximation in Fig. 4.16.

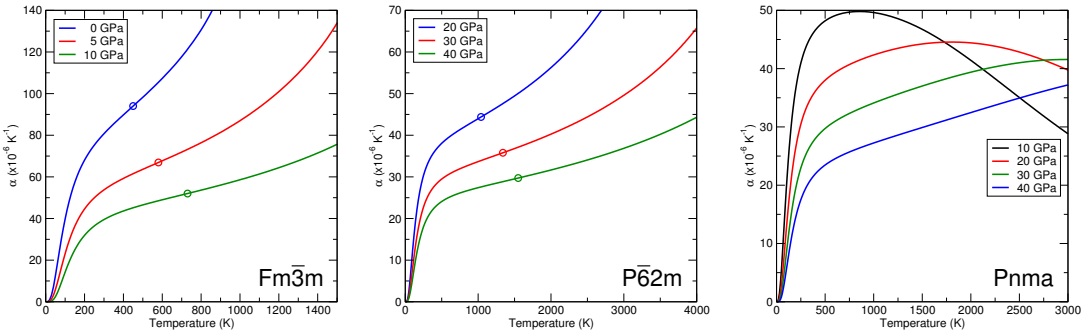

Figure 4.17: Calculated volume thermal expansion coefficients $\alpha(P,T)$ at a variety of pressures as a function of temperature for the $Fm\bar{3}m$ (*left*), $P\bar{6}2m$ (*middle*) and $Pnma$ (*right*) CaF_2 structures. The open circles in the left and middle panels show inflection points, where $d^2\alpha/dT^2$ changes sign.

We note that locating the inflection point is subject to some numerical uncertainty, because $\alpha(P,T)$ changes quite slowly in the vicinity of this point (see Fig. 4.17). We therefore attach an uncertainty of roughly 100 K to this validity rule. In light of this, the lower half of the α-γ phase boundary in Fig. 4.16, and the γ-$P\bar{6}2m$ phase boundary near 40 GPa, are expected to be accurate within the QHA.

This inflection point is harder to locate in the $\alpha(P,T)$ curves for the $Pnma$ structure. The thermal expansion coefficients are slightly unusual in that they initially increase, but then decline at higher temperatures. This is partly due to the fact that the phonon pressure in $Pnma$ declines at higher volumes, as can be seen in the slope of the $F(V,T)$ curves for $Pnma$ in the right−hand panel of Fig. 4.14.

4.5.5 Superionicity in CaF_2

As mentioned in Sec. 4.5.2, fluorite CaF_2 (α-CaF_2) has a known high temperature modification (β-CaF_2) which is superionic. In this section, we spend some time investigating superionicity in CaF_2, primarily in the $P\bar{6}2m$ phase which our QHA results (Fig. 4.16) predict is stabilised at high temperature and pressure. We carry out our analysis through a detailed discussion of phonon modes, and through classical molecular dynamics simulations.

The onset of superionicity in β-CaF_2 has been discussed in connection with the formation of unstable phonon modes in the fluorite CaF_2 structure [155]. Indeed, this is the criterion we have used in Fig. 4.16, where we label the region where $Fm\bar{3}m$-CaF_2 has unstable phonons as superionic ('S/I'), or β. Rigidly applying this criterion, the α-β transition is calculated to occur at ≈1000 K at 0 GPa, which is in rough agreement with the experimentally observed transition temperature of 1400 K, considering that the QHA should be inaccurate near unstable phonon modes. Accordingly, we expect that the QHA can only deliver qualitative results with respect to the exact superionic transition temperature. The formation of unstable phonons creates an effective 'double-well' energy potential with respect to displacement along the phonon mode, which can push atoms away from their equilibrium positions and favour the creation of defects. Superionic behaviour in general has also been rationalised in terms of the energetic costs of forming defects, such as Frenkel defects [156].

Fig. 4.18(a) shows the phonon dispersion relations in $Fm\bar{3}m$-CaF_2 at a static-lattice pressure of 0 GPa, while Fig. 4.18(b) shows how unstable modes develop in this structure with increasing volume (decreasing static-lattice pressure). Unstable phonon modes are first encountered at the Brillouin zone X point. The corresponding atomic displacements in this unstable mode leave Ca^{2+} ions fixed, while F^- ions are displaced along the [100], [010] or [001] directions (referred to a conventional cubic cell for $Fm\bar{3}m$-CaF_2). The connection to superionicity is that these directions also correspond to easy directions for F^- ion diffusion in the fluorite structure, and are almost barrierless at volumes corresponding to unstable X phonons [157].

Fig. 4.18(b) also shows that at even larger volumes, unstable phonon modes develop at the Brillouin zone W point and that the entire $W-X$ branch becomes soft. As is the case at X, the corresponding phonon modes involve only F^- ion displacements, though in different directions: at W, F^- ions displace along the [011] and [0-11] directions. This may explain the observed gradual onset of superionicity in the fluorite structure [158]: as volume increases, further low-energy diffusion pathways corresponding to unstable phonon modes are opened up in the lattice.

Fig. 4.19 shows the phonon dispersion relations in our predicted $P\bar{6}2m$ structure. With increasing volume, this structure first develops unstable phonon modes at the Brillouin zone K point, and the atomic displacements of Ca^{2+} and F^- ions in the corresponding

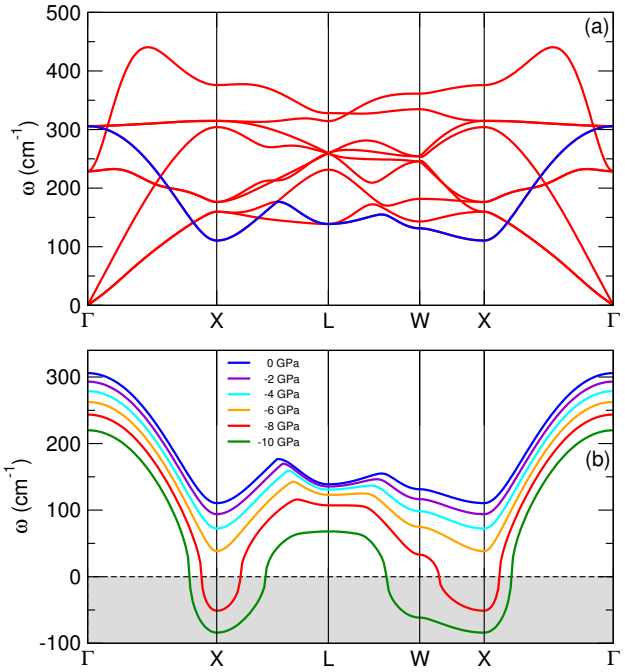

Figure 4.18: Softening of phonon modes in the fluorite $Fm\bar{3}m$-CaF_2 structure. (a) Phonon dispersion curves of this structure at a static-lattice pressure of 0 GPa (cell volume 41.79 Å^3/f.u.). (b) The blue-coloured mode in (a) as a function of decreasing static pressure, from 0 to −10 GPa. The mode softens and first develops imaginary phonon frequencies at X (shown as negative frequencies).

mode are depicted in Fig. 4.20.

This mode is similar to the unstable mode found in fluorite CaF_2 at X, in the sense that it involves displacements of F^- ions and a sublattice of Ca^{2+} ions which remain fixed. F^- ions move along the [120], [210] or [1-10] directions, and all displacements are confined to the *ab*-plane. The $P\bar{6}2m$ structure can be visualised as layer-like: in Fig. 4.20, all atoms that are linked by bonds belong to the same layer, and all 'isolated' atoms belong to a different layer. We find that Ca^{2+} ions in alternating layers remain fixed in the unstable phonon mode. By analogy with fluorite CaF_2, we propose that $P\bar{6}2m$-CaF_2 also undergoes a superionic phase transition accompanying this phonon mode, and we label the region where the $P\bar{6}2m$ structure has unstable phonon modes in Fig. 4.16 as superionic ('S/I'). As is the case for the fluorite structure, it is possible that other compounds in the $P\bar{6}2m$ structure could also exhibit superionicity.

To further investigate the behaviour of $P\bar{6}2m$-CaF_2 at high temperatures and pressures, we carry out some classical molecular dynamics simulations on this structure using the potentials described in Sec. 4.2.2. An orthorhombic simulation cell, with lattice vectors $\mathbf{a}_o$, $\mathbf{b}_o$, and $\mathbf{c}_o$ is constructed from the hexagonal unit cell of the $P\bar{6}2m$ structure through the relations $\mathbf{a}_o = \mathbf{a}_h$, $\mathbf{b}_o = \mathbf{a}_h + 2\mathbf{b}_h$, $\mathbf{c}_o = \mathbf{c}_h$, where $\mathbf{a}_h$, $\mathbf{b}_h$, and $\mathbf{c}_h$ are the lattice vectors of the hexagonal cell. This orthorhombic cell has 18 atoms (twice that of the conventional cell). From this orthorhombic cell, a 9×6×16 simu-

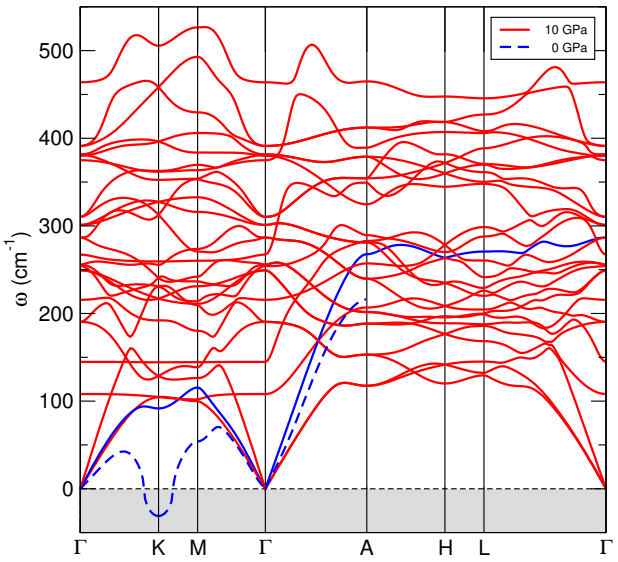

Figure 4.19: Phonon dispersion curves for the proposed $P\bar{6}2m$-CaF_2 structure. This phase has stable phonons at a static pressure of 10 GPa (cell volume 34.45 Å^3/f.u.). The mode coloured blue softens and becomes unstable at the Brillouin zone K point with decreasing pressure, as shown by the blue dashed curve. Only the portion from Γ to A is shown at 0 GPa.

lation box containing 15,552 atoms is created. We remark here that this particular size simulation box is commensurate with the unstable phonon mode at K shown in Figs. 4.19 and 4.20.

Following this, the simulation box is evolved in the constant-stress NPT ensemble in which the lattice parameters, but not cell angles, are allowed to vary.[2] The simulation box is initialised at 10 K for 30 ps, then warmed to 100 K over 30 ps, and thereafter run at 100 K for 30 ps. This process, of warming over 30 ps followed by a run over 30 ps, is then repeated in 100 K increments. We examine the mean-squared displacement (MSD) of calcium and fluorine atoms as a function of temperature; in practice, this calculation uses the built-in `compute msd` LAMMPS command which automatically accounts for effects such as atoms passing through periodic boundaries. As we are working in the NPT ensemble, we check that fluctuations in the lattice parameters are sufficiently small - i.e., that the simulation is in pressure equilibrium - before calculating mean-square displacements.

At a pressure of 30 GPa, we show the results of our MSD calculations on $P\bar{6}2m$-CaF_2 at temperatures of 2000, 2500, 3000 and 3500 K in Fig. 4.21. We split the calculation of the MSD of Ca ions into those on the Wyckoff 2c sites, and those on the Wyckoff 1b sites; see Table 4.6. Note that the unstable phonon mode seen in the $P\bar{6}2m$ structure in Fig. 4.20 leaves 1b-Ca ions stationary, while 2c-Ca ions have a non-zero amplitude in this mode.

[2]Tests on smaller simulation boxes show that allowing the lattice angles to vary does not affect the results discussed here; they are found to fluctuate about 90°.

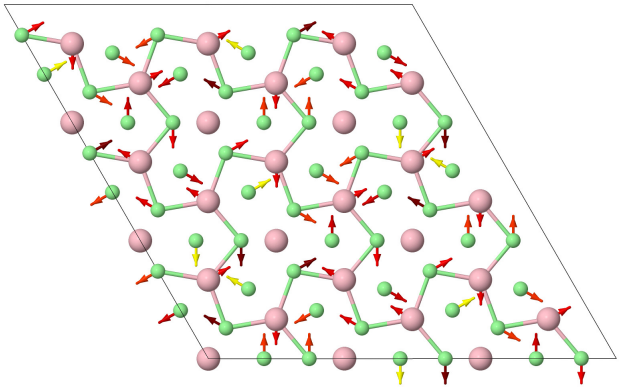

Figure 4.20: Illustration of the unstable phonon mode in $P\bar{6}2m$-CaF_2 at the Brillouin zone K point, shown here at 0 GPa. A 3×3×1 slab of the structure is depicted, viewed along the c-axis as in the left-hand panel of Fig. 4.13(a). Arrows indicate the direction of movement of atoms in this mode, and are colour-coded according to their relative amplitudes: yellow for largest amplitude, through to dark red for smallest amplitude. Calcium atoms are in red, fluorine atoms in green.

At T = 2000 K and 2500 K, the MSD for all ions (both Ca and F) is a constant, and the ions vibrate about their equilibrium positions in the $P\bar{6}2m$ structure. At T = 3000 K, the MSD for Ca ions is still constant, but the MSD for F shows linear growth with simulation time. This behaviour is indicative of F^- ion diffusion. For diffusing particles, we expect that at large times t (see p191 of [159]):

$$\mathrm{MSD}_\alpha \longrightarrow B_\alpha + 6D_\alpha|t|, \tag{4.8}$$

where MSD_α is the mean-square displacement of species α, and B_α and D_α are constants. The value D_α is known as the *tracer diffusion coefficient* for species α.

At T = 3500 K, we observe strong F^- ion diffusion. Unlike T = 2000, 2500, and 3000 K, we also find that the MSD for 1b-Ca and 2c-Ca are nearly the same at T = 3500 K, whereas for these other temperatures the MSD for 1b-Ca is consistently lower than that for 2c-Ca. While it is not evident from Fig. 4.21, we find that the reason for this behaviour is that the Ca-ion sublattice undergoes a structural phase transition between 3000 and 3500 K, which leaves 1b-Ca ions in the structure in place, but sees 2c-Ca ions displace away from their positions in the $P\bar{6}2m$ structure. This behaviour echoes that of the unstable phonon mode at K in the $P\bar{6}2m$ structure, and it is possible that this unstable mode drives both the structural rearrangement and the transition to a superionic state. Our analysis shows that the resulting Ca sublattice is body-centered cubic ($Im\bar{3}m$ symmetry), with Z=2 in a conventional unit cell. The transition is accompanied by a volume increase of about 2.1%, largely as a result of expansion along the c-axis.

While Fig. 4.21 only shows results at P = 30 GPa, similar results are found at other pressures. In the phase diagram of Fig. 4.16, the open circles and dashed lines show the temperatures at which we observe this rearrangement of Ca ions from $P\bar{6}2m$ symmetry

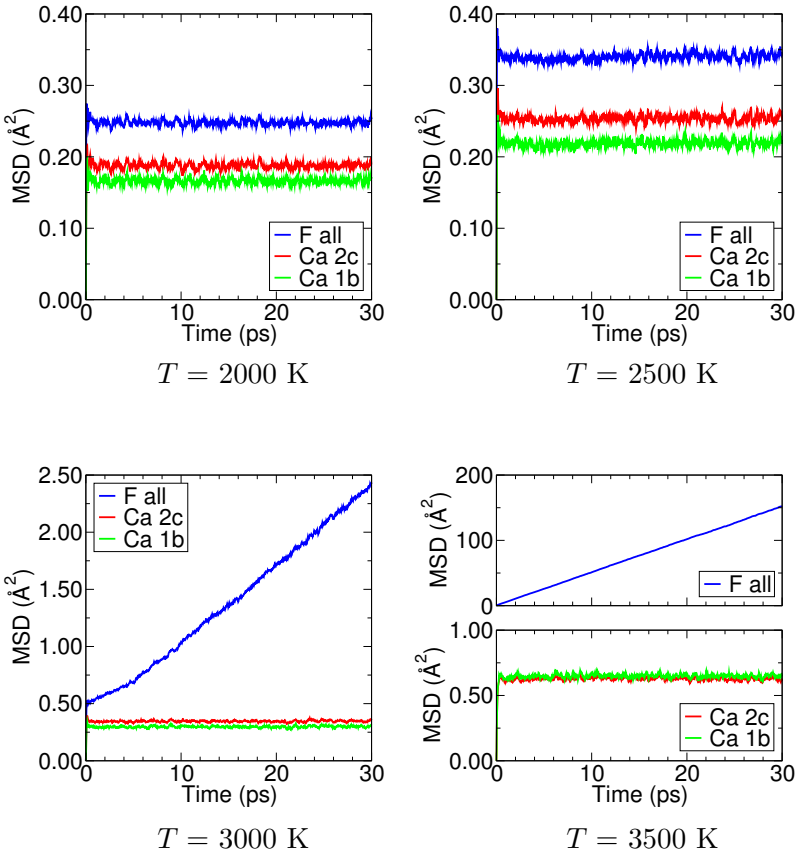

Figure 4.21: Calculated mean-square displacements for Ca and F in $P\bar{6}2m$-structured CaF_2 at 30 GPa, from classical molecular dynamics simulations. The MSD calculations for Ca are split into those on the 2c Wyckoff sites, and those on the 1b sites. Note the different scales on the vertical axes of these graphs. Because the MSDs differ considerably for Ca and F at $T = 3500$ K, this plot has been split into two subplots; one for Ca and one for F.

to $Im\bar{3}m$ symmetry in our classical molecular dynamics simuations. The uncertainty in T for these data should be around ± 50 K because our simulations used 100 K increments.

A straight-line fit to the F^- MSD calculations in Fig. 4.21 allows us to calculate the diffusion coefficient D_F for fluoride ions by virtue of Eq. (4.8). Working at 3000 and 3500 K, the results of this calculation are given in Table 4.7. The last 20 ps of molecular dynamics trajectory in Fig. 4.21 is fitted with a straight line for these calculations. If we further assume that the Nernst-Einstein equation:

$$\sigma_F = \frac{H_R z_F^2 e^2 D_F n_F}{k_B T}, \tag{4.9}$$

applies in this situation, we can estimate the ionic conductivity σ_F from the diffusion coefficient D_F. The other quantities entering this equation are the Haven ratio H_R (see e.g. p193 of [159]), which measures the correlation between the diffusion of different ions and which we take to be 1 (uncorrelated), the valence of the fluoride ions z_F (which

is -1), the elementary charge e, and the number density of mobile fluoride ions n_{F}, which we just take to be the total number density of fluoride ions. Because of these simplifying assumptions, our estimate of σ_{F} should be considered approximate. Again, the results of these calculations are tabled in Table 4.7.

Table 4.7: Calculated diffusion coefficients and ionic conductivities at 3000 K and 3500 K for $P\bar{6}2m$-CaF_2 from classical molecular dynamics simulations. These results are for $P =$ 30 GPa.

T	Slope	D_{F}	n_{F}	σ_{F}
3000 K	0.0694 Å^2/ps	0.116×10^{-5} cm^2/s	6.053×10^{22} cm^{-3}	4.3×10^{-2} Ω^{-1}cm^{-1}
3500 K	5.0247 Å^2/ps	8.374×10^{-5} cm^2/s	5.827×10^{22} cm^{-3}	2.6 Ω^{-1}cm^{-1}

To wrap up our discussion on the unstable phonon modes in $Fm\bar{3}m$ and $P\bar{6}2m$-CaF_2, Fig. 4.22 shows the smallest mode frequency at X and W as a function of volume for the $Fm\bar{3}m$ structure. The solid blue points in Fig. 4.22 were obtained using a 2×4×4 supercell (96 atoms) for $Fm\bar{3}m$, as the X and W points are both commensurate with a supercell of this size (see Eq. (2.59)). For comparison, red crosses in Fig. 4.22 show the results obtained using a 5×5×5 supercell (375 atoms), the size used in our phase diagram calculations. The X and W points are not commensurate with this supercell, so the frequencies shown with red crosses have been obtained by interpolation. These results differ from the exactly commensurate 2×4×4 supercell results by <4 cm^{-1}. The thin solid and dotted black lines connecting the blue points are shape−preserving interpolants fitted to the data and are intended to guide the eye.

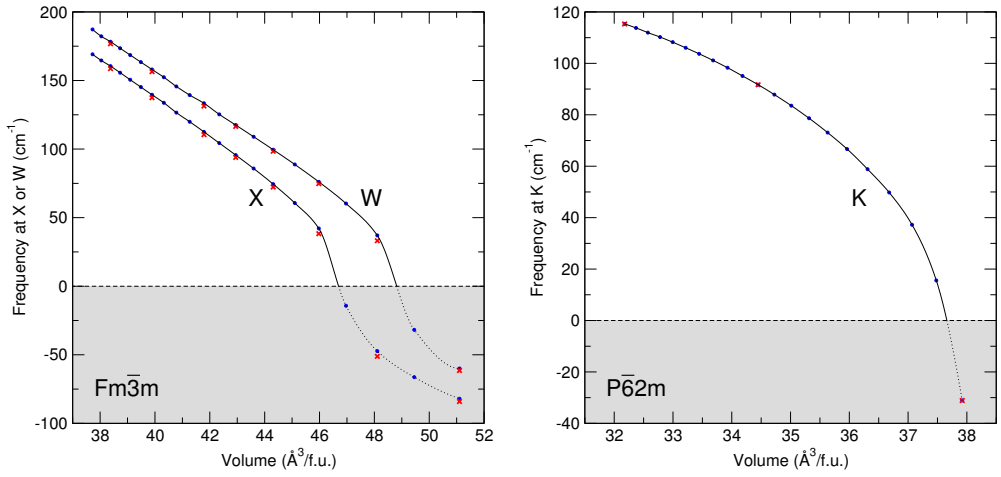

Figure 4.22: (*Left*) Lowest mode frequency at the Brillouin zone X (left−hand curve) and W (right−hand curve) points for $Fm\bar{3}m$-CaF_2, as a function of volume. (*Right*) Mode frequencies at the Brillouin zone K point for $P\bar{6}2m$-CaF_2 as a function of volume. Imaginary frequencies are shown as negative values.

For the $P\bar{6}2m$ structure, the right−hand panel of Fig. 4.22 shows the lowest mode frequency at K as a function of volume. The solid blue points are obtained using a

3×3×1 supercell (81 atoms) commensurate with K, while the red crosses show results using a 3×3×6 supercell (486 atoms), as used in our phase diagram calculations. In this case, K is also commensurate with this larger supercell. The thin solid and dotted black lines are again guides to the eye.

The volume at which these structures first develop imaginary phonon frequencies directly affects the phase diagram of Fig. 4.16. In particular, this volume determines the location of the dashed lines between the red/light−red and blue/light−blue regions of the phase diagram. We have taken this volume to be simply halfway between the first blue point in Fig. 4.22 with a frequency >0 cm^{-1}, and the first 'negative-frequency' blue point. For $Fm\bar{3}m$, this corresponds to $V = 46.47$ Å^3/f.u., and is at a static−lattice pressure between −7 and −6 GPa. For $P\bar{6}2m$, we have $V = 37.70$ Å^3/f.u., occurring between 0 and 1 GPa.

The pressure-temperature phase diagram of CaF_2 has recently been examined by Cazorla *et al.* [151, 160]. In addition to the known α, β and γ phases, the authors propose a high-temperature phase transition from γ to a new δ phase, which in turn is predicted to undergo a superionic transition at even higher temperatures, to a phase labelled ϵ-CaF_2. A $P2_1/c$ symmetry structure was proposed for the δ-phase [151], however we find that this structure is close to $Pnma$ symmetry, and relaxing it using DFT gives the γ-CaF_2 structure. The phase diagram of Fig. 4.16 is in qualitative agreement with these results, where we identify the δ phase with our predicted $P\bar{6}2m$ structure, and the ϵ superionic phase with the region where $P\bar{6}2m$ has unstable phonon modes.

4.5.6 Optical bandgaps in CaF_2

Our calculations show that optical bandgaps in CaF_2 initially increase but then remain relatively constant over the pressure range 0−70 GPa (Fig. 4.5). We show optical bandgaps for the fluorite and cotunnite structures; we also show, using a dashed line Fig. 4.5, the calculated bandgap for the $P\bar{6}2m$-CaF_2 phase, which begins to slowly decrease above 50 GPa. Semilocal DFT calculations using GGA functionals have also shown that this occurs for γ-CaF_2 above 70 GPa [161]. The optical bandgap for γ-CaF_2 lies 0.9−1.2 eV above that of $P\bar{6}2m$-CaF_2 in the pressure range 10−70 GPa, suggesting that the formation of $P\bar{6}2m$-CaF_2 might be detectable in optical measurements. We remark here that the $P\bar{6}2m$ phase is only predicted to be stable at high temperature, and that our calculated bandgaps in Fig. 4.5 have not been corrected for the effects of temperature.

Low temperature CaF_2 has been proposed as an internal pressure standard [143]. Our calculations of the bandgap shows that it remains a wide-gap insulator up to at least 70 GPa, and likely retains its superior optical properties up until high pressures.

4.6 Conclusions

We have explored Be-, Mg- and CaF_2 at pressures up to 70 GPa through DFT calculations and computational structure searching.

BeF_2 has a large number of polymorphs at ambient pressures, and shares many of these with SiO_2, such as α, β-quartz and α, β-cristobalite. We identify BeF_2 as a potential tetrahedral framework material. Our searches show that BeF_2 has open-framework zeolite-like polymorphs, and that framework structures predicted in BeF_2 are energetically relevant to SiO_2, highlighting the utility of structure searching in model systems. At higher pressures, we find that BeF_2 is stable in the moganite structure between 11.6 and 30.1 GPa, and stable in the $CaCl_2$ structure between 30.1 and 57.5 GPa.

In MgF_2, we find that the *Pbca*-symmetry 'O-I' TiO_2 structure is a stable intermediary between the pyrite and cotunnite MgF_2 phases, and is the lowest enthalpy MgF_2 structure between 39.6 and 44.1 GPa. A class of polymorphs for SiO_2 intermediate to the $CaCl_2$ and α-PbO_2 structures, which are relevant at Earth mantle pressures and are close to stability near 100 GPa in SiO_2, also occur in MgF_2 but at much lower pressures (≈ 10 GPa).

We find that the Fe_2P-type $P\bar{6}2m$-symmetry structure for CaF_2 lies close in enthalpy to the known γ-CaF_2 phase over the pressure range 0−70 GPa. Calculations using the QHA show that this structure is stabilised at high pressure and temperature ($P \gtrsim 10$ GPa and $T \gtrsim 1500$ K). The $P\bar{6}2m$ structure develops unstable phonon modes at high temperatures, which we propose is associated with a superionic transition in this structure. Classical molecular dynamics simulations show that a superionic transition does occur in this structure, accompanied by a structural rearrangement of the calcium ion sublattice.

Be-, Mg- and CaF_2 are wide-gap insulators. Calculations using the HSE06 functional show that the bandgaps in BeF_2 and MgF_2 are tunable with pressure, rising by 0.06 eV/GPa and 0.04 GPa over the pressure range 0−70 GPa. The optical bandgaps in CaF_2 are instead relatively constant over this pressure range.

Chapter 5

A hydride superconductor: stable high pressure hydrogen sulfide

Superconductivity is an exotic physical phenomenon characterised by the electrical resistance of a material decreasing abruptly to zero, usually at very low temperature. In this chapter, we explore stable phases of highly compressed hydrogen sulfide, as found using structure searching methods. High pressure hydrogen sulfide has recently been found to be a high-temperature superconductor in diamond anvil cell experiments, and characterising stable hydrogen−sulfur compounds at different pressures is key in understanding the observed superconductivity. Parts of this chapter contributed to the work published in:

Y. Li, L. Wang, H. Liu, Y. Zhang, J. Hao, C. J. Pickard, J. R. Nelson, R. J. Needs, W. Li, Y. Huang, I. Errea, M. Calandra, F. Mauri, and Y. Ma
Dissociation products and structures of solid H_2S at strong compression
Physical Review B **93**, 020103(R) (2016),

which is also reference [114] of this thesis. This work was a combined theoretical-experimental study of the H-S system, and my contribution to this was to carry out structure searches using the AIRSS technique. The bulk of this chapter therefore details the results of these structure searches.

5.1 Introduction

Developments in low-temperature experimental physics, such as the successful liquefaction of helium in 1908, paved the way for the first observation of superconductivity in 1911 by Dutch physicist Heike Kamerlingh Onnes. An entry in his laboratory notebook dated 8 April 1911 contains the brief comment *Kwik nagenoeg nul*, meaning 'Mercury['s resistance] practically zero.', a message which ushered in a new era of

physics [162]. Kamerlingh Onnes had observed an abrupt decrease in the measured resistance of mercury near 4.2 K; these discoveries would see him awarded the 1913 Nobel Prize in Physics. The temperature at which resistance abruptly decreases in this manner is referred to as the superconducting critical temperature, T_c.

Superconductivity was subsequently observed in a number of other materials and attempts were made to further characterise the superconducting state. In 1933, Fritz Walther Meissner and Robert Ochsenfeld discovered that a superconductor will exclude any external magnetic fields: this is now known as the *Meissner effect*. This phenomenon is responsible for many of the applications of superconducting materials in magnetic levitation.

A key theoretical development in the superconductivity field was *BCS theory*, advanced in 1957 by John Bardeen, Leon Cooper and John Schrieffer [163, 164]. BCS theory describes the superconducting state as the result of the formation of so-called Cooper pairs of electrons which are weakly bound at low temperature. The 'binding force' for these pairs is ascribed to interactions between electrons and phonons in the material. A further key ingredient is the formation of a small energy gap which suppresses excitations in electron quantum states. BCS theory creates an important division in superconducting materials: the synonyms *conventional* or *phonon-mediated* are used to describe materials which conform to the (original) BCS theory, while *unconventional* superconductors are those that do not. Prior to the experimental discoveries outlined in the subsequent sections of this chapter, the conventional superconductor with the highest known T_c was magnesium diboride, MgB_2, which has $T_c = 39$ K [165], discovered in 2001. Superconductivity with T_c in the neighbourhood of 140 K has been observed in unconventional superconductors, such as the well known cuprates, which can be broadly described as transition metal oxides.

5.2 Superconducting hydrides

Since the discovery of superconductivity, the hunt has been on for a room temperature superconductor, considered one of the 'holy grails' of condensed matter physics. How do we get to high T_c superconductors? BCS theory provides a concrete path: candidate materials ideally have high-frequency phonons and a high electronic density of states at the Fermi level. N. Ashcroft made two significant suggestions for such materials. The first was to propose elemental hydrogen as a high T_c superconductor, on the grounds that the low atomic mass in hydrogen leads to a large Debye temperature, and therefore in principle to a large T_c [166]. This particular route offers challenges in that large pressures or temperatures are needed to successfully metallize elemental hydrogen, the pursuit of which is a large and thriving research area in its own right. At the time of writing, experiments have successfully statically compressed hydrogen to at least 400 GPa, where a 'Phase V' for H has been observed and described as a

possible precursor to metallic hydrogen [167], while recent QMC calculations put the metallization pressure in the range 421-473 GPa [168]. Lastly, Dias and Silvera have very recently published experimental results concerning metallic hydrogen observed at 495 GPa in diamond anvil cells [169], which has generated intense debate [170].

Subsequent to Ref. [166], Ashcroft also suggested alloying hydrogen with other atoms to create superconducting hydrides, which are expected to metallize at much lower pressures than elemental hydrogen due to 'chemical precompression' [171]. This idea has subsequently proved to be a rich ground for structural prediction methodologies such as those discussed in Chapter 3. These methods allow the structures of hypothetical hydrides to be determined (particularly at high pressures), and *ab initio* methods (to be discussed in Sec. 5.6) are available for determining the critical temperature of materials within BCS theory. As such, a number of predictions stemming from structure prediction calculations are now available. We summarise some example systems, methodologies and calculated critical temperatures in Table 5.1. All electronic structure calculations in these systems have been performed with DFT.

Hyd.	SG	E_{xc}	Searching	Pred. T_c	λ	P	Ref.
SnH_4	$P6_3/mmc$	PBE	Evolutionary	52-62 K	0.87	200 GPa	[172]
PH_2	$I4/mmm$	PBE	Evolutionary	48-70 K	1.13	200 GPa	[85]
H_4Te	$P6/mmm$	PBE	Swarm	73-104 K	1.46	170 GPa	[173]
YH_4	$I4/mmm$	PBE	Swarm	84-95 K	1.01	120 GPa	[174]
SbH_4	$P6_3/mmc$	PBE	Random + Swarm	94 K	1.16	300 GPa	[175]
H_3Se	$Im\bar{3}m$	LDA	Minima hopping	131 K	1.45	200 GPa	[176]
Si_2H_6	$Pm\bar{3}m$	PBE	Random	139-153 K	1.40	275 GPa	[177]
AsH_8	$C2/c$	PBE	Random + Swarm	151 K	1.77	450 GPa	[175]
H_3S	$Im\bar{3}m$	PBE	Evolutionary	191-204 K	2.19	200 GPa	[178]
CaH_6	$Im\bar{3}m$	PBE	Swarm	220-235 K	2.69	150 GPa	[179]
YH_6	$Im\bar{3}m$	PBE	Swarm	251-264 K	2.93	120 GPa	[174]
H_2	$I4_1/amd$	PBE	–	300 K	1.63	500 GPa	[180]

Table 5.1: Table showing a variety of predicted superconducting hydrides. We show the hydride (Hyd.), space group of the structure (SG), and the searching technique used to predict it. All the above examples used DFT, and we show the exchange-correlation functional E_{xc}, predicted critical temperature, electron-phonon coupling strength λ (see Sec. 5.6), and the pressure P at which the prediction was made. The H_2 entry of the table used a previously predicted atomic hydrogen structure for calculations of T_c; see Ref. [180] for details.

5.3 Hydrogen sulfide

The structure prediction study of Li *et al.* [181] examined hydrogen sulfide, H_2S, as a potential superconducting hydride and reported a predicted T_c in the vicinity of 80 K for this compound at 160 GPa. Shortly after this, Duan *et al.* [178] carried out structure searching calculations on H_3S, and found an even higher predicted T_c of $\approx$200 K at 200 GPa (see Table 5.1).

Following these studies, Drozdov *et al.* reported the results of compressing H_2S to $P \lesssim 230$ GPa using diamond anvil cells.[1] Their experiments used direct electrical measurements to determine the resistance of the compressed H_2S sample. At pressures above 100 GPa, sudden decreases in the measured resistance were observed at low temperatures. These decreases moved to progressively higher temperatures with increasing pressure, and a maximum T_c of 150 K for pressures $\gtrsim 150$ GPa was observed: a new high temperature superconductor had been found (Fig. 5.1). The superconducting behaviour observed was found to be PT-path dependent – for H_2S samples prepared and compressed at low temperature, a steady increase in T_c was seen with increasing pressure, rising to $T_c = 150$ K at 200 GPa, while samples that were annealed to about 300 K instead saw a higher and weakly pressure-dependent T_c of around 190 K. Measurements of the magnetization of H_2S samples eventually established the highest T_c recorded in this system as 203±1 K, at 155 GPa [182]. The recent experiments of Troyan *et al.* have succeeded in observing the Meissner effect in compressed H_2S at 153 GPa [183].

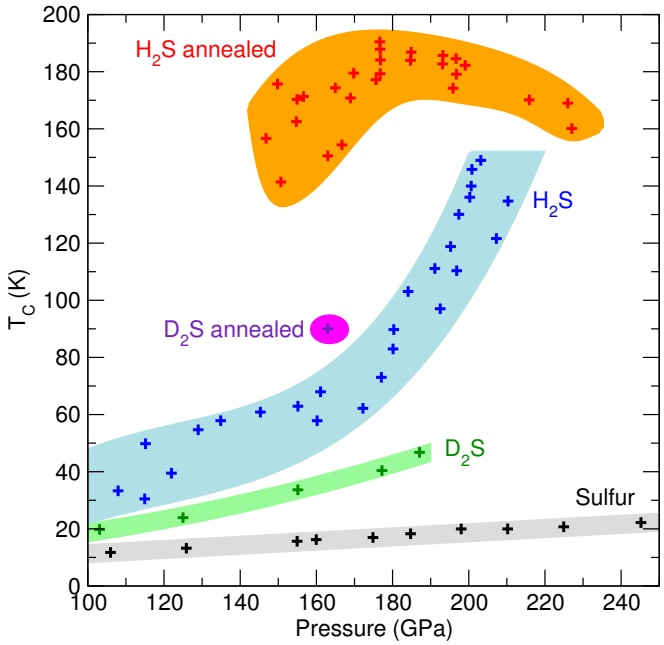

Figure 5.1: Measurements of the superconducting critical temperature in hydrogen sulfide, determined by electrical resistance, against pressure as recorded by Drozdov *et al.* Blue data points correspond to H_2S samples prepared at low temperature, and an abrupt rise in T_c is found between about 160 and 200 GPa. Red data points correspond to H_2S samples which are first annealed by warming to 220-300 K; for these samples, a much higher T_c is found ('H_2S annealed'). Corresponding measurements for deuterium sulfide are shown in green and purple. For comparison, measurements were also taken of T_c in elemental sulfur (black points). Figure adapted from Figs. 2a) and b) of Drozdov *et al.*, arxiv:1412.0460. Additional data and measurements can be found in Ref. [182].

[1] The original results, which we show in Fig. 5.1, appeared as arxiv:1412.0460 on 1 Dec 2014; a revised version was submitted as arxiv:1506.08190 on 26 Jun 2015, and the work was eventually published as Ref. [182].

Given the agreement between the experimentally observed T_c and that predicted for H_3S by Duan *et al.* [178], it was proposed that H_2S undergoes a pressure-induced decomposition where H_3S is formed alongside other sulfur-rich decomposition products, and that H_3S is responsible for the observed superconductivity. At 200 GPa, H_3S takes on a symmetric cubic structure (space group $Im\bar{3}m$), and it is worth noting that a pressure-induced decomposition of H_2O (a sister molecule to H_2S) into H_3O in the same $Im\bar{3}m$ structure has previously been predicted, but at much higher pressures of several terapascals (TPa) [184]. The subsequent first-principles studies of Duan *et al.* and Bernstein *et al.* looked at different stoichiometries H_nS and concluded that at above 43 GPa, H_2S is indeed unstable by decomposition into H_3S and S [185, 186]. Note that the experimental results of Drozdov *et al.* (see Fig. 5.1) affirm that S alone is not responsible for the observed high T_c.

The goal of this chapter is to apply structure searching techniques to the hydrogen-sulfur system, and to establish stable stoichiometries formed at different pressures. The crystal structures of these compounds allow an understanding of the lead-up to the superconducting state seen in H_2S, and the superconducting state itself.

5.4 Methods

Electronic structure calculations are carried out with the CASTEP plane−wave pseudopotential DFT code (Sec. 2.8.1), using Vanderbilt-type ultrasoft pseudopotentials (Sec. 2.9.5) for H and S as generated internally by the CASTEP code. We use the Perdew−Burke−Ernzerhof (PBE) exchange−correlation functional (Sec. 2.5.2). A plane−wave cutoff of 750 eV, Monkhorst-Pack Brillouin zone sampling density of at least $2\pi \times 0.03$ Å^{-1} (Sec. 2.8.3), grid scale of 2 (for the density) and fine grid scale of 2.3 are used in these calculations.

We apply the AIRSS method of Section 3.3 at pressures of 25, 50, 100, 150 and 200 GPa, searching over a total of 44 different H_nS_m stoichiometries. The convex hull method, discussed in Section 4.3.1, is then used to find stable stoichiometries. The structure searching calculations were carried out independently and alongside other researchers who applied the CALYPSO search technique discussed in Section 3.7; one can refer to Ref. [114] for details of the particle-swarm calculations. The results of both methods were then compiled in order to give the results published in [114]. We report in what follows the results of AIRSS searches, but remark that in the majority of cases the AIRSS and CALYPSO methods were in agreement as to the stable structures and compositions.

5.5 Results

The results of our structural searches are essentially summarised in Fig. 5.2. We calculate the H-S convex hull at different pressures in the range 25-200 GPa, and determine which compounds are stable (i.e., lie on the convex hull). The coloured bars in Fig. 5.2 show the pressure ranges over which various H_nS_m compounds are stable, and we indicate the space group of the corresponding stable structure. The calculations in Fig. 5.2 do not include the effects of zero-point motion. In addition to Fig. 5.2, we also show convex hulls for the H-S system at four different pressures in Fig. 5.3.

The structures depicted in Fig. 5.2 were found using the AIRSS method, with the exception of the $C2/m$-H_3S_5 structure, which is from the work of Goncharov *et al.* [187]. We also note that the $R3m$ and $Im\bar{3}m$ structures for H_3S have been reported previously by Duan *et al.* [178].

In the following sections, we examine some of the H_nS_m phases found here in more detail. Unless otherwise indicated, our discussion quotes pressures of phase transitions as calculated at the static-lattice level.

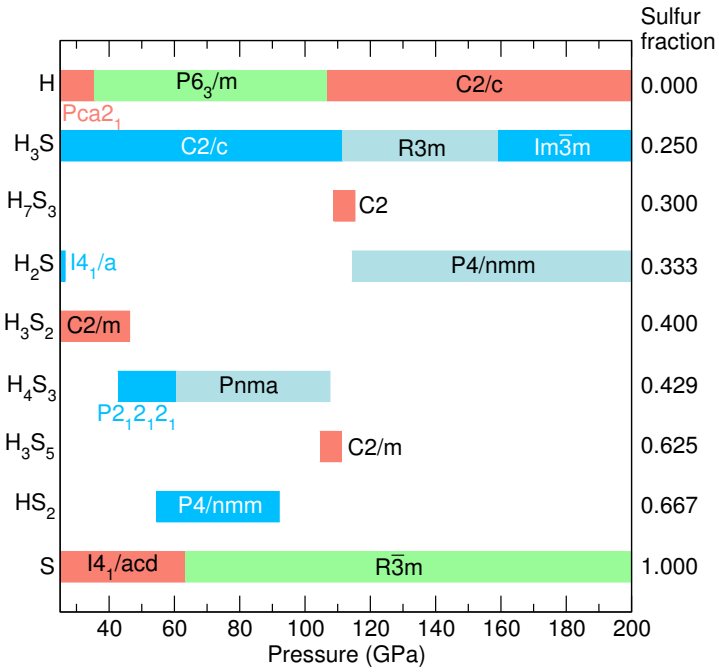

Figure 5.2: Composition diagram for the H-S system over the pressures 25-200 GPa, as calculated at the static-lattice level of theory. Coloured bars are used to show the space groups of stable phases and the pressure ranges at which they are stable. The H_3S_5 structure is from Ref. [187]. The vertical axis, which shows the sulfur fraction, is not to scale.

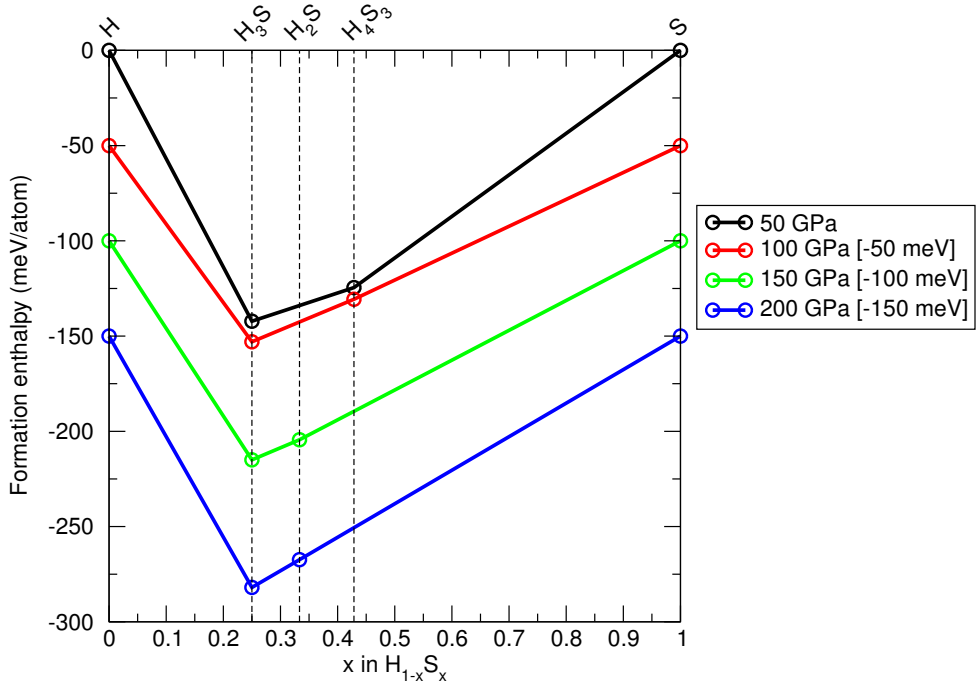

Figure 5.3: Convex hulls for the H-S system at 50, 100, 150 and 200 GPa. For ease of viewing, the hulls are offset by the amounts indicated in the figure legend.

5.5.1 Elemental H and S

We carry out structure searching for solid H and S over the pressure range 25-200 GPa, though it is worth noting that extensive searches and experimental studies have already been carried out for these elements at the pressures relevant here.

For hydrogen, in addition to our searches, we also examine the structures obtained by Pickard and Needs [188]. We do not find any additional H structures that not already discussed in Ref. [188], and calculate the sequence of transitions:

$$Pca2_1 \xrightarrow{36\ \text{GPa}} P6_3/m \xrightarrow{107\ \text{GPa}} C2/c\,; \tag{5.1}$$

see also Fig. 5.2.

High-pressure experimental studies on sulfur show a transition from S-I (space group $Fddd$) to S-II (space group $P3_221$) at low pressure (< 5 GPa). S-II then undergoes a transition to a $I4_1/acd$ phase (S-III) [189] near 35 GPa, with a further transition between 83-94 GPa to an incommensurately modulated monoclinic structure (S-IV). The average unit cell has two S atoms and a monoclinic angle $\beta \approx 113°$ at 100 GPa; the incommensurate modulation is along the crystallographic b-axis. Around 95 GPa, sulfur becomes metallic [190]. Above 153 GPa, a transition to an $R\bar{3}m$ structure (β-Po, S-V) occurs [191]. We do not treat the incommensurate sulfur phase (IV) in our

calculations, and instead have sulfur in the phases:

$$I4_1/acd \text{ (S-III)} \xrightarrow{63 \text{ GPa}} R\bar{3}m \text{ (S-V)} \tag{5.2}$$

over the range 25-200 GPa.

5.5.2 H_3S

Our searches find the following sequence of phase transitions for H_3S (see Fig. 5.2):

$$C2/c \xrightarrow{111 \text{ GPa}} R3m \xrightarrow{159 \text{ GPa}} Im\bar{3}m, \tag{5.3}$$

and hence we affirm the work of Duan *et al.* [178] in the sense that the $R3m$ and $Im\bar{3}m$ H_3S phases are those that tend to be stable at the pressures at which superconductivity is seen (Fig. 5.1). However, the $C2/c$ structure here is a new prediction, and at the static-lattice level is more stable than the $Cccm$-H_3S structure given in Ref. [178]. The $C2/c$ phase is comprised of H_2 and H_2S molecules, and we show it alongside the $Cccm$ phase in Fig. 5.4.

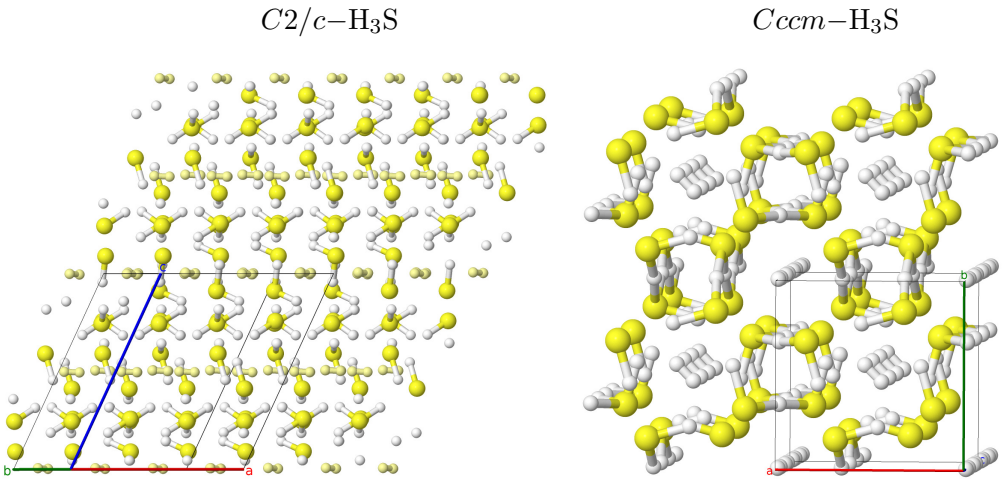

Figure 5.4: 2×2×2 slabs of low pressure H_3S structures. (*Left*) The $C2/c$ structure predicted to be stable below 111 GPa. This phase consists of distinct H_2S and H_2 molecules. Sulfur atoms in yellow, hydrogen atoms in white, and H_2 molecules in pale yellow. (*Right*) The $Cccm$ structure predicted in Ref. [178]. H_2S molecules form an extended network, which have interstitial H_2 molecules.

The $R3m$ structure can be viewed as a lower-symmetry distortion of the cubic $Im\bar{3}m$ phase, where hydrogen atoms move away from the exact midpoint between sulfur atoms. We depict these two structures in Fig. 5.5. Goncharov *et al.* [187] have additionally proposed distortions of the $Im\bar{3}m$ phase resulting in H_3S structures with Cm and $I4mm$ symmetry. We do not find either of these phases to be lower in enthalpy than $R3m$ or $Im\bar{3}m$-H_3S: the Cm structure relaxes to $R3m$ in our calculations, and the $I4mm$ structure is intermediate to $R3m$ and $Im\bar{3}m$. We would also comment that a very dense k-point sampling is needed to fully resolve the enthalpy differences between

these metallic phases. The enthalpy differences are also small - for example, above about 135 GPa, the $R3m$ and $Im\bar{3}m$ phases are within 10 meV/H_3S of one another.

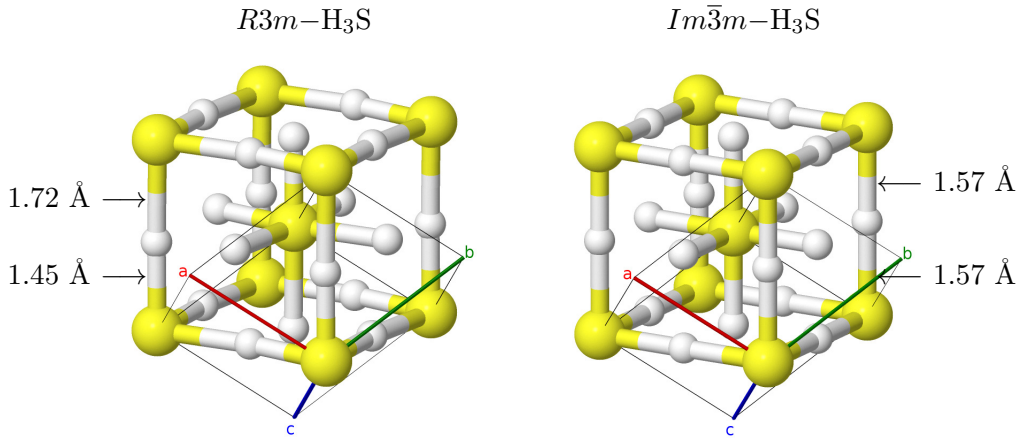

Figure 5.5: High pressure H_3S phases. (*Left*) $R3m$ phase, stable between 111 and 159 GPa. (*Right*) $Im\bar{3}m$ phase stable above 159 GPa. Both structures have a similar bcc sulfur sublattice. The higher symmetry $Im\bar{3}m$ has hydrogen atoms collinear with, and equidistant from, the sulfur atoms, while the lower symmetry $R3m$ structure sees hydrogen atoms move away from these 'midway' sites. The lengths shown are H−S bond lengths as calculated for these structures at 110 GPa. Nuclear motion favours the $Im\bar{3}m$ structure and lowers the $R3m$-$Im\bar{3}m$ transition pressure [192].

The static-lattice calculations here are not completely sufficient to determine the phase transition pressures (Eq. (5.3)) in H_3S to a high level of accuracy. Errea *et al.* [192] have shown that including anharmonic nuclear vibrational effects lowers the $R3m$-$Im\bar{3}m$ transition pressure to 103 GPa, a decrease of more than 35% on the static-lattice value of 159 GPa in Eq. (5.3). It is also noteworthy that in terms of nuclear vibrations the $R3m$-$Im\bar{3}m$ transition cannot be treated in the harmonic phonon approximation (Sec. 2.7.1), because the $R3m$ structure has unstable phonon modes at the harmonic level for pressures below the static-lattice $R3m$-$Im\bar{3}m$ transition pressure [192]. Techniques for treating anharmonicity, such as those discussed in Sec. 2.7.3, are necessary. Anharmonic effects also strongly impact other properties, such as the calculated electron-phonon coupling strength [193].

On the experimental side, the $Cccm$, $R3m$ and $Im\bar{3}m$ H_3S phases have essentially been reported based on XRD data, but there is some disagreement as to the exact transition pressures between these. Einaga *et al.* report XRD patterns at 150 GPa, showing the presence of a bcc sulfur lattice corresponding to $R3m$ or $Im\bar{3}m$ H_3S, as well as the presence of β-Po sulfur (Section 5.5.1) [194]. Goncharov *et al.* report the $Cccm$ phase between roughly 55 and 110 GPa, with H_2S as the starting material. The $R3m$ and/or $Im\bar{3}m$ H_3S phases were detected above 110 GPa [187]. The similarity between the $R3m$ and $Im\bar{3}m$ phases means that they are difficult to distinguish in XRD data. Guigue *et al.* have synthesised H_3S directly from elemental H and S at high pressure, and instead report an extended stability field for the $Cccm$-H_3S phase,

finding that it forms up to at least 160 GPa [195]. Further experiments by Goncharov *et al.* also synthesised H_3S directly from the elements, but instead showed that the $Im\bar{3}m$ phase is stable down to 140 GPa, where it transforms to the $R3m$ phase, which (upon annealing) further transforms to $Cccm$-H_3S at 70 GPa [196]. These results also show that the exact PT path taken is important in determining the structures found, as well as their crystallinity. Finally, we remark that the experiments of Li *et al.* [114] have observed XRD patterns consistent with $C2/c$-H_3S, but in a mixture with other compounds. We discuss this last point in more detail in Section 5.7.

5.5.3 H_7S_3

As can be seen in Fig. 5.2, an H_7S_3 structure with space group $C2$ is predicted to have a narrow range of stability, between 109 and 115 GPa. The structure is metallic within this pressure window, and is depicted in Fig. 5.6. It has Z=2, which is to say 14 atoms, in the primitive unit cell.

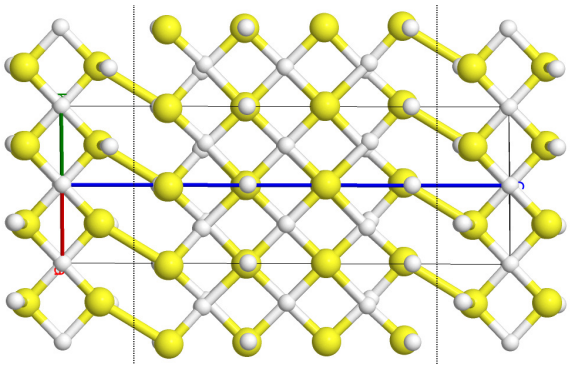

Figure 5.6: H_7S_3 with $C2$ symmetry. Sulfur atoms in yellow, hydrogen atoms in white.

The structure can be viewed as layers of slabs cut from the cubic $Im\bar{3}m$ structure in Fig. 5.5. In Fig. 5.6, two vertical dotted lines are used to indicate the extent and boundaries of such a slab.

Slab, or layer-like structures, may have an important role in explaining the onset of superconductivity in H_2S. Akashi *et al.* [197] have proposed an infinite series of metastable hydrogen sulfide structures with sulfur fractions intermediate to H_2S and H_3S (i.e., between 0.250 and 0.333). These are comprised of layers of varying thicknesses constructed from solid H_2S and H_3S structures, and are analogous to Magnéli phases formed in a number of transition metal oxides. Although these phases are metastable, calculations of T_c in the corresponding structures match the rapid rise in T_c seen in the blue shaded region of Fig. 5.1 between about 160 and 210 GPa. Examining Ref. [197] closely, it is possible that the H_7S_3 structure shown in Fig. 5.6 could be classified as '$\alpha\alpha\beta\beta$' (using the nomenclature of that reference), but we have not fully investigated this.

Finally we remark that the work of Ishikawa *et al.* [198] predicts a $P1$-symmetry H_5S_2

structure to be stable between 110 and 123 GPa. This structure is composed of H_2S and H_3S units, and calculations of its superconducting critical temperature show reasonable agreement with experimental results (Fig. 5.1). However, at the static lattice level, our calculations show that the $C2$-H_7S_3 structure presented here precludes the stability of $P1$-H_5S_2.

5.5.4 H_2S

As can be seen in Fig. 5.2, H_2S is an unstable stoichiometry above 26 GPa. The work of Li *et al.* [181] provides a set of (metastable) H_2S structures at pressures above this; these include $P\bar{1}$ and $Cmca$ symmetry H_2S structures which were used in the work of Akashi *et al.* mentioned in Section 5.5.3. Our searches have also found a couple of structurally similar phases with $C2/c$ and $C2/m$ symmetries, that are energetically in the same neighbourhood as $P\bar{1}$ and $Cmca$ structures.

Above 114 GPa, we have also found a layered H_2S structure with $P4/nmm$ symmetry and Z=6, which consists of alternating sulfur and H_3S layers (Fig. 5.7). At the static lattice level, this structure is stable between 114 and 201 GPa, and is metallic over this pressure range.

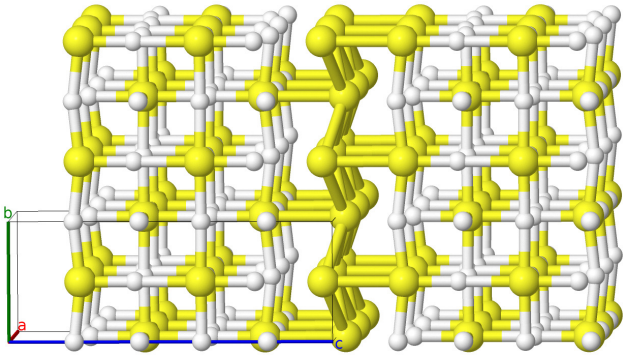

Figure 5.7: Layered H_2S structure, consisting of slab regions of $Im\bar{3}m$-like H_3S separated by buckled sheets of sulfur. Hydrogen atoms in white, sulfur atoms in yellow.

The work of Gordon *et al.* [199] has also proposed a perovskite-like H_2S structure. The authors calculated that $Im\bar{3}m$-H_3S would be unstable by decomposition into perovskite H_2S and elemental H_2, thus challenging the notion that $Im\bar{3}m$-H_3S plays an important role in the observed superconductivity. We do not find these proposed perovskite structures to be stable, but do note that they turned up as metastable phases during our structure searches. The authors of [199] have released a corrigendum concerning their energy calculations.

5.5.5 H_3S_2

Fig. 5.2 shows that H_3S_2 is a stable compound up to 46 GPa. The corresponding structure has $C2/m$ symmetry and Z=4 in the primitive unit cell, and is depicted in

Fig. 5.8. It can be considered to be built from H_2S, H_3S and HS_2 molecules.

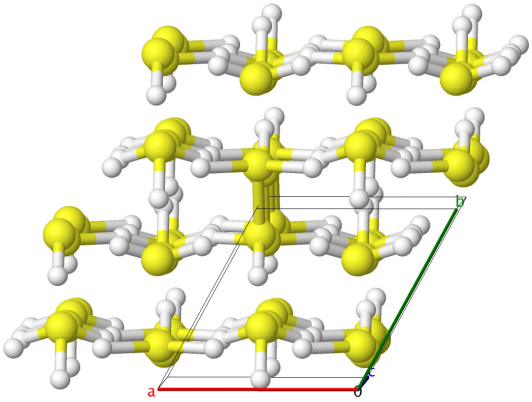

Figure 5.8: Illustration of the $C2/m$ H_3S_2 structure, viewed almost down the crystallographic c-axis.

H_3S_2 is semiconducting in this structure, and the PBE bandgap decreases from approximately 1.1 eV to 0.6 eV over the pressure range 25-46 GPa.

5.5.6 H_4S_3

We find H_4S_3 to be a stable stoichiometry between 43 and 108 GPa. Two structures, with $P2_12_12_1$ and $Pnma$ symmetry and both with Z=4, are found in this pressure range with a transition between the two:

$$P2_12_12_1 \xrightarrow{61\text{ GPa}} Pnma. \tag{5.4}$$

This transition occurs in a continuous manner, in the sense that the calculated enthalpy-pressure curves for the $P2_12_12_1$ and $Pnma$ phases merge (rather than cross) at 61 GPa. We show the $P2_12_12_1$ structure in Fig. 5.9; the $Pnma$ structure is quite similar.

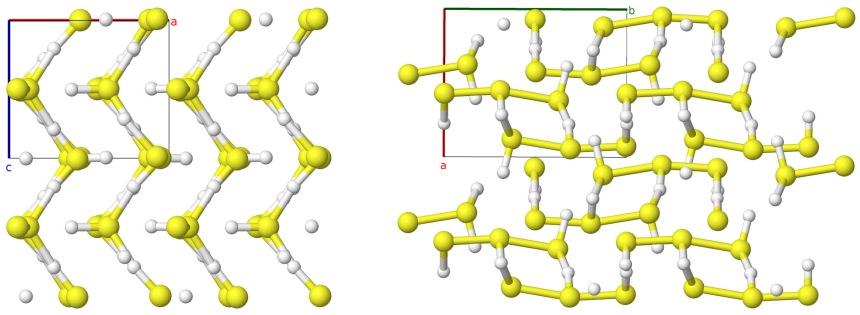

Figure 5.9: Two views of the $P2_12_12_1$-H_4S_3 structure, stable between 43 and 61 GPa. (*Left*) view down the b-axis, and (*Right*) view down the c-axis. Sulfur atoms (yellow) form buckled chains running along the b-axis; each sulfur is bound to either one or two hydrogen atoms (shown in white), and longer H-S bonds connect neighbouring sulfur chains.

Li *et al.* [114] calculate the band gap of the $Pnma$ phase, and find a metallisation

pressure of 73 GPa with the PBE functional, and 102 GPa with the HSE06 functional.

Goncharov *et al.* [187] also propose a $P\bar{1}$-symmetry H_4S_3 structure. Our calculations find that this structure is more energetically favourable than the $P2_12_12_1$ structure discussed here below about 23 GPa; however, this falls outside the stability range for H_4S_3.

5.5.7 HS_2

Our searches find an HS_2 compound, space group $P4/nmm$, to be stable between 54 and 92 GPa (Fig. 5.2). We show this structure in Fig. 5.10.

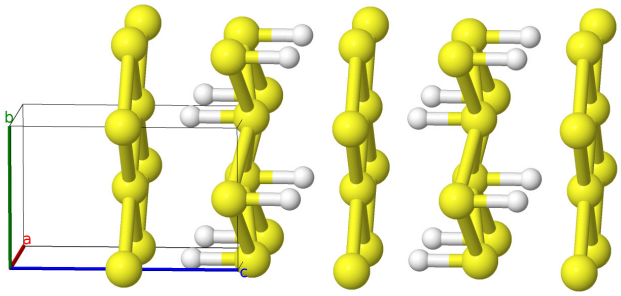

Figure 5.10: The $P4/nmm$-symmetry HS_2 structure. The phase consists of flat sheets of sulfur atoms, bonded in squares, and buckled sheets of sulfur atoms, each bonded to one hydrogen atom. Sulfur atoms in yellow, hydrogen atoms in white.

As was the case in H_3S, vibrational motion also affects the window of stability of HS_2. Li *et al.* [114] have shown that the effect of zero-point motion, treated at the harmonic level, narrows the stability field of $P4/nmm$-HS_2 to between 75 and 87 GPa.

Goncharov *et al.* [187] have proposed a structurally similar $Pmmn$ structure for HS_2. However, our calculations find that this structure relaxes to the $P4/nmm$ phase proposed here. Dense k-point sampling is again required due to the metallicity of these structures.

5.6 An outline of ab initio T_c calculations

By now, we have discussed a number of H_nS_m phases which have stemmed from our structure searches. These candidate structures can be used to generate XRD patterns in an effort to match experimental data now (increasingly) available for the H-S system. However, a key test for proposed structures and their stability is whether they yield a T_c that matches available data (e.g., Fig. 5.1). In this section we discuss techniques for calculating T_c from first-principles. The methods mentioned here are presented only in the context of conventional (phonon-mediated) superconductivity. A recent and extensive review of first-principles electron-phonon calculations can be found in Giustino [37], which is our primary reference for this section.

A key first step is calculating the set of electron-phonon matrix elements, $g_{mn\nu}$, defined by:

$$g_{mn\nu}(\mathbf{k},\mathbf{q}) = \frac{1}{\sqrt{2\omega_\nu(\mathbf{q})}}\langle\phi_{m\mathbf{k}+\mathbf{q}}|\Delta_{\mathbf{q}\nu}V_{KS}|\phi_{n\mathbf{k}}\rangle. \tag{5.5}$$

These matrix elements are taken between Kohn-Sham orbitals $\phi_{n\mathbf{k}}$ and $\phi_{m\mathbf{k}+\mathbf{q}}$. The orbitals are labelled by band number (n and m) and Brillouin-zone points ($\mathbf{k}$, and $\mathbf{k}$+$\mathbf{q}$). The quantity $\Delta_{\mathbf{q}\nu}V_{KS}$ is the derivative of the self-consistent Kohn-Sham potential V_{KS} with respect to the phonon mode having branch index ν, and wavevector $\mathbf{q}$ – see Eq. (2.53) and the discussion following it. The underlying physics of Eq. (5.5) is then clear: it describes the scattering between electronic states $\phi_{n\mathbf{k}}$ and $\phi_{m\mathbf{k}+\mathbf{q}}$, induced by the phonon $\nu\mathbf{q}$. In Eq. (2.50), we saw that a phonon mode ($\nu\mathbf{q}$) corresponds to a displacement of atoms $\Delta r_{(p\alpha)i}$ with amplitude $A_{\alpha i}(\mathbf{q})$ and frequency ω and so $\Delta_{\mathbf{q}\nu}V_{KS}$ can be expressed as (with $A_{\alpha i}(\mathbf{q}) \to A_{\alpha i\nu}(\mathbf{q})$ and $\omega \to \omega_\nu(\mathbf{q})$):

$$\Delta_{\mathbf{q}\nu}V_{KS} = \sum_{\alpha i}\frac{A_{\alpha i\nu}(\mathbf{q})}{\sqrt{M_\alpha}}\sum_p e^{i\mathbf{q}.\mathbf{r}_p}\frac{\partial V_{KS}}{\partial r_{(p\alpha)i}}, \tag{5.6}$$

i.e., as a sum of derivatives of V_{KS} with respect to the position of nucleus α in cell p along Cartesian direction i. These quantities can in turn be evaluated either using supercells, or DFPT (Section 2.7.4).

Next, the isotropic Eliashberg function $\alpha^2F(\omega)$ is calculated from these electron-phonon matrix elements using:

$$\alpha^2F(\omega) = \frac{1}{N_F}\int\frac{d\mathbf{k}d\mathbf{q}}{\Omega_{BZ}^2}\sum_{mn\nu}|g_{mn\nu}(\mathbf{k},\mathbf{q})|^2\delta(\epsilon_{n\mathbf{k}}-\epsilon_F)\delta(\epsilon_{m\mathbf{k}+\mathbf{q}}-\epsilon_F)\delta(\omega-\omega_{\mathbf{q}\nu}), \tag{5.7}$$

where N_F is the density of states at the Fermi level, and ϵ_F is the Fermi energy. The delta functions in Eq. (5.7) therefore constrain energies to be near the Fermi energy. As we have seen a couple of times by now, the integrals over $\mathbf{k}$ and $\mathbf{q}$ in Eq. (5.7) are in practice carried out using sums involving grids of k and q-points. The delta functions are also broadened for calculation purposes, for example using Lorentzian [200] or Gaussian functions [201].

Giustino *et al.* [200] have shown that in general, extremely dense k-point sampling is needed to achieve convergence when evaluating Eq. (5.7). This implies the calculation of a large number of matrix elements $g_{mn\nu}(\mathbf{k},\mathbf{q})$, which in turn implies a large number of phonon frequency calculations (in order to compute $\Delta_{\mathbf{q}\nu}V_{KS}$); the resulting calculation is then prohibitively expensive. The authors of Ref. [200] introduce a Wannier interpolation scheme, whereby the matrix elements $g_{mn\nu}(\mathbf{k},\mathbf{q})$ are instead first calculated on a relatively coarse Brillouin zone grid, and then interpolated (at low computational cost) onto a much denser grid.

Two further quantities: λ, the strength of electron-phonon coupling, and $\omega_{\log}$, the log-

arithmic average of phonon frequencies, can then be calculated through the relations:

$$\lambda = 2\int_0^\infty \frac{\alpha^2 F(\omega)}{\omega} d\omega, \quad \omega_{\log} = \exp\left(\frac{2}{\lambda}\int_0^\infty \frac{\alpha^2 F(\omega)}{\omega}\log(\omega) d\omega\right). \tag{5.8}$$

We met λ earlier in Table 5.1, where its calculated values are given for a number of hydride materials.

There are now a few options for calculating the critical temperature T_c itself. We can solve the so-called Migdal-Eliashberg gap equations, which are a coupled set of non-linear equations involving the renormalization function $Z_{n\mathbf{k}}$, and superconducting gap function $\Delta_{n\mathbf{q}}$. See, for example, Eqs. (208) and (209) of Giustino [37] for a statement of these gap equations. These require as input the temperature T, a slight generalisation of the electron-phonon coupling strength λ of Eq. (5.8), and μ^* (to be discussed shortly). The temperature at which the gap function $\Delta_{n\mathbf{q}}$ goes to zero is then the superconducting critical temperature T_c.

Approximate solutions to the gap equations are also available, and give another widely-used method for obtaining T_c. An example is the Allen and Dynes modified McMillan equation [202]:

$$k_B T_c = \frac{\omega_{\log}}{1.2}\exp\left[-\frac{1.04(1+\lambda)}{\lambda - \mu^*(1+0.62\lambda)}\right], \tag{5.9}$$

which determines T_c directly from the quantities given in Eq. (5.8).

The quantity μ^* appearing here, and in the gap equations, is a dimensionless 'effective' Coulomb potential, also referred to as the strength of the Morel-Anderson pseudopotential [203]. It is in principle possible to calculate μ^*, which involves averaging the matrix elements of the screened Coulomb interaction over the Fermi surface, and an example can be found in Ref. [204] where it is calculated for calcium-intercalated graphene. In practice (and in a slightly non-*ab initio* manner), μ^* is not explicitly calculated but instead taken to lie in an expected range of 0.1-0.2 [37]. A calculation of T_c therefore does not result in a unique value, but rather a range of values depending on the value of μ^*. It is for this reason that many of the T_c values reported in Table 5.1 are given as a range rather than a single value.

A further method of calculating T_c is superconducting DFT (SCDFT), which brings superconductivity into a density-functional formalism [205, 206]. In addition to the electronic density $n(\mathbf{r})$, SCDFT introduces two extra densities: the superconducting anomalous density, corresponding to the interaction strength between (Cooper) pairs of electrons, and the nuclear density, to account for nuclear vibrations. The authors of Refs. [205, 206] show how a Kohn-Sham system of interacting nuclei and non-interacting electrons can be constructed, with potentials that are functionals of these three densities. Among its features, SCDFT does not require μ^* as input and can be

regarded as fully *ab initio*.

In closing, we mention the Quantum Espresso [207] and Electron-Phonon Wannier (EPW) [201] codes, which are widely used for the calculation of the electron-phonon coupling matrix elements of Eq. (5.5), as well as the Eliashberg spectral function and associated properties (such as T_c).[2]

5.7 Deductions from XRD data and T_c calculations

In this section, we discuss some results from XRD data and critical temperature calculations on the structures presented so far in this chapter.

Li *et al.* [114] have carried out experiments on compressed H_2S, prepared and compressed to 10 GPa at low temperature (77 K), and then further compressed to 140 GPa at room temperature. Rietveld refinement has then been carried out on XRD data obtained from these experiments, using the energetically favourable H-S structures reported in this chapter from AIRSS searches. Calculations of T_c using the methodologies described in Section 5.6 have also been carried out by the authors of Ref. [114] for these structures. We give some of the results here.

At 46 GPa, our AIRSS searches predict that $C2/c$-H_3S (Sec. 5.5.2) and $P2_12_12_1$-H_4S_3 (Sec. 5.5.6) are stable compounds - see Fig. 5.2. This pressure is right on the upper limit for the stability of $C2/m$-H_3S_2 (Sec. 5.5.5), so this compound is not considered. Li *et al.* [114] find that XRD data at this pressure is well indexed by a *mixture* of these structures: specifically, Pc-H_2S, $I4_1/acd$-S, $C2/c$-H_3S, and $P2_12_12_1$-H_4S_3, with ratios of unit cell numbers 1147:85:31:1. As stated in Sec. 5.5.4, H_2S (the starting material) is not thermodynamically stable at 46 GPa, but these results show only a partial decomposition of H_2S into other stable H-S compounds predicted in our searches. The Pc-H_2S structure is not described in this thesis and is from Ref. [181]. Other combinations of compounds (e.g., excluding H_2S) were examined, but gave poorer XRD refinements [114].

At 66 GPa, $C2/c$-H_3S, $Pnma$-H_4S_3 and $P4/nmm$-HS_2 are predicted to be stable at the static-lattice level (Fig. 5.2). However, as discussed in Sec. 5.5.7, inclusion of zero-point motion reduces the stability of HS_2 and in particular renders it unstable at 66 GPa. XRD data at this pressure is well described by a mixture of $Pnma$-H_4S_3, $C2/c$-H_3S, and Pc-H_2S, with ratios of numbers of unit cells 5:3.4:1 [114]. The decomposition of (metastable) H_2S is therefore more complete at 66 GPa, with H_4S_3 as the majority decomposition product.

At 82 GPa, Rietveld refinements index XRD data to a mixture of $Pnma$-H_4S_3, $C2/c$-H_3S and $Pmc2_1$-H_2S, with unit cell number ratios 43:6:1. At 140 GPa, XRD data

[2] At the time of writing, these codes are available to download from `http://www.quantum-espresso.org/` and `http://epw.org.uk/`, respectively.

is well indexed by *Pnma*-H_4S_3, *R*3*m*-H_3S and $P\bar{1}$-H_2S, in the ratios 56:7:1. Again, metastable H_2S structures were taken from Ref. [181]. These results are in accord with Fig. 5.2, although at the former pressure (82 GPa) the inclusion of HS_2 in Rietveld fitting does not result in a better fit, and at the latter pressure (140 GPa) a large quantity of metastable H_4S_3 appears to be present.

The experiments detailed in Ref. [114] therefore lead us to a picture whereby compressed H_2S decomposes gradually over the pressure range $\approx$ 40-140 GPa, leaving H_4S_3 as a dominant decomposition product. H_2S is metastable, but detected in experiments, over this pressure range.

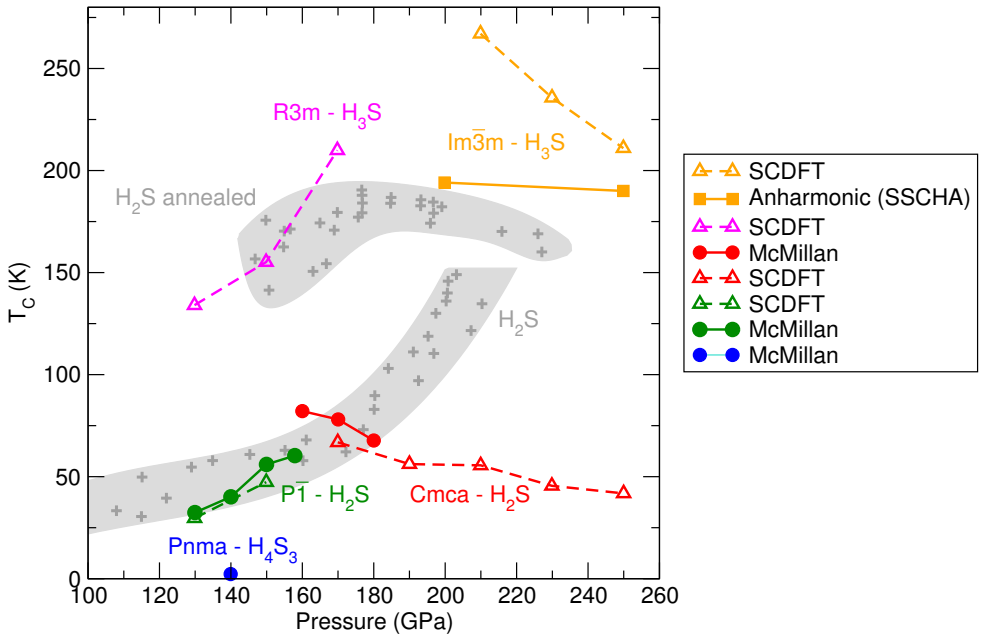

Figure 5.11: Comparison of calculated critial temperatures T_c for the *Im*$\bar{3}$*m*-H_3S (orange points), *R*3*m*-H_3S (magenta points), *Cmca*-H_2S (red points), $P\bar{1}$-H_2S (green points), and *Pnma*-H_4S_3 (blue point) structures with the experimental data from Fig. 5.1. We show only the data for compressed H_2S from Fig. 5.1, omitting the data on D_2S and sulfur. Open triangles △ and dashed lines show results calculated using superconducting DFT (SCDFT, Sec. 5.6), solid circles ● show results calculated using the McMillan equation Eq. (5.9), and solid squares ■ show results calculated by solving the Migdal-Eliashberg equations (Sec. 5.6) accounting for phonon anharmonicity through the SSCHA (Sec. 2.7.3). Aside from the solid squares, all other results treat phonons at the harmonic level. The calculated T_c values are sourced from Akashi *et al.* [208] (open triangles), Li *et al.* [181] (solid red and green circles), Li *et al.* [114] (solid blue circle), and Errea *et al.* [193] (solid squares). This figure is very similar to Fig. 1 of [208] and Fig. 5 of [114].

With regards to the T_c measurements shown in Fig. 5.1: of the compounds discussed in this section, H_2S is able to explain the observed trend in T_c, where its calculated T_c below about 170 GPa fits well with observations (blue data in Fig. 5.1). The calculated T_c for *Pnma*-H_4S_3 (using Eq. (5.9)) is too low (<2.1 K), while that for *R*3*m*-H_3S is too large [114]. Above 170 GPa, the rapid rise in T_c seen in the blue data of Fig. 5.1 is not described or accounted for by structures mentioned in this section. The situation

is illustrated in Fig. 5.11.

The set of high-temperature T_c measurements (orange data in Fig. 5.1) is accounted for by $Im\bar{3}m$-H_3S (see Fig. 5.11). Two factors are important in this regard. First, the increased stabilisation of $Im\bar{3}m$-H_3S over $R3m$-H_3S, mentioned in Sec. 5.5.2, means that the stability field of $Im\bar{3}m$-H_3S is extended downward in pressure from its static-lattice value. Second, calculations of T_c give good agreement with observed T_c values ('orange data'), but only if phonon anharmonic effects (Section 2.7.3) are taken into account, as shown by Errea *et al.* [193], and depicted in Fig. 5.11. This includes the observed trend in T_c values, which are relatively independent of pressure over a wide pressure interval.

5.8 Conclusions

High-temperature superconductivity has recently been observed in experiments compressing H_2S to 200 GPa. We have carried out variable-stoichiometry structure searches to predict stable compounds in the H-S system over the pressure range 25-200 GPa, in an effort to understand the onset of the superconducting state.

Over this pressure range, H_3S, H_7S_3, H_2S, H_3S_2, H_4S_3 and HS_2 are predicted to be stable compounds within different pressure windows. Figure 5.2 of this chapter summarises the stability ranges of these compounds, calculated at the static lattice level.

The experimental XRD data of Li *et al.* is consistent with a pressure-induced decomposition of H_2S, forming H_4S_3, H_3S and S in the structures predicted in this chapter [114]. H_4S_3 is the dominant decomposition product. H_2S is metastable above 26 GPa, and the presence of residual (undecomposed) H_2S can explain the set of low-temperature T_c measurements observed, up to 170 GPa.

Above 170 GPa, a rapid rise in T_c is seen in experiments, which is not explained directly by structures predicted in this chapter. The formation of Magnéli phases has been offered by other authors as a possible explanation [197].

The set of high-temperature T_c measurements seen in experiments can be explained by the formation of H_3S in an $Im\bar{3}m$ structure. Errea *et al.* have shown that vibrational anharmonic effects are significant for H_3S, both in terms of its thermodynamic stability, and in terms of obtaining quantitative agreement between experimental and calculated T_c values [192, 193].

Chapter 6

High-pressure calcium peroxide

Calcium and oxygen are two elements of high terrestrial and cosmic abundance, and both are components of a number of minerals. At low pressure, calcium and oxygen also form oxides, peroxides and superoxides with a variety of chemical applications. This chapter investigates calcium peroxide over the pressure range 0-200 GPa, focussing on both the ground state (0 GPa) structure and on the possible role of calcium peroxide as a planetary mantle material at high pressures, with oxygen-rich mantles in mind. The text of this chapter largely follows the work published in:

J. R. Nelson, R. J. Needs, and C. J. Pickard
Calcium peroxide from ambient to high pressures
Physical Chemistry Chemical Physics **17**, 6889−6895 (2015),

which is also Ref. [148] of this thesis.

6.1 Introduction

The typical oxide formed by calcium metal is calcium oxide, CaO, having Ca and O in +2 and -2 oxidation states respectively. Calcium and oxygen can also combine to form calcium peroxide, CaO_2, a compound which enjoys a variety of uses in industry and agriculture. Calcium peroxide is used as a source of chemically bound but easily evolved oxygen in fertilisers, for oxygenation and disinfection of water, and in soil remediation [209, 210].

At ambient pressure bulk calcium peroxide decomposes at a temperature of about 620 K [210][1]. Early X-ray diffraction (XRD) experiments assigned a tetragonal 'calcium carbide' structure of space group $I4/mmm$ to CaO_2 [211]; this structure is illustrated in Fig. 6.1. The same structure is already known in heavier alkaline earth metal peroxides [212, 213]. Recently, Zhao *et al.* [214] used an adaptive genetic algorithm (Sec. 3.6) and density functional theory (DFT) calculations to search for structures

[1]This decomposition temperature may be lower for samples of different purities; for example the CRC Handbook [W. M. Haynes (ed.), *CRC Handbook of Chemistry and Physics*, 94th ed., Taylor and Francis (2013)] reports a decomposition temperature of ≈470 K for CaO_2.

of CaO_2, and found a new orthorhombic ground state structure of $Pna2_1$ symmetry, which is calculated to be close to thermodynamic stability at zero pressure and temperature. The simulated XRD pattern from this structure is in good agreement with the experimental data of Ref. [214]. Thermodynamic stability in this case means stability against decomposition via the reaction:

$$CaO_2 \longrightarrow CaO + \frac{1}{2}O_2. \tag{6.1}$$

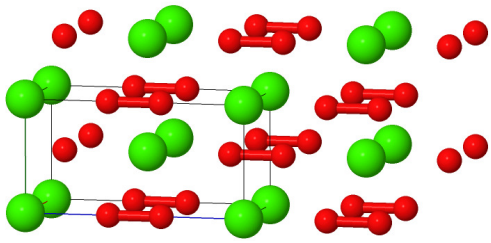

Figure 6.1: The $I4/mmm$ structure of CaO_2. At 30 GPa, we have the calculated lattice parameters $a = b = 3.117$ Å, $c = 6.116$ Å; $\alpha = \beta = \gamma = 90°$; Ca atoms occupy the $2a$ (0,0,0) Wyckoff positions, and O atoms occupy the $4e$ (0,0,0.3800) Wyckoff positions.

We explore the stabilities and structures of CaO_2 from zero pressure up to 200 GPa, and temperatures up to 1000 K. To date, almost no work has been performed investigating CaO_2 as a stable oxide of calcium at high pressures; a small amount of previous work has explored the effect of low pressures (<10 GPa) on the bond lengths and lattice parameters of $I4/mmm$-CaO_2 [212].

Calcium and oxygen have high abundances in the Earth's crust and mantle and, because they also have high cosmic abundances, stable compounds formed from these elements at high pressures are key (exo)-planetary building blocks. Understanding the structures of such compounds allows insight into the composition of planetary interiors, including exoplanets. For example, the elastic properties of Earth minerals at high temperatures and pressures are needed for accurate geophysical models of the deep Earth. These elastic properties directly affect the speed of seismic waves in the Earth's interior; as such, we require both knowledge of the composition of the Earth as a function of pressure, which can be deduced from thermodynamic stability calculations (such as that for Eq. (6.1)), while mechnical and elastic properties can also be deduced through calculation by applying known strains to the unit cells of candidate minerals and examining the resulting changes in stress and energy. The full elastic tensor C_{ij} (as opposed to just the bulk or shear moduli) can give further insight into any elastic anisotropies present in these minerals [215]. CaO is a known Earth mineral, and may be formed at high pressures in the mantle through the decomposition of $CaSiO_3$. One of our aims in this Chapter is to determine whether CaO is the only stable oxide of calcium at high pressure and temperature, or whether other oxides (like

CaO_2) can be formed under these conditions.

While, for the purposes of this Chapter, we define thermodynamic stability in terms of Eq. (6.1), separate calculations would be required to determine whether any predicted CaO_2 compound could also feasibly *coexist* with other minerals. In the case of the Earth, its iron-rich interior tends to present a chemically reducing environment [216], which could favour the reduction of higher oxides like CaO_2 even if they are thermodynamically stable according to Eq. (6.1). We do not fully examine such possibilities in this Chapter.

6.2 Methods

6.2.1 Electronic structure calculations

Density functional theory calculations are performed using the CASTEP plane-wave pseudopotential code (Sec. 2.8.1). Ultrasoft pseudopotentials of the Vanderbilt type (Sec. 2.9.5), generated with the CASTEP code, are used for both calcium and oxygen. These have core states $1s^2 2s^2 2p^6$ and $1s^2$, respectively. We use the Perdew-Burke-Ernzerhof (PBE) form of the exchange-correlation functional (Sec. 2.5.2) with a plane-wave basis cutoff of 800 eV. A Monkhorst-Pack k-point sampling density of $2\pi \times 0.03$ Å^{-1} is used for our CaO and CaO_2 phases (Sec. 2.8.3). For our oxygen phases, we use a denser k-point sampling of $2\pi \times 0.02$ Å^{-1}. Bulk modulii are calculated by fitting static lattice pressure-volume data to the third-order Birch-Murnaghan equation of state.

The electronic density of states is calculated using the OPTADOS code [105, 106, 107]. Calculations of phonon frequencies are performed with the CASTEP code and a finite-displacement supercell method, using the quasiharmonic approximation; see Secs. 2.7.1, 2.7.4 and 4.5.3, and Refs. [217, 218].

6.2.2 Validation of pseudopotentials

The Center for Molecular Modelling [219] provides a database comparing pseudopotentials from a number of different plane-wave codes, including CASTEP. Pseudopotentials are benchmarked against all-electron full-potential calculations performed with the WIEN2K code. Performance is tested by examining the equations of state for pure element phases, and comparing the energy differences between pseudopotential and all-electron calculations.

The ultrasoft pseudopotentials that are generated by CASTEP version 8.0 have been tested in this manner, and show a root-mean-square deviation in energy from an all-electron calculation of 0.5 meV/atom averaged across the periodic table. This difference is even smaller (0.06 meV/atom) for the calcium pseudopotential alone.

In this chapter, we use ultrasoft pseudopotentials generated by a slightly older version

of CASTEP. Therefore, we test our pseudopotentials against the pseudopotentials of CASTEP-8.0, by comparing the calculated equilibrium lattice parameters and enthalpies of three different CaO_2 structures using our pseudopotentials, and the pseudopotentials of CASTEP-8.0. The structures used are the $C2/c$-I, $C2/c$-II and $P2_1/c$-H structures at 0, 20 and 30 GPa respectively, which we will meet in due course.

We find a maximum enthalpy difference between the two sets of pseudopotentials of 1.41 meV/unit of CaO_2, while equilibrium lattice parameters differ by less than 0.04%. We therefore expect that the pseudopotentials used in this study are able to accurately resolve energy differences between the CaO_2 phases we have considered.

6.2.3 Structure searches

To search for new phases of CaO_2, we use the *ab initio* random structure searching (AIRSS) (Sec. 3.3).

In the searches, we use a lower plane-wave basis cutoff of 500 eV and a coarser k-point sampling density of $2\pi\times0.07$ Å^{-1} along with ultrasoft pseudopotentials generated by the CASTEP code. Once low-enthalpy candidate structures have been identified, we proceed with the higher basis cutoff energy of 800 eV and k-point sampling density of $2\pi\times0.03$ Å^{-1}. All results presented here use this stricter set of parameters, with the exception of the oxygen structures, where a denser k-point sampling is needed owing to the metallic nature of some of its phases.

In generating our starting cells for AIRSS, we require the majority of our starting cells to have at least 2 symmetry operations, in addition to having reasonable atomic bond lengths and a reasonable volume. We justify this by appealing to symmetry: low-energy minima tend to correspond to symmetrical structures [66].

Searching is carried out at 0, 10, 20, 50, 100, 150 and 200 GPa. The bulk (about 60%) of our searches use cells with 2 or 4 formula units of CaO_2, and we have also performed searches with cells containing 1, 3, 5, 6 and 8 formula units. Not all combinations of pressures and formula unit numbers are searched. In total, we relax over 25,000 structures in our searches. We supplement these results by calculating the enthalpies of five known alkaline earth metal peroxide structures taken from the Inorganic Crystal Structure Database (ICSD) [89] and from other literature [214, 216, 220]. The relevant alkaline earth metal is replaced with calcium where appropriate. The number of structures relaxed during our AIRSS searches for CaO_2 structures are tabled in Table 6.1; blank entries indicate that structure searching was not carried out for that combination of formula units and pressure.

Table 6.1: Numbers of CaO_2 structures relaxed at various pressures during structure searching. 'f.u.' is the number of formula units of CaO_2.

f.u.	0 GPa	10 GPa	20 GPa	50 GPa	100 GPa	150 GPa	200 GPa	Subtotal
1	460	272	292	340	496		549	2409
2	1111	283	280	1830	1553	1176	1210	7443
3	602	225	249	253	857		922	3108
4	1234	283	255	1288	1583	1325	1982	7950
5					94		235	329
6	360	250	280	278	580		644	2392
8	296	219	261	310	456		553	2095
							Total	25726

6.2.4 CaO

CaO undergoes a transition from the rocksalt ($Fm\bar{3}m$) to the CsCl ($Pm\bar{3}m$) structure (the B1-B2 transition) around 60-65 GPa. Diamond-anvil-cell experiments indicate a transition pressure of 60±2 GPa at room temperature [221], while DFT calculations give a transition pressure of 65-66 GPa [222, 223]. We calculate a pressure of 65 GPa in the present study, and we therefore use the $Fm\bar{3}m$ rocksalt structure below 65 GPa and the CsCl structure at higher pressures. The bulk modulus of $Fm\bar{3}m$-CaO has been measured to be 104.9 GPa [224], while our static-lattice DFT calculations give a value of 108.5 GPa. To exclude the possibility that CaO might have a different, more stable structure (other than $Fm\bar{3}m$ or $Pm\bar{3}m$) over the pressure range 0-200 GPa, we also perform AIRSS on CaO at pressures of 50, 100 and 200 GPa. We do not find any new low-enthalpy structures for CaO at these pressures.

6.2.5 Solid oxygen

Structure searching over the pressure range 0-200 GPa has already been performed for solid oxygen [225, 226], and we use the lowest enthalpy structures found therein. We also examine the enthalpies of the experimentally-determined α and δ oxygen phases at low pressures [227]. Choosing the lowest-enthalpy oxygen structure at each pressure, we find that δ-O_2 is stable between 0 and 1.2 GPa, after which an insulating phase with space group $Cmcm$ [227] is stable up to 41 GPa. A phase of symmetry $C2/m$ [226] then becomes stable, remaining so up to 200 GPa. Our spin-polarised calculations show no discernible difference in enthalpy between a δ-O_2 phase with antiferromagnetic spin ordering, and the experimentally-determined ferromagnetic spin-ordering for δ-O_2 [228].

These results are not in accord with low-temperature experiments on solid oxygen, which predict α-O_2 to be stable between 0 and about 5 GPa, δ-O_2 to be stable between about 5 and 10 GPa, followed by the 'ϵ-O_2' phase between 10 and 96 GPa, with a further isostructural phase transition around 100 GPa [229, 230, 231]. Our DFT calculations do not yield α-O_2; optimising its structure at low pressures simply gives the δ-O_2 structure. The aforementioned $C2/m$ oxygen phase is however very similar

in structure to ϵ-O_2 (which is also of $C2/m$ symmetry), and is within 50 meV/f.u. of that phase in enthalpy over the pressure range 0-200 GPa. Any higher enthalpy structure for oxygen over the pressure range being explored here would only increase the calculated stability of CaO_2 in Eq. (6.1), so we proceed with the lowest enthalpy DFT phases for oxygen. It is possible that vibrational effects could account for the energy differences discussed here, but we have not considered this further.

6.3 Results

6.3.1 Structure searching and static lattice results

Structure searching is carried out at the static-lattice level by minimising the enthalpy at a given pressure. We discuss these results first before presenting our calculations of the Gibbs free energy.

Fig. 6.2 shows the enthalpy-pressure curves for nine phases of CaO_2. The first five of these, labelled with their space group symmetries $I4/mmm$, $Pa\bar{3}$, $Pna2_1$, $Cmmm$ and $I4/mcm$ in Fig. 6.2, are known alkaline earth metal peroxide structures mentioned in Sec. 6.2. The other four, with space group symmetries $C2/c$ and $P2_1/c$, are new CaO_2 structures. These are the lowest-enthalpy phases that turned up during our AIRSS searches. The dotted line in Fig. 6.2 shows the enthalpy of $CaO+\frac{1}{2}O_2$, calculated using the lowest-enthalpy phases of CaO and O_2 at each pressure. Any CaO_2 phase below this dotted line is stable against decomposition in the manner of Eq. (6.1).

We find the following sequence of phase transitions for CaO_2 by considering the lowest enthalpy structure at each pressure:

$$C2/c\text{-I} \xrightarrow{1.8\text{ GPa}} Pna2_1 \xrightarrow{2.0\text{ GPa}} C2/c\text{-II} \xrightarrow{27.6\text{ GPa}} I4/mcm \xrightarrow{37.9\text{ GPa}} P2_1/c\text{-}L, \tag{6.2}$$

with the transition pressures between each structure as indicated by the arrows. The $P2_1/c$-L phase is then predicted to be stable up to at least 200 GPa.

6.3.2 Ground state structures

At 0 GPa, our structure searching reveals a number of CaO_2 phases which are very close (within 10 meV/f.u.) in enthalpy. Within the present approximations (DFT with PBE exchange-correlation), a phase of $C2/c$ symmetry ('$C2/c$-I') is lowest in enthalpy at 0 GPa. This phase is 8.4 meV/f.u. lower in enthalpy than the proposed $Pna2_1$-symmetry ground state structure of Zhao *et al.* [214], which we note also turned up in our AIRSS searches. Our searches also uncover a second $C2/c$-symmetry phase ('$C2/c$-II') which is slightly higher in enthalpy than $Pna2_1$ at 0 GPa. The enthalpies of these three phases at low pressures are shown in more detail in the left-hand panel of Fig. 6.2.

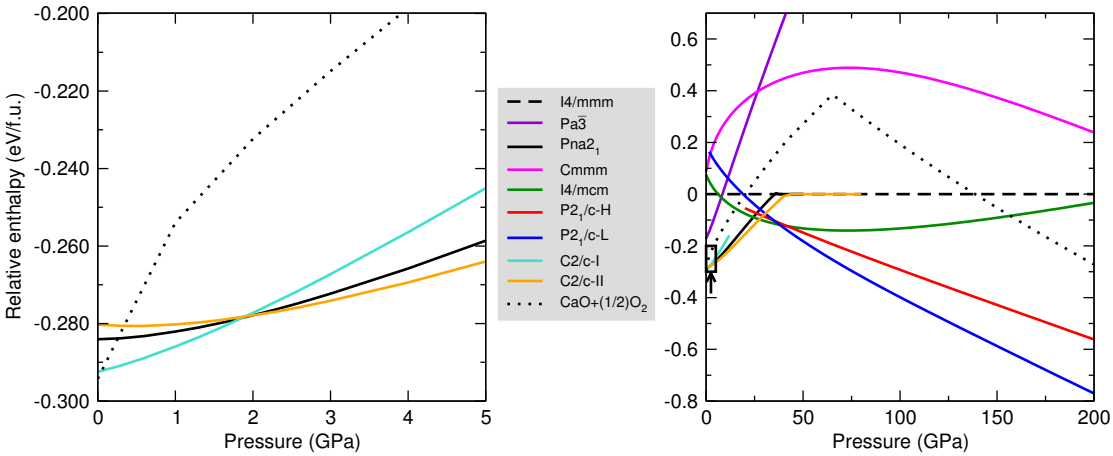

Figure 6.2: Static lattice enthalpies, in eV per unit of CaO_2, of calcium peroxide phases in the pressure range 0-5 GPa (*left*) and 0-200 GPa (*right*). Enthalpies are given relative to the $I4/mmm$ phase of CaO_2 depicted in Fig. 6.1. $C2/c$-I, $C2/c$-II, $P2_1/c$-*H* and $P2_1/c$-*L* are new structures of CaO_2 found using AIRSS. The left-hand plot highlights the enthalpy differences between the $Pna2_1$ and two $C2/c$ phases at low pressures; $C2/c$-I is the lowest-enthalpy structure at 0 GPa from our searches. The arrow and box in the right-hand figure indicate the scope of the left-hand figure. Structures of CaO_2 below the dotted line are thermodynamically stable against decomposition into CaO and O_2.

In Fig. 6.3, we show the $Pna2_1$, $C2/c$-I and $C2/c$-II phases as viewed down the crystallographic b-axis. For the $Pna2_1$ phase, we orientate the a-axis to be horizontal on the page, while the $C2/c$-I and $C2/c$-II phases are orientated so that $a+c$ (the [101] direction) is horizontal on the page.

From this perspective, calcium atoms in all three structures form an almost-hexagonal pattern in the plane of the page, consisting of elongated diamonds with a peroxide ion at the center. The monoclinic angle β is close to 120° for the $C2/c$-I and $C2/c$-II phases. A key difference between the structure of these three phases can also be seen – the peroxide ions in $C2/c$-I and $C2/c$-II are almost coplanar, whereas in $Pna2_1$ they form two sets of coplanar ions. In the $C2/c$-I and II structures, peroxide ions lie approximately in the ab-plane, and for $C2/c$-II the ions in each plane have parallel O–O bonds in the peroxide ions, while in $C2/c$-I they alternate in orientation in the same plane.

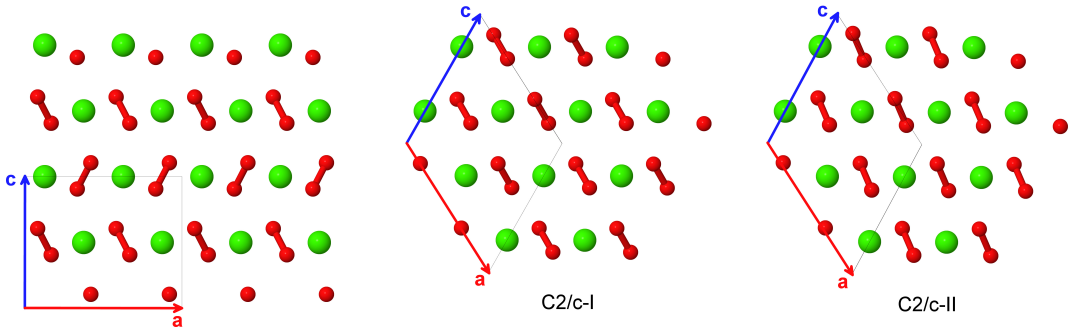

Figure 6.3: The $Pna2_1$ (*left*, unlabelled), $C2/c$-I (*middle*) and $C2/c$-II (*right*) phases of CaO_2, as viewed down the crystallographic b-axis. The a-axis is horizontal and in the plane of the page for $Pna2_1$, while the $a+c$ axis is instead horizontal for $C2/c$-I and $C2/c$-II.

In Fig. 6.4, we show these three phases again, but viewed down the a-axis (for $Pna2_1$), and down the [101] direction (for $C2/c$-I and $C2/c$-II). This view is obtained by rotating the views of Fig. 6.3 by 90° about the vertical direction of the page. From this perspective, the three phases are almost indistinguishable. Calcium ions form zig-zag rows running parallel to the a-axis ($Pna2_1$) and in the [101] direction ($C2/c$-I and $C2/c$-II).

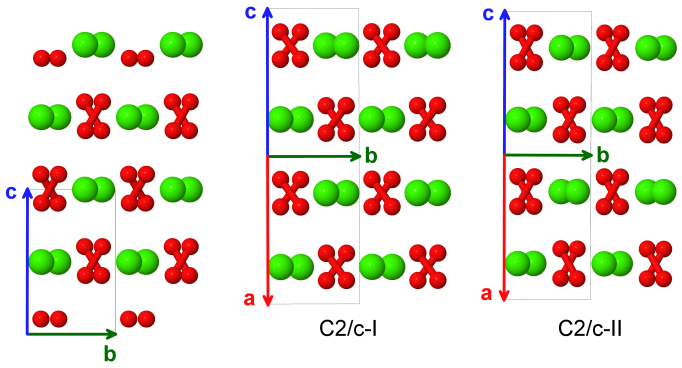

Figure 6.4: The $Pna2_1$ (*left*, unlabelled), $C2/c$-I (*middle*) and $C2/c$-II (*right*) phases of CaO_2, as viewed down the crystallographic a-axis ($Pna2_1$), and the [101] direction ($C2/c$-I and $C2/c$-II).

Calculated XRD patterns for these phases are shown in Fig. 6.5. These patterns share many similar features with available experimental data from Ref. [220], although this XRD data appears to be fitted best by the $Pna2_1$ structure.

The enthalpy differences between the $C2/c$-I, -II and $Pna2_1$ phases at 0 GPa are dependent on the choice of exchange-correlation functional. In Table 6.2, we show the enthalpies of the $Pna2_1$ and $C2/c$-II phases relative to the $C2/c$-I phase using a variety of different functionals, most of which we met already in Fig. 2.1 in our discussion of exchange enhancements. We find differences in calculated equilibrium volumes as

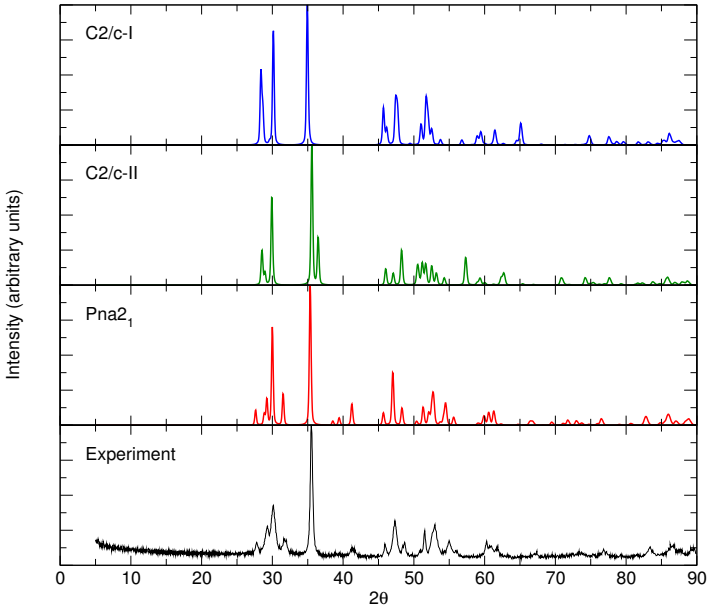

Figure 6.5: Simulated powder XRD patterns (Cu, $\lambda = 1.540562$ Å) of the $C2/c$-I and $C2/c$-II phases of CaO_2, as well as the $Pna2_1$ phase of Zhao *et al.* [214]. The lower panel shows experimental data taken from Königstein *et al.* [220]. All simulated patterns are for DFT-relaxed structures at 0 GPa.

well: for $C2/c$-I at 0 GPa, the LDA gives a volume of 35.8 Å^3/f.u., while the PBE functional gives 39.1 Å^3/f.u. The LDA typically 'overbinds' in DFT calculations, with PBE instead underbinding, so these two volumes likely bracket the true volume of the $C2/c$-I phase at 0 GPa. Given that dP/dV is about -2.3 GPa/Å^3 for this phase at 0 GPa, this volume difference (due to functional choice) corresponds to a pressure uncertainty in the neighbourhood of ± 3 GPa. In light of this uncertainty, $C2/c$-I, $C2/c$-II and $Pna2_1$ are all reasonable candidates for the structure of CaO_2 at 0 GPa.

Table 6.2: Enthalpies of the $C2/c$-II and $Pna2_1$ phases of CaO_2 at 0 GPa, in meV per unit of CaO_2, relative to the $C2/c$-I phase using different exchange-correlation functionals.

Functional	LDA	PBE	PBESOL	PW91	WC
$C2/c$-I	0.0	0.0	0.0	0.0	0.0
$Pna2_1$	0.1	8.4	2.9	8.7	3.5
$C2/c$-II	-16.3	12.2	-4.1	12.0	-2.7

6.3.3 High pressure phases

Having discussed the $Pna2_1$, $C2/c$-I and $C2/c$-II structures in some detail, we turn our attention to other phases in Eq. (6.2). Above 27.6 GPa, we predict a $I4/mcm$-symmetry structure for CaO_2; this structure has also been predicted for MgO_2 above 53 GPa [216] and subsequently observed in the experiments of Lobanov *et al.* [232]. We illustrate it in Fig. 6.6. Above 37.9 GPa, a monoclinic CaO_2 structure is then predicted to be stable, designated here as $P2_1/c$-L.

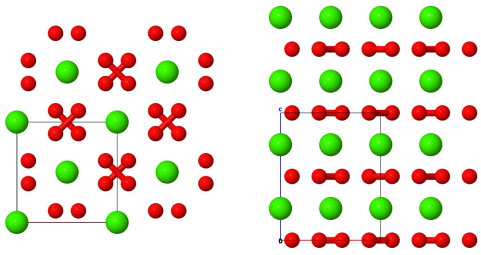

Figure 6.6: The $I4/mcm$ structure in the ab-plane (*Left*) and ac-plane (*Right*).

AIRSS searches also reveal a second phase for CaO_2 with $P2_1/c$ symmetry ('$P2_1/c$-H'). As can be seen in the right-hand panel of Fig. 6.2, our static-lattice calculations show that this is not a stable phase for CaO_2 over the pressure range 0-200 GPa. However around 38 GPa, the enthalpy of this phase lies within 10 meV/f.u. of the $I4/mcm$ and $P2_1/c$-L phases, opening up the possibility that it could become stable once we take temperature into account. We consider this further in Sec. 6.6.

We provide lattice parameters and bulk modulii for the $C2/c$-I, $C2/c$-II, $I4/mcm$, $P2_1/c$-H and $P2_1/c$-L phases at 0, 20, 30 and 50 GPa in Table 6.3.

Table 6.3: Structures of the $C2/c$-I, $C2/c$-II, $I4/mcm$, $P2_1/c$-H and $P2_1/c$-L phases of CaO_2. The calculated bulk modulii B_0 of these five phases are 87, 89, 114, 93, and 110 GPa, respectively.

		Lattice parameters			Atomic coordinates				
P	Space group	(Å, deg.)				x	y	z	Site
0	$C2/c$ (#15)[a] (I)	a=7.041	b=3.685	c=6.820	Ca	0.0000	0.6399	0.2500	4e
		α=90.0	β=117.8	γ=90.0	O	0.2548	0.1404	0.4119	8f
20	$C2/c$ (#15)[a] (II)	a=6.829	b=3.403	c=6.407	Ca	0.0000	0.3413	0.2500	4e
		α=90.0	β=118.8	γ=90.0	O	0.1661	0.1553	0.0252	8f
30	$I4/mcm$ (#140)	a=4.521	b=4.521	c=5.745	Ca	0.0000	0.0000	0.2500	4a
		α=90.0	β=90.0	γ=90.0	O	0.1143	0.6143	0.0000	8h
30	$P2_1/c$-H (#14)[b]	a=6.590	b=4.842	c=3.795	Ca	0.0611	0.7628	0.2781	4e
		α=90.0	β=105.2	γ=90.0	O	0.1301	0.2714	0.3087	4e
					O	0.2446	0.4378	0.1012	4e
50	$P2_1/c$-L (#14)[b]	a=4.223	b=4.279	c=5.949	Ca	0.0613	0.5133	0.2539	4e
		α=90.0	β=98.7	γ=90.0	O	0.0820	0.0235	0.4019	4e
					O	0.1224	0.1182	0.0089	4e

[a] $C12/c1$ - International Tables, Volume A: unique axis b, cell choice 1.
[b] $P12_1/a1$ - International Tables, Volume A: unique axis b, cell choice 3.

6.4 Bonding and electronic structure

The bandstructure of the $C2/c$-I phase at 0 GPa is shown in Fig. 6.7. The insulating nature of this phase is evident, with a calculated thermal bandgap of 2.9 eV and optical bandgap of 3.5 eV. Because these bandstructures have been calculated with the PBE functional, these values will be underestimates of the true bandgap. The top of the conduction band is shown with a black dashed line.

The right-hand panel of Fig. 6.7 shows the phonon dispersion relations and density of states for $C2/c$-I. No imaginary phonon frequencies are encountered, which ensures this structure is dynamically stable. There are a set of distinctive high-frequency phonon modes above 800 cm^{-1}, which correspond to phonon modes that stretch the covalent bond present in the peroxide $[O\text{-}O]^-$ ion.

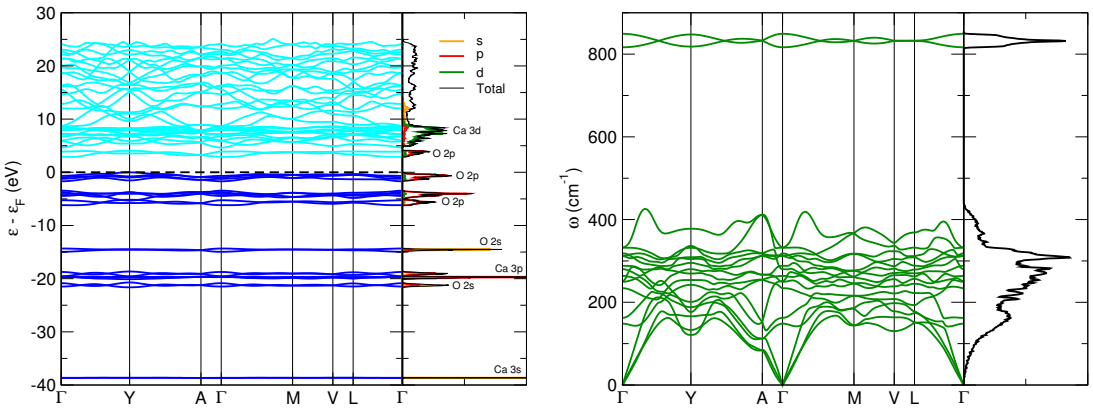

Figure 6.7: (*Left*) Electronic bandstructure and density of states for $C2/c$-I-CaO_2 at 0 GPa. We calculate a thermal bandgap of 2.9 eV and optical bandgap of 3.5 eV for this phase at 0 GPa. (*Right*) Corresponding phonon bandstructure and density of states.

The left-hand panel of Fig. 6.8 shows the electronic structure of the $P2_1/c$-L phase at 50 GPa. The composition of the electronic density of states is broadly similar to that of $C2/c$-I in Fig. 6.7, in spite of the different structure and pressure. The lowest set of 4 bands is comprised almost entirely of Ca 3s orbitals. Above this, we find a central peak flanked by two smaller sidepeaks in the total density of states. The central peak is built from 12 bands and is largely Ca 3p orbitals, while the two sidepeaks contain 4 bands apiece and are dominated by O 2s orbitals. Thus, we have a splitting of the O 2s orbital energy levels, possibly arising from the covalent bonding present in the peroxide $[O\text{-}O]^-$ ion. Above this, and just below the valence band, are 20 bands which arise largely from O 2p orbitals. The first orbitals of the conduction band consist of (unoccupied) O 2p orbitals, followed by a dense band of Ca 3d orbitals. An almost identical pattern of bonding and electronic density of states are found in our other low-enthalpy phases.

The corresponding phonon dispersion relations are found in the right-hand panel of

Fig. 6.8. This structure also has a set of distinctly separate high frequency bands around 930−1000 cm^{-1}. Two distinct peroxide O−O bond lengths are found in the ions of this structure: 1.44 Å and 1.46 Å, which splits these higher frequency bands. These bond lengths are somewhat longer those found in molecular oxygen, which has an O−O bond length of 1.207 Å [220] at ambient conditions, and the bond length in $C2/m$ oxygen at 50 GPa (Sec. 6.2.5), which we calculate as 1.20 Å. These longer O−O bond lengths are however typical of crystalline ionic peroxides [212].

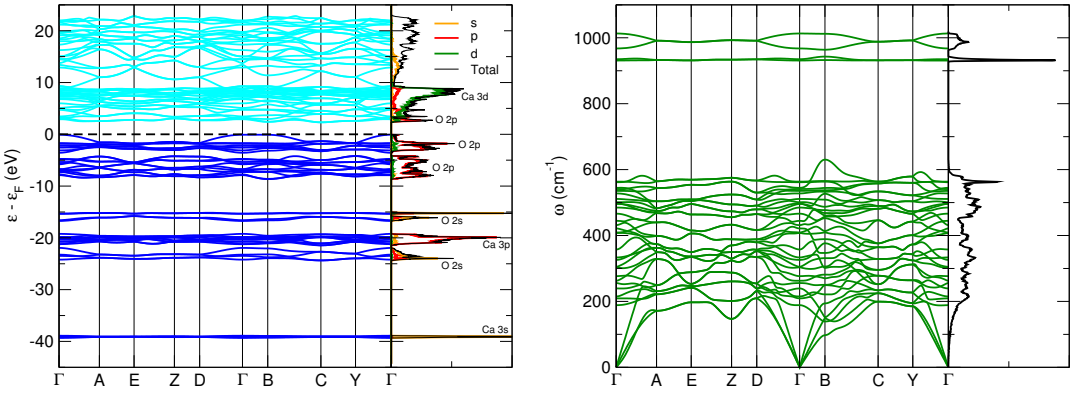

Figure 6.8: (*Left*) Bandstructure and electronic density of states of the $P2_1/c$-L phase at 50 GPa. The density of states is shown projected onto the s, p and d angular momentum channels. A thermal bandgap of 2.4 eV, and an optical bandgap of 2.5 eV, is found with the PBE functional. The top of the conduction band is shown with a black dashed line. (*Right*) Corresponding phonon dispersion relations and density of states.

6.5 Stability of CaO_2

As can be seen in Fig. 6.2, our low-enthalpy phases for CaO_2 show remarkable stability against decomposition (Eq. (6.1)) as pressure increases. We predict CaO_2 to be most stable at the B1-B2 CaO phase transition pressure of 65 GPa. There, the decomposition enthalpy (Eq. (6.1)) of CaO_2 is +0.64 eV/unit of CaO_2 (+62 kJ/mol).

One implication of the stability of CaO_2 is that it may be preferentially formed over CaO in an oxygen-rich environment under pressure, through the reverse of Eq. (6.1). For example, the pressure in the Earth's lower mantle, at a depth of around 1550 km, is about 65 GPa [221], close to our predicted peak stability pressure for CaO_2. The formation of MgO_2 in this way has also been discussed [216], although much higher pressures (>116 GPa) are needed before MgO_2 is stable against decomposition, whereas CaO_2 is stable from around 0 GPa. The mantle temperature in the Earth at 65 GPa is in the neighbourhood of 2500 K, and our phonon calculations show that under these PT conditions, $\Delta G = +0.54$ eV/f.u. for the reaction of Eq. (6.1). Hence, CaO_2 is a thermodynamically stable oxide at temperatures and pressures encountered in planetary interiors.

Reactions of the form $X+O_2 \rightarrow Y$ for species X and Y, such as the reverse of Eq. (6.1), are known as mineral redox buffers. Such reactions are key in determining planetary mantle compositions. In the Earth's mantle, there are a number of such buffers, usually involving the further oxidation of iron and nickel compounds, such as $Fe_3O_4 + \frac{1}{4}O_2 \longrightarrow \frac{3}{2}Fe_2O_3$ and $Ni + \frac{1}{2}O_2 \longrightarrow NiO$. The natural formation of CaO_2 by further oxidation of CaO in the mantle, while energetically favourable at high pressures and temperatures, would also need to compete against the further oxidation of other such compounds. The average CaO content in the Earth's mantle is about 3% [224], though exoplanet mantles offer a rich variety of alternative compositions.

We highlight the fact that the pressures at which these different CaO_2 phases are predicted to become stable are amenable to experimental study in diamond anvil cells. Very few pressure-induced phase transitions for $A[B_2]$ compounds are experimentally known [233], although at least one example already occurs among the alkaline earth metal peroxides, in BaO_2 [233]. Equivalently, it would be interesting to test the reactivity of CaO and O_2 under conditions of excess oxygen, as our results suggest that CaO and O_2 are reactive at high pressures. The formation of CaO_2 may require laser heating in a diamond anvil cell to overcome the likely high potential barriers between phases. High pressure phases of CaO_2 could be recoverable at lower pressures, although possibly not at ambient or zero pressure.

6.6 Lattice dynamics

6.6.1 Phase diagram for CaO_2

In addition to our static-lattice calculations, we calculate the phonon free energies of our lowest-enthalpy CaO_2 phases, namely those with $Pna2_1$, $C2/c$-I/II, $I4/mcm$, $P2_1/c$-H and $P2_1/c$-L symmetries. We encounter no imaginary phonon frequencies over the pressure ranges relevant to these phases, indicating that they are dynamically stable. The relevant thermodynamic potential is now the Gibbs free energy, which includes the phonon pressure. Selecting the lowest Gibbs free energy structure from these six structures gives rise to the PT phase diagram given in Fig. 6.9. We note that the upper-left (low-P, high-T) part of the phase diagram is representative only, because at ambient pressures CaO_2 decomposes at temperatures around 620 K [210].

We find that the small enthalpy difference between the $I4/mcm$ and $P2_1/c$-H phases seen in our static-lattice calculations (Fig. 6.2) closes with increasing temperature, and we see the emergence of $P2_1/c$-H as a stable phase for CaO_2 at 37.7 GPa and for $T > 281$ K. The free energy difference between the $I4/mcm$ and $P2_1/c$-H phases does remain quite small however, around 20 meV per CaO_2 unit at the most over the temperature range 0-1000 K.

At room temperature (300 K), we therefore predict a different sequence of phase tran-

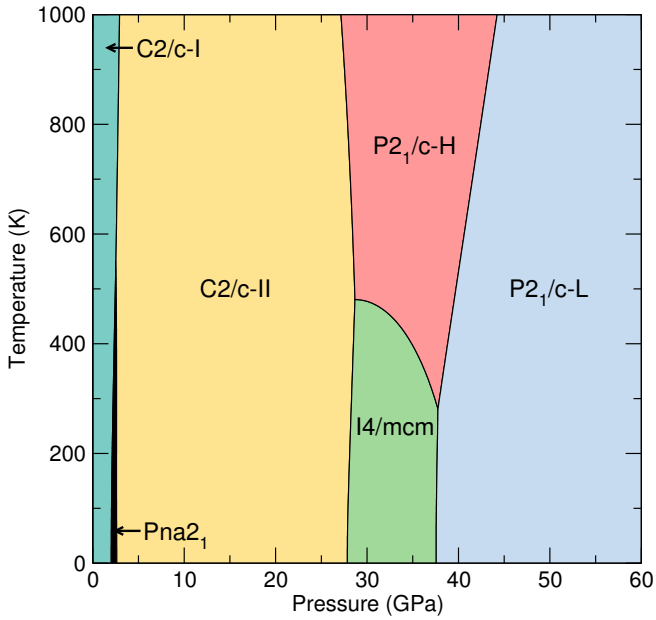

Figure 6.9: Predicted T-P phase diagram of CaO_2, calculated using the quasiharmonic approximation and our lowest-enthalpy structures from the AIRSS method.

sitions than those given in Eq. (6.2) for our static-lattice calculations. We find that, with PBE exchange-correlation:

$$C2/c\text{-I} \xrightarrow{2.2\text{ GPa}} Pna2_1 \xrightarrow{2.6\text{ GPa}} C2/c\text{-II} \xrightarrow{28.3\text{ GPa}} I4/mcm$$
$$\xrightarrow{37.4\text{ GPa}} P2_1/c\text{-}H \xrightarrow{37.9\text{ GPa}} P2_1/c\text{-}L,$$

with the arrows labelled by the predicted transition pressures.

The phase diagram of Fig. 6.9 does not extend all the way to 200 GPa. However, we expect $P2_1/c$-L to continue to be the most stable CaO_2 phase at high pressures. This is because our structure searching results (which use static-lattice enthalpies) show that the next most stable structure for CaO_2 over the pressure range 100-200 GPa is at least 45 meV per unit of CaO_2 higher in enthalpy. This was not the case at low pressures, where our searches reveal quite a few structures (such as $P2_1/c$-H) that are close to becoming stable and may therefore do so at high temperatures.

6.6.2 Equation of state for CaO_2

The equation of state of calcium peroxide from the results of both our static-lattice calculations and phonon calculations at 300 K is shown in Fig. 6.10. As mentioned already, the $P2_1/c$-H phase is not present in the static lattice equation of state, but is present over the small pressure range 37.4-37.9 GPa at 300 K.

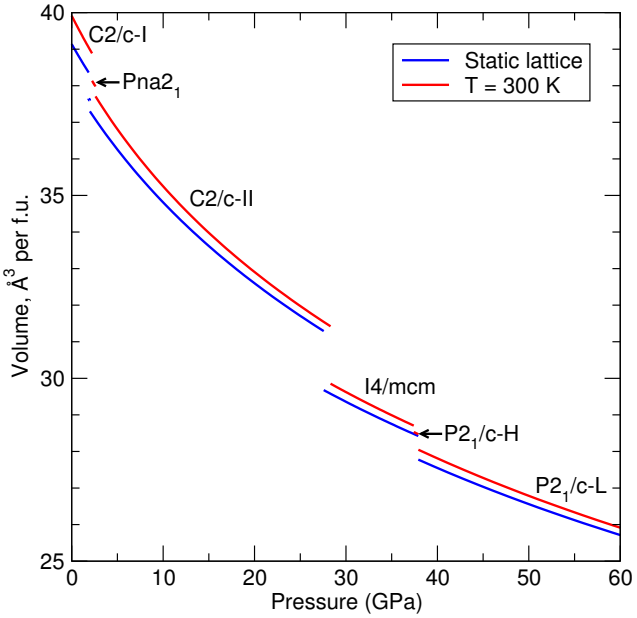

Figure 6.10: Calculated EOS for CaO_2.

6.7 Conclusions

Structural changes in CaO_2 under pressure have been explored over the pressure range 0-200 GPa and at temperatures up to 1000 K.

CaO_2 remains insulating up to pressures of at least 200 GPa. Structure searching and DFT calculations reveal six stable phases for CaO_2 over these pressure and temperature ranges, of which five are reported for the first time in this chapter. Calculations of the phonon frequencies of these new structures confirms their dynamical stability. The lowest-enthalpy phase of CaO_2 at 0 GPa is dependent on the choice of DFT exchange-correlation functional.

At pressures above 40 GPa, a phase of $P2_1/c$ symmetry ('$P2_1/c$-L') emerges for CaO_2 which is predicted to be stable up to 200 GPa, and at mantle pressures and temperatures. CaO_2 is a very stable oxide of calcium at high pressures, and may be a constituent of exoplanet mantles, formed through the further oxidation of CaO. The pressures at which these CaO_2 phases become stable are readily attainable in diamond anvil cells.

Chapter 7

Conclusions and future research

7.1 Conclusions

We have given an outline of density-functional theory and computational structure searching techniques in Chapters 2 and 3. The calculations presented in this thesis use DFT and the *ab initio* random structure search technique. Chapters 4, 5 and 6 then describe our own work using these methods.

In Chapter 4, we examined the Be-F, Mg-F and Ca-F systems at pressures up to 70 GPa. We found that:

- There are no stable compositions in the Be-F and Mg-F systems for $P < 70$ GPa, other than BeF_2 and MgF_2. For the Ca-F system, both CaF_2 and CaF_3 are stable stoichiometries.
- BeF_2 has many low-energy polymorphs at 0 GPa, and is a potential tetrahedral framework material. It has two previously unreported high pressure phases, the moganite and $CaCl_2$ silica structures.
- MgF_2 is stable in the 'orthorhombic-I' titanium dioxide structure in a small pressure window (40-44 GPa), and is a good model system for many high-pressure phase transitions in silica.
- CaF_2 has a high-pressure high-temperature phase, the Fe_2P-type $P\bar{6}2m$ structure. Classical molecular dynamics simulations show that this structure is a superionic conductor.

In Chapter 5, we examined the H-S system over the pressure range 25-200 GPa. Our main conclusions from our own results and those in the literature regarding this system are:

- The H-S system supports a large number of stable stoichiometries at different pressures, namely H_3S, H_7S_3, H_2S, H_3S_2, H_4S_3 and HS_2.

- H_2S is unstable above 26 GPa. Above 46 GPa, the reaction $H_2S \rightarrow H_4S_3 + H_3S$ is the most exothermic decomposition pathway for H_2S. Results from XRD data are consistent with this decomposition, and also the formation of S [114].
- The set of 'low-temperature' T_c values seen in experiments is consistent with undecomposed H_2S up to about 170 GPa [114]. Experiments then observe a rapid rise in T_c above this pressure, which may be accounted for by the formation of Magnéli phases intermediate to H_2S and H_3S, proposed elsewhere [197].
- The set of 'high-temperature' T_c values seen in experiments is consistent with cubic $Im\bar{3}m$-H_3S which is stabilised by strong anharmonic effects, as described by Errea *et al.* [192, 193].

Finally, in Chapter 6, we examined structures of CaO_2 at pressures up to 200 GPa. We found that:

- CaO_2 has at least six stable phases over the pressure and temperature ranges $0 \leq P \leq 200$ GPa and $0 \leq T \leq 1000$ K. It remains an insulator in these phases.
- A monoclinic structure for CaO_2, $P2_1/c$-L, is stable above 38 GPa. Under the Earth mantle conditions $P = 65$ GPa and $T = 2500$ K, CaO_2 in this structure is stable against decomposition into CaO and O_2.
- Conversely, CaO_2 could therefore form from the further oxidation of CaO in oxygen rich mantles, and the reaction $CaO + \frac{1}{2}O_2 \rightarrow CaO_2$ is a potential mineral redox buffer.
- CaO_2 has at least 3 polymorphs at 0 GPa, and the energy ordering of these depends on the treatment of exchange-correlation in DFT.

7.2 Possible future research directions

Here, we give some possible extensions of the work in Chapters 4, 5 and 6, which may be interesting directions for future research.

If we take the view established in Chapter 4 that MgF_2 models many of the high-pressure phase transitions in SiO_2, but at much lower pressures, then it would be interesting to explore a wider pressure window than just 0−70 GPa for the Mg-F system. This would include variable stoichiometries Mg_nF_m, with a view towards any implications for SiO_2, or the Si-O system. For example, there is evidence for the stability of SiO_3 above 510 GPa [234], but no other stoichiometries (other than SiO_2) are known below this pressure. These compounds have implications for models of (exo)planet interiors.

The prediction of a superionic $P\bar{6}2m$ phase for CaF_2 which is stabilised at high temperature and pressure ideally needs to be explored further. To recap, we made this prediction on the basis of harmonic phonons, attributing a phonon instability at K in the Brillouin zone to a possible superionic transition. We then carried out classi-

cal molecular dynamics simulations, which provided further evidence for a superionic transition in this structure. The resulting phase diagram of Fig. 4.16 shows our results, but some clarification is still needed for the phase boundaries above 2500 K and about 10 GPa. Anharmonic phonon calculations of the type described in Section 2.7.3 may also be useful in calculating a more accurate phase diagram for CaF_2. A more interesting direction would be to check if any other known compounds (particulary those containing Li or Na) have the $P\bar{6}2m$ structure, and whether they may also exhibit superionicity.

An obvious extension of the work in Chapter 5 is to carry on the search for new superconducting hydride materials, i.e., to extend the list of Table 5.1. This would use the searching methods of Chapter 3 and the methods for calculating T_c of Section 5.6. At the time of writing, this appears to be an active area of research.

Not all of the structures discussed in Chapter 5 have been assessed for their possible role (or lack thereof) in the observed superconductivity in the H-S system. Examples include the $C2$-H_7S_3 structure depicted in Section 5.5.3, and the layered $P4/nmm$-H_2S structure depicted in Section 5.5.4. Calculations of T_c for such structures are also a possible extension of the work in that chapter.

High pressure CaO_2 was described in Chapter 6, and CaO_2 was identified as a potential mantle material that may result from the further oxidation of CaO. To make this more concrete, the change in enthalpy for the reaction $CaO + \frac{1}{2}O_2 \rightarrow CaO_2$ should be compared to other reactions of the form $X + O_2 \rightarrow Y$, i.e., compared to other competing redox buffers, to establish whether it would remain favourable.

We did not carry out a variable stoichiometry search for compounds of the form Ca_nO_m in Chapter 6, and Ref. [235] has shown that CaO_3 is also a stable stoichiometry in this system. This opens up $CaO_2 + \frac{1}{2}O_2 \rightarrow CaO_3$ as yet another potential mineral redox buffer, and further calculations could be carried out to establish the energetics of this reaction.

Bibliography

[1] W. Kohn. *Nobel Lecture: Electronic structure of matter - wave functions and density functionals*. Reviews of Modern Physics **71**, 1253-1266 (1999).

[2] P. A. M. Dirac. *Quantum Mechanics of Many-Electron Systems*. Proceedings of the Royal Society of London. Series A, Containing Papers of a Mathematical and Physical Character **123**, 714-733 (1929).

[3] C.-K. Skylaris, P. D. Haynes, A. A. Mostofi and M. C. Payne. *Introducing ONETEP: Linear-scaling density functional simulations on parallel computers*. Journal of Chemical Physics **122**, 084119 (2005).

[4] A. Dewaele, N. Worth, C. J. Pickard, R. J. Needs, S. Pascarelli, O. Mathon, M. Mezouar, and T. Irifune. *Synthesis and stability of xenon oxides Xe_2O_5 and Xe_3O_2 under pressure*. Nature Chemistry **8**, 784-790 (2016).

[5] Y. Ma, M. Eremets, A. R. Oganov, Y. Xie, I. Trojan, S. Medvedev, A. O. Lyakhov, M. Valle, and V. Prakapenka. *Transparent dense sodium*. Nature **458**, 182-185 (2009).

[6] K. Shimizu, K. Suhara, M. Ikumo, M. I. Eremets, and K. Amaya. *Superconductivity in oxygen*. Nature **393**, 767-769 (1998).

[7] L. Dubrovinsky, N. Dubrovinskaia, V. B. Prakapenka, and A. M. Abakumov. *Implementation of micro-ball nanodiamond anvils for high-pressure studies above 6 Mbar*. Nature Communications **3**, 1163 (2012).

[8] A. Szabo and N. S. Ostlund. *Modern Quantum Chemistry*. Dover Publications (1996).

[9] R. M. Martin. *Electronic Structure: Basic Theory and Practical Methods*. Cambridge University Press (2008).

[10] M. Born and K. Huang. *Dynamical Theory of Crystal Lattices*. Clarendon Press, Oxford (1954).

[11] H. Toffoli. *Hartree-Fock theory*. Lecture IV for Physics 741: Principles of Density Functional Theory, Department of Physics, Middle East Technical University (2009).

[12] P. Giannozzi. Course notes for *Metodi Numerici per la Struttura Elettronica* (Numerical Methods in Electronic Structure), University of Udine (2009).

[13] D. M. Ceperley and B. J. Alder. *Ground State of the Electron Gas by a Stochastic Method*. Physical Review Letters **45**, 566-569 (1980).

[14] J. P. Perdew and A. Zunger. *Self-interaction correction to density-functional approximations for many-electron systems*. Physical Review B **23**, 5048-5079 (1981).

[15] S.-K. Ma and K. A. Brueckner. *Correlation Energy of an Electron Gas with a Slowly Varying High Density*. Physical Review **165**, 18-31 (1968).

[16] J. P. Perdew, K. Burke, and M. Ernzerhof. *Generalized Gradient Approximation Made Simple*. Physical Review Letters **77**, 3865-3868 (1996); Erratum Physical Review Letters **78**, 1396 (1997).

[17] A. D. Becke. *Density-functional exchange-energy approximation with correct asymptotic behavior*. Physical Review A **38**, 3098 (1988).

[18] J. P. Perdew and Y. Wang. *Accurate and simple analytic representation of the electron-gas correlation energy*. Physical Review B **45**, 13244 (1992).

[19] Z. Wu and R. E. Cohen. *More accurate generalized gradient approximation for solids*. Physical Review B **73**, 235116 (2006).

[20] J. P. Perdew, A. Ruzsinszky, G. I. Csonka, O. A. Vydrov, G. E. Scuseria, L. A. Constantin, X. Zhou, and K. Burke. *Restoring the Density-Gradient Expansion for Exchange in Solids and Surfaces*. Physical Review Letters **100**, 136406 (2008); Erratum Physical Review Letters **102**, 039902 (2009).

[21] J. Sun, J. P. Perdew, and A. Ruzsinszky. *Semilocal density functional obeying a strongly tightened bound for exchange*. Proceedings of the National Academy of Sciences **112**, 685-689 (2015).

[22] F. Tran, R. Laskowski, P. Blaha, and K. Schwarz. *Performance on molecules, surfaces, and solids of the Wu-Cohen GGA exchange-correlation energy functional*. Physical Review B **75**, 115131 (2007).

[23] A. D. Becke. *A new mixing of Hartree-Fock and local density-functional theories*. Journal of Chemical Physics **98**, 1372 (1993).

[24] A. D. Becke. *Correlation energy of an inhomogeneous electron gas: A coordinate-space model*. Journal of Chemical Physics **88**, 1053 (1988).

[25] J. P. Perdew, M. Ernzerhof, and K. Burke. *Rationale for mixing exact exchange with density functional approximations*. Journal of Chemical Physics **105**, 9982 (1996).

[26] J. Heyd, G. E. Scuseria, and M. Ernzerhof. *Hybrid functionals based on a screened Coulomb potential*. Journal of Chemical Physics **118**, 8207 (2003); Erratum Journal of Chemical Physics **124**, 219906 (2006).

[27] A. V. Krukau, O. A. Vydrov, A. F. Izmaylov, and G. E. Scuseria. *Influence of the exchange screening parameter on the performance of screened hybrid functionals*. Journal of Chemical Physics **125**, 224106 (2006).

[28] F. Zahariev, S. S. Leang, and M. S. Gordona. *Functional derivatives of meta-generalized gradient approximation (meta-GGA) type exchange-correlation density functionals*. Journal of Chemical Physics **138**, 244108 (2013).

[29] A. V. Arbuznikov. *Hybrid exchange correlation functionals and potentials: Concept elaboration*. Journal of Structural Chemistry **48**, S1-S31 (2007).

[30] R. P. Feynman. *Forces in Molecules*. Physical Review **56**, 340 (1939).

[31] O. H. Nielsen and R. M. Martin. *Quantum-mechanical theory of stress and force*. Physical Review B **32**, 3780 (1985); Erratum Physical Review B **35**, 9308 (1987).

[32] O. H. Nielsen and R. M. Martin. *First-Principles Calculation of Stress*. Physical Review Letters **50**, 697 (1983).

[33] O. H. Nielsen and R. M. Martin. *Stresses in semiconductors: Ab initio calculations on Si, Ge, and GaAs*. Physical Review B **32**, 3792 (1985).

[34] B. G. Pfrommer, M. Côté, S. G. Louie, and M. L. Cohen. *Relaxation of Crystals with the Quasi-Newton Method*. Journal of Computational Physics **131**, 233-240 (1997).

[35] Lin-Hui Ye, Bang-Gui Liu, Ding-Sheng Wang, and Rushan Han. *Ab initio phonon dispersions of single-wall carbon nanotubes*. Physical Review B **69**, 235409 (2004).

[36] A. A. Maradudin and S. H. Vosko. *Symmetry Properties of the Normal Vibrations of a Crystal*. Reviews of Modern Physics **40**, 1 (1968).

[37] F. Giustino. *Electron-phonon interactions from first principles*. Reviews of Modern Physics **89**, 015003 (2017).

[38] I. Errea, B. Rousseau, and A. Bergara. *Anharmonic Stabilization of the High-Pressure Simple Cubic Phase of Calcium*. Physical Review Letters **106**, 165501 (2011).

[39] I. Errea, M. Calandra, and F. Mauri. *Anharmonic free energies and phonon dispersions from the stochastic self-consistent harmonic approximation: Application to platinum and palladium hydrides*. Physical Review B **89**, 064302 (2014).

[40] B. Monserrat, N. D. Drummond, and R. J. Needs. *Anharmonic vibrational properties in periodic systems: energy, electron-phonon coupling, and stress*. Physical Review B **87**, 144302 (2013).

[41] G. Geneste, H. Dammak, M. Hayoun and M. Thiercelin. *Low-temperature anharmonicity of barium titanate: A path-integral molecular-dynamics study*. Physical Review B **87**, 014113 (2013).

[42] K. Refson. *Phonon and related calculations using* CASTEP (2013). Available online at `http://www.tcm.phy.cam.ac.uk/castep/Phonons_Guide/Castep_Phonons.html`.

[43] F. Detraux, Ph. Ghosez, and X. Gonze. *Comment: Long-Range Coulomb Interaction in ZrO_2*. Physical Review Letters **81**, 3297 (1998).

[44] S. Baroni, S. de Gironcoli, A. Dal Corso, and P. Giannozzi. *Phonons and related crystal properties from density-functional perturbation theory*. Reviews of Modern Physics **73**, 515 (2001).

[45] K. Parlinski, Z. Q. Li, and Y. Kawazoe. *First-Principles Determination of the Soft Mode in Cubic ZrO_2*. Physical Review Letters **78**, 4063 (1997).

[46] K. Parlinski, Z. Q. Li, and Y. Kawazoe. *Parlinski, Li, and Kawazoe Reply.* Physical Review Letters **81**, 3298 (1998).

[47] S. J. Clark, M. D. Segall, C. J. Pickard, P. J. Hasnip, M. I. J. Probert, K. Refson, and M. C. Payne. *First principles methods using CASTEP.* Zeitschrift für Kristallographie **220**, 567-570 (2005).

[48] M. C. Payne, M. P. Teter, D. C. Allan, T. A. Arias, and J. D. Joannopoulos. *Iterative minimization techniques for ab initio total-energy calculations: molecular dynamics and conjugate gradients.* Reviews of Modern Physics **64**, 1045-1097 (1992).

[49] M. D. Towler, A. Zupan, and M. Causa. *Density functional theory in periodic systems using local Gaussian basis sets.* Computer Physics Communications **98**, 181-205 (1996).

[50] L. Genovese, A. Neelov, S. Goedecker, T. Deutsch, S. A. Ghasemi, A. Willand, D. Caliste, O. Zilberberg, M. Rayson, A. Bergman, and R. Schneider. *Daubechies wavelets as a basis set for density functional pseudopotential calculations.* Journal of Chemical Physics **129**, 014109 (2008).

[51] P. Pulay. *Ab initio calculation of force constants and equilibrium geometries in polyatomic molecules. I. Theory.* Molecular Physics **17**, 197-204 (1969).

[52] H. J. Monkhorst and J. D. Pack. *Special points for Brillouin-zone integrations.* Physical Review B **13**, 5188-5192 (1976).

[53] G. Kresse and J. Furthmüller. *Efficient iterative schemes for ab initio total-energy calculations using a plane-wave basis set.* Physical Review B **54**, 11169 (1996).

[54] U. von Barth and C. D. Gelatt. *Validity of the frozen-core approximation and pseudopotential theory for cohesive energy calculations.* Physical Review B **21**, 2222 (1980).

[55] M. Fuchs and M. Scheffler. *Ab initio pseudopotentials for electronic structure calculations of poly-atomic systems using density-functional theory.* Computer Physics Communications **119**, 67-98 (1999).

[56] P. Gianozzi. *Notes on pseudopotential generation.* Available online at `http://www.quantum-espresso.org/wp-content/uploads/Doc/pseudo-gen.pdf`; dated 3 October 2016.

[57] N. Troullier and J. L. Martins. *Efficient pseudopotentials for plane-wave calculations.* Physical Review B **43**, 1993 (1991).

[58] M. Fuchs, M. Bockstedte, E. Pehlke, and M. Scheffler. *Pseudopotential study of binding properties of solids within generalized gradient approximations: The role of core-valence exchange correlation.* Physical Review B **57**, 2134 (1998).

[59] S. G. Louie, S. Froyen, and M. L. Cohen. *Nonlinear ionic pseudopotentials in spin-density-functional calculations.* Physical Review B **26**, 1738 (1982).

[60] D. R. Hamann, M. Schlüter, and C. Chiang. *Norm-Conserving Pseudopotentials.* Physical Review Letters **43**, 1494 (1979).

[61] G. P. Kerker. *Non-singular atomic pseudopotentials for solid state applications*. Journal of Physics C: Solid State Physics **13**, L189 (1980).

[62] A. M. Rappe, K. M. Rabe, E. Kaxiras, and J. D. Joannopoulos. *Optimized pseudopotentials*. Physical Review B **41**, 1227(R) (1990); Erratum Physical Review B **44**, 13175 (1991).

[63] D. D. Koelling and B. N. Harmon. *A technique for relativistic spin-polarised calculations*. Journal of Physics C: Solid State Physics **10**, 3107 (1977).

[64] D. Vanderbilt. *Soft self-consistent pseudopotentials in a generalized eigenvalue formalism*. Physical Review B **41**, 7892-7895 (1990).

[65] A. R. Oganov (Ed.). *Modern Methods of Crystal Structure Prediction*. Wiley-VCH (2010).

[66] C. J. Pickard and R. J. Needs. *Ab initio random structure searching*. Journal of Physics: Condensed Matter **23**, 053201 (2011).

[67] M. Reguzzoni, A. Fasolino, E. Molinari, and M. C. Righi. *Potential energy surface for graphene on graphene: Ab initio derivation, analytical description, and microscopic interpretation*. Physical Review B **86**, 245434 (2012).

[68] C. J. Pickard and R. J. Needs. *High-Pressure Phases of Silane*. Physical Review Letters **97**, 045504 (2006).

[69] J. Pillardy, Y. A. Arnautova, C. Czaplewski, K. D. Gibson, and H. A. Scheraga. *Conformation-family Monte Carlo: A new method for crystal structure prediction*. Proceedings of the National Academy of Sciences **98**, 12351-12356 (2001).

[70] S. M. Woodley and R. Catlow. *Crystal structure prediction from first principles*. Nature Materials **7**, 937-946 (2008).

[71] K. Doll, J. C. Schön, and M. Jansen. *Structure prediction based on ab initio simulated annealing*. Journal of Physics: Conference Series **117** 012014 (2008).

[72] K. Doll, J. C. Schön, and M. Jansen. *Structure prediction based on ab initio simulated annealing for boron nitride*. Physical Review B **78**, 144110 (2008).

[73] D. H. Brouwer and M. Horvath. *A simulated annealing approach for solving zeolite crystal structures from two-dimensional NMR correlation spectra*. Solid State Nuclear Magnetic Resonance **65**, 89-98 (2015).

[74] R. L. C. Akkermans, N. A. Spenley, and S. H. Robertson. *Monte Carlo methods in Materials Studio*. Molecular Simulation **39**, 1153-1164 (2013).

[75] D. J. Wales and H. A. Scheraga. *Global Optimization of Clusters, Crystals, and Biomolecules*. Science **285**, 1368-1372 (1999).

[76] S. Goedecker. *Minima hopping: An efficient search method for the global minimum of the potential energy surface of complex molecular systems*. Journal of Chemical Physics **120**, 9911 (2004).

[77] M. Amsler and S. Goedecker. *Crystal structure prediction using the minima hopping method*. Journal of Chemical Physics **133**, 224104 (2010).

[78] D. C. Lonie and E. Zurek. *XtalOpt: An open-source evolutionary algorithm for crystal structure prediction*. Computer Physics Communications **182**, 372-387 (2011).

[79] A. R. Oganov, A. O. Lyakhov, and M. Valle. *How Evolutionary Crystal Structure Prediction Works-and Why*. Accounts of Chemical Research **44**, 227-237 (2011).

[80] C. W. Glass, A. R. Oganov, and N. Hansen. *USPEX-Evolutionary crystal structure prediction*. Computer Physics Communications **175**, 713-720 (2006).

[81] W. W. Tipton and R. G. Hennig. *A grand canonical genetic algorithm for the prediction of multi-component phase diagrams and testing of empirical potentials*. Journal of Physics: Condensed Matter **25**, 495401 (2013).

[82] N. L. Abraham and M. I. J. Probert. *A periodic genetic algorithm with real-space representation for crystal structure and polymorph prediction*. Physical Review B **73**, 224104 (2006).

[83] N. L. Abraham and M. I. J. Probert. *Improved real-space genetic algorithm for crystal structure and polymorph prediction*. Physical Review B **77**, 134117 (2008); Erratum Physical Review B **94**, 059904 (2016).

[84] A. R. Oganov, J. Chen, C. Gatti, Y. Ma, Y. Ma, C. W. Glass, Z. Liu, T. Yu, O. O. Kurakevych, and V. L. Solozhenko. *Ionic high-pressure form of elemental boron*. Nature **457**, 863-867 (2009).

[85] A. Shamp, T. Terpstra, T. Bi, Z. Falls, P. Avery, and E. Zurek. *Decomposition Products of Phosphine Under Pressure: PH_2 Stable and Superconducting?* Journal of the American Chemical Society **138**, 1884-1892 (2016).

[86] Y. Wang, J. Lv, L. Zhu, and Y. Ma. *Crystal structure prediction via particle-swarm optimization*. Physical Review B **82**, 094116 (2010).

[87] Y. Wang, J. Lv, L. Zhu, and Y. Ma. *CALYPSO: A method for crystal structure prediction*. Computer Physics Communications **183**, 2063-2070 (2012).

[88] C. Lu, M. Miao, and Y. Ma. *Structural Evolution of Carbon Dioxide under High Pressure*. Journal of the American Chemical Society **135**, 14167-14171 (2013).

[89] *Crystallographic databases*, ed. F. H. Allen, G. Bergerhoff and R. Sievers, Chester, England: International Union of Crystallography, 1987. Database available online at `http://icsd.cds.rsc.org/`.

[90] A. Jain, S. P. Ong, G. Hautier, W. Chen, W. D. Richards, S. Dacek, S. Cholia, D. Gunter, D. Skinner, G. Ceder, and K. A. Persson. *Commentary: The Materials Project: A materials genome approach to accelerating materials innovation*. Applied Physics Letters Materials **1**, 011002 (2013). Database online at `https://materialsproject.org/`.

[91] Cambridge Structural Database. Database online at `http://www.ccdc.cam.ac.uk/Solutions/CSDSystem/Pages/CSD.aspx`.

[92] M. J. Lyle, C. J. Pickard, and R. J. Needs. *Prediction of 10-fold coordinated TiO_2 and SiO_2 structures at multimegabar pressures*. Proceedings of the National Academy of Sciences **112**, 6898-6901 (2015).

[93] S. Curtarolo, D. Morgan, K. Persson, J. Rodgers, and G. Ceder. *Predicting Crystal Structures with Data Mining of Quantum Calculations*. Physical Review Letters **91**, 135503 (2003).

[94] W. H. Dumbaugh and D. W. Morgan. *Preliminary ultraviolet transmission data for beryllium fluoride glasses*. Journal of Non-Crystalline Solids **38**, 211-216 (1980).

[95] R. T. Williams, D. J. Nagel, P. H. Klein and M. J. Weber. *Vacuum ultraviolet properties of beryllium fluoride glass*. Journal of Applied Physics **52**, 6279 (1981).

[96] J. P. M. van der Meer and R. J. M. Konings. *Thermal and physical properties of molten fluorides for nuclear applications*. Journal of Nuclear Materials **360**, 16-24 (2007).

[97] R. Appel, C. D. Dyer, and J. N. Lockwood. *Design of a broadband UV-visible α-barium borate polarizer*. Applied Optics **41**, 2470-2480 (2002).

[98] M. Daimon and A. Masumura. *High-accuracy measurements of the refractive index and its temperature coefficient of calcium fluoride in a wide wavelength range from 138 to 2326 nm*. Applied Optics **41**, 5275-5281 (2002).

[99] R. M. Hazen and L. W. Finger. *Calcium Fluoride as an Internal Pressure Standard in High-Pressure/High-Temperature Crystallography*. Journal of Applied Crystallography **14**, 234-236 (1981).

[100] B. Grocholski, S.-H. Shim, and V. B. Prakapenka. *Stability, metastability, and elastic properties of a dense silica polymorph, seifertite*. Journal of Geophysical Research: Solid Earth **118**, 4745-4757 (2013).

[101] F. Dachille and R. Roy. *High-pressure region of the silica isotypes*. Zeitschrift für Kristallographie **111**, 451-461 (1959).

[102] K. A. Walsh. *Beryllium chemistry and processing*. ASM International, Ohio, United States (2009). Section 8.3.2.

[103] J. Haines, J. M. Leger, F. Gorelli, D. D. Klug, J. S. Tse, and Z. Q. Li. *X-ray diffraction and theoretical studies of the high-pressure structures and phase transitions in magnesium fluoride*. Physical Review B **64**, 134110 (2001).

[104] K. P. Driver, R. E. Cohen, Zhigang Wu, B. Militzer, P. López Ríos, M. D. Towler, R. J. Needs, and J. W. Wilkins. *Quantum Monte Carlo computations of phase stability, equations of state, and elasticity of high-pressure silica*. Proceedings of the National Academy of Sciences **107**, 9519-9524 (2010).

[105] R. J. Nicholls, A. J. Morris, C. J. Pickard, and J. R. Yates. *OptaDOS - a new tool for EELS calculations*. Journal of Physics: Conference Series **371**, 012062 (2012).

[106] A. J. Morris, R. J. Nicholls, C. J. Pickard, and J. R. Yates. *OptaDOS: A tool for obtaining density of states, core-level and optical spectra from electronic structure codes*. Computer Physics Communications **185**, 1477-1485 (2014).

[107] J. R. Yates, X. Wang, D. Vanderbilt, and I. Souza. *Spectral and Fermi surface properties from Wannier interpolation*. Physical Review B **75**, 195121 (2007).

[108] S. Plimpton. *Fast Parallel Algorithms for Short-Range Molecular Dynamics*. Journal of Computational Physics **117**, 1 (1995).

[109] Z.-Y. Zeng, X.-R. Chen, J. Zhu, and C. Hu. *Phase Transition and Melting Curves of Calcium Fluoride via Molecular Dynamics Simulations*. Chinese Physics Letters **25**, 230 (2008).

[110] S. Faraji, S. A. Ghasemi, S. Rostami, R. Rasoulkhani, B. Schaefer, S. Goedecker, and M. Amsler. *High accuracy and transferability of a neural network potential through charge equilibration for calcium fluoride*. Physical Review B **95**, 104105 (2017).

[111] L. Pauling. *The principles determining the structure of complex ionic crystals*. Journal of the American Chemical Society **51**, 1010 (1929).

[112] R. J. Needs and C. J. Pickard. *Perspective: Role of structure prediction in materials discovery and design*. APL Materials **4**, 053210 (2016).

[113] C. J. Pickard and R. J. Needs. *Metallization of aluminum hydride at high pressures: A first-principles study*. Physical Review B **76**, 144114 (2007).

[114] Y. Li, L. Wang, H. Liu, Y. Zhang, J. Hao, C. J. Pickard, J. R. Nelson, R. J. Needs, W. Li, Y. Huang, I. Errea, M. Calandra, F. Mauri, and Y. Ma. *Dissociation products and structures of solid H_2S at strong compression*. Physical Review B **93**, 020103(R) (2016).

[115] A. Černok, E. Bykova, T. B. Ballaran, H.-P. Liermann, M. Hanfland, and L . Dubrovinsky. *High-pressure crystal chemistry of coesite-I and its transition to coesite-II*. Zeitschrift für Kristallographie **229**, 761-773 (2014).

[116] M. S. Rakitin, A. R. Oganov, H. Niu, M. M. D. Esfahani, X.-F. Zhou, G.-R. Qian, and V. L. Solozhenko. *A novel phase of beryllium fluoride at high pressure*. Physical Chemistry Chemical Physics **17**, 26283-26288 (2015).

[117] A. El Goresy, P. Dera, T. G. Sharp, C. T. Prewitt, M. Chen, L. Dubrovinsky, B. Wopenka, N. Z. Boctor and R. J. Hemley. *Seifertite, a dense orthorhombic polymorph of silica from the Martian meteorites Shergotty and Zagami*. European Journal of Mineralogy **20**, 523-528 (2008).

[118] N. A. Dubrovinskaia, L. S. Dubrovinsky, R. Ahuja, V. B. Prokopenko, V. Dmitriev, H.-P. Weber, J. M. Osorio-Guillen, and B. Johansson. *Experimental and Theoretical Identification of a New High-Pressure TiO_2 Polymorph*. Physical Review Letters **87**, 275501 (2001).

[119] J. E. Lowther, J. K. Dewhurst, J. M. Leger, and J. Haines. *Relative stability of ZrO_2 and HfO_2 structural phases*. Physical Review B **60**, 14485 (1999).

[120] A. Lazicki, A. Dewaele, P. Loubeyre, and M. Mezouar. *High-pressure-temperature phase diagram and the equation of state of beryllium*. Physical Review B **86**, 174118 (2012).

[121] M.-S. Miao. *Caesium in high oxidation states and as a p-block element*. Nature Chemistry **5**, 846-852 (2013).

[122] A. F. Wright, A. N. Fitch, and A. C. Wright. *The Preparation and Structure of the α- and β-Quartz Polymorphs of Beryllium Fluoride*. Journal of Solid State Chemistry **73**, 298-304 (1988).

[123] P. Ghalsasi and P. S. Ghalsasi. *Single Crystal X-Ray Structure of BeF_2: α-Quartz*. Inorganic Chemistry **50**, 86-89 (2011).

[124] I. Jackson. *Melting of the silica isotypes SiO_2, BeF_2 and GeO_2 at elevated pressures*. Physics of the Earth and Planetary Interiors **13**, 218-231 (1976).

[125] S. Coh and D. Vanderbilt. *Structural stability and lattice dynamics of SiO_2 cristobalite*. Physical Review B **78**, 054117 (2008).

[126] Ch. Baerlocher and L. B. McCusker. Database of Zeolite Structures: http://www.iza-structure.org/databases/.

[127] M. B. Boisen Jr., G. V. Gibbs, and M. S. T. Bukowinski. *Framework silica structures generated using simulated annealing with a potential energy function based on an $H_6Si_2O_7$ molecule*. Physics and Chemistry of Minerals **21**, 269 (1994).

[128] V. A. Blatov, A. P. Shevchenko, and D. M. Proserpio. *Applied Topological Analysis of Crystal Structures with the Program Package ToposPro*. Crystal Growth and Design **14**, 3576-3586 (2014).

[129] M. A. Zwijnenburg, F. Corà, and R. G. Bell. *Isomorphism of Anhydrous Tetrahedral Halides and Silicon Chalcogenides: Energy Landscape of Crystalline BeF_2, $BeCl_2$, SiO_2, and SiS_2*. Journal of the American Chemical Society **130**, 11082-11087 (2008).

[130] A. Togo, F. Oba, and I. Tanaka. *First-principles calculations of the ferroelastic transition between rutile-type and CaCl2-type SiO_2 at high pressures*. Physical Review B **78**, 134106 (2008).

[131] F. Yu, M. Xu, M. Jiang, and J.-X. Sun. *The phase transitions and electronic structures of crystalline BeF_2 under high-pressure: First-principle calculations*. Solid State Communications **169**, 14-19 (2013).

[132] D. M. Teter, R. J. Hemley, G. Kresse and J. Hafner. *High Pressure Polymorphism in Silica*. Physical Review Letters **80**, 2145 (1998).

[133] G. W. Stinton, S. G. MacLeod, H. Cynn, D. Errandonea, W. J. Evans, J. E. Proctor, Y. Meng, and M. I. McMahon. *Equation of state and high-pressure/high-temperature phase diagram of magnesium*. Physical Review B **90**, 134105 (2014).

[134] H. Öztürk, C. Kürkçü, and C. Kürkçü. *High-pressure structural phase transitions and intermediate phases of magnesium fluoride*. Journal of Alloys and Compounds **597**, 155-160 (2014).

[135] V. Kanchana, G. Vaitheeswaran, and M. Rajagopalan. *High-pressure structural phase transitions in magnesium fluoride studied by electronic structure calculations*. Journal of Alloys and Compounds **352**, 60-65 (2003).

[136] B. Grocholski, S.-H. Shim, and V. B. Prakapenka. *Stability of the $MgSiO_3$ analog $NaMgF_3$ and its implication for mantle structure in super-Earths*. Geophysical Research Letters **37**, L14204 (2010).

[137] S. Wu, K. Umemoto, M. Ji, C.-Z. Wang, K.-M. Ho, and R. M. Wentzcovitch. *Identification of post-pyrite phase transitions in SiO_2 by a genetic algorithm*. Physical Review B **83**, 184102 (2011).

[138] T. Tsuchiya and J. Tsuchiya. *Prediction of a hexagonal SiO_2 phase affecting stabilities of $MgSiO_3$ and $CaSiO_3$ at multimegabar pressures*. Proceedings of the National Academy of Sciences **108**, 1252-1255 (2011).

[139] J. Haines, J. M. Léger, F. Gorelli, and M. Hanfland. *Crystalline Post-Quartz Phase in Silica at High Pressure*. Physical Review Letters **87**, 155503 (2001).

[140] A. R. Oganov, Y. Ma, Y. Xu, I. Errea, A. Bergara, and A. O. Lyakhov. *Exotic behavior and crystal structures of calcium under pressure*. Proceedings of the National Academy of Sciences **107**, 7646-7651 (2010).

[141] B. Li, Y. Ding, W. Yang, L. Wang, B. Zou, J. Shu, S. Sinogeikin, C. Park, G. Zou, and H.-K. Mao. *Calcium with the β-tin structure at high pressure and low temperature*. Proceedings of the National Academy of Sciences **109**, 16459-16462 (2012).

[142] P. W. Mirwald and G. C. Kennedy. *The phase relations of calcium fluoride (fluorite) to 60 kbars and 1800° C*. Journal of Physics and Chemistry of Solids **39**, 859-861 (1978).

[143] L. Gerward, J. S. Olsen, S. Steenstrup, M. Malinowski, S. Åsbrink, and A. Waskowska. *X-ray Diffraction Investigations of CaF_2 at High Pressure*. Journal of Applied Crystallography **25**, 578-581 (1992).

[144] M. J. Gillan. *Collective dynamics in super-ionic CaF_2: I. Simulation compared with neutron-scattering experiment*. Journal of Physics C: Solid State Physics **19**, 3391 (1986).

[145] A. D. Mulliner, P. C. Aeberhard, P. D. Battle, W. I. F. David, and K. Refson. *Diffusion in Li_2O studied by non-equilibrium molecular dynamics for $873<T/K<1603$*. Physical Chemistry Chemical Physics **17**, 21470 (2015).

[146] C. Cazorla and D. Errandonea. *Giant Mechanocaloric Effects in Fluorite-Structured Superionic Materials*. Nano Letters **16**, 3124-3129 (2016).

[147] S. M. Dorfman, F. Jiang, Z. Mao, A. Kubo, Y. Meng, V. B. Prakapenka, and T. S. Duffy. *Phase transitions and equations of state of alkaline earth fluorides CaF_2, SrF_2, and BaF_2 to Mbar pressures*. Physical Review B **81**, 174121 (2010).

[148] J. R. Nelson, R. J. Needs, and C. J. Pickard. *Calcium peroxide from ambient to high pressures*. Physical Chemistry Chemical Physics **17**, 6889-6895 (2015).

[149] C. J. Pickard, M. Martinez-Canales, and R. J. Needs. *Density functional theory study of phase IV of solid hydrogen*. Physical Review B **85**, 214114 (2012); Erratum Physical Review B **86**, 059902 (2012).

[150] A. Otero-de-la-Roza, D. Abbasi-Pérez, and Víctor Luaña. *Gibbs2: A new version of the quasiharmonic model code. II. Models for solid-state thermodynamics, features and implementation*. Computer Physics Communications **182**, 2232-2248 (2011).

[151] C. Cazorla and D. Errandonea. *Superionicity and Polymorphism in Calcium Fluoride at High Pressure*. Physical Review Letters **113**, 235902 (2014).

[152] N. Sata, G. Shen, M. L. Rivers, and S. R. Sutton. *Pressure-volume equation of state of the high-pressure B2 phase of NaCl*. Physical Review B **65**, 104114 (2002).

[153] B. B. Karki, R. M. Wentzcovitch, S. de Gironcoli and S. Baroni. *First principles thermoelasticity of $MgSiO_3$-perovskite: consequences for the inferred properties of the lower mantle*. Geophysical Research Letters **28**, 2699-2702 (2001)

[154] R. M. Wentzcovitch, B. B. Karki, M. Cococcioni, and S. de Gironcoli. *Thermoelastic Properties of $MgSiO_3$-Perovskite: Insights on the Nature of the Earths Lower Mantle*. Physical Review Letters **92**, 018501 (2004).

[155] L. L. Boyer. *Nature of Melting and Superionicity in Alkali and Alkaline-Earth Halides*. Physical Review Letters **45**, 1858 (1980).

[156] P. S. Ghosh, A. Arya, G. K. Dey, N. Kuganathan, and R. W. Grimes. *A computational study on the superionic behaviour of ThO_2*. Physical Chemistry Chemical Physics **18**, 31494 (2016).

[157] M. K. Gupta, P. Goel, R. Mittal, N. Choudhury, and S. L. Chaplot. *Phonon instability and mechanism of superionic conduction in Li_2O*. Physical Review B **85**, 184304 (2012).

[158] S. Hull. *Superionics: crystal structures and conduction processes*. Reports on Progress in Physics **67**, 1233 (2004).

[159] A. M. Stoneham (Ed.). *Directions in Condensed Matter Physics - Vol. 2: Ionic Solids At High Temperatures*. World Scientific Publishing Co., Singapore (1989).

[160] C. Cazorla and D. Errandonea. *High-Pressure, High-Temperature Phase Diagram of Calcium Fluoride from Classical Atomistic Simulations*. Journal of Physical Chemistry C **117**, 11292-11301 (2013).

[161] H. Shi, W. Luo, B. Johansson and R. Ahuja. *Electronic and elastic properties of CaF_2 under high pressure from ab initio calculations*. Journal of Physics: Condensed Matter **21**, 415501 (2009).

[162] D. van Delft and P. Kes. *The discovery of superconductivity*. Physics Today **63**, 38 (2010).

[163] J. Bardeen, L. N. Cooper, and J. R. Schrieffer. *Microscopic Theory of Superconductivity*. Physical Review **106**, 162 (1957).

[164] J. Bardeen, L. N. Cooper, and J. R. Schrieffer. *Theory of Superconductivity*. Physical Review **108**, 1175 (1957).

[165] J. Nagamatsu, N. Nakagawa, T. Muranaka, Y. Zenitani, and J. Akimitsu. *Superconductivity at 39 K in magnesium diboride*. Nature **410**, 63-64 (2001).

[166] N. W. Ashcroft. *Metallic Hydrogen: A High-Temperature Superconductor?* Physical Review Letters **21**, 1748 (1968).

[167] P. Dalladay-Simpson, R. T. Howie, and E. Gregoryanz. *Evidence for a new phase of dense hydrogen above 325 gigapascals.* Nature **529**, 63-67 (2016).

[168] S. Azadi, N. D. Drummond, and W. M. C. Foulkes. *Nature of the metallization transition in solid hydrogen.* Physical Review B **95**, 035142 (2017).

[169] R. P. Dias and I. F. Silvera. *Observation of the Wigner-Huntington transition to metallic hydrogen.* Science **355**, 715-718 (2017).

[170] A. F. Goncharov and V. V. Struzhkin, *Comment on Observation of the Wigner-Huntington transition to metallic hydrogen*, arxiv:1702.04246, submitted 13 Feb 2017; M. I. Eremets and A. P. Drozdov, *Comments on the claimed observation of the Wigner-Huntington Transition to Metallic Hydrogen*, arxiv:1702.05125, submitted 16 Feb 2017; P. Loubeyre, F. Occelli, and P. Dumas, *Comment on: Observation of the Wigner-Huntington transition to metallic hydrogen*, arxiv:1702.07192, submitted 23 Feb 2017; I. Silvera and R. Dias, *Response to critiques on Observation of the Wigner-Huntington transition to metallic hydrogen*, arxiv:1703.03064, submitted 8 Mar 2017; X.-D. Liu, P. Dalladay-Simpson, R. T. Howie, B. Li, and E. Gregoryanz, *Comment on "Observation of the Wigner-Huntington transition to metallic hydrogen"*, arxiv:1704.07601, submitted 25 Apr 2017.

[171] N. W. Ashcroft. *Hydrogen Dominant Metallic Alloys: High Temperature Superconductors?* Physical Review Letters **92**, 187002 (2004).

[172] G. Gao, A. R. Oganov, P. Li, Z. Li, H. Wang, T. Cui, Y. Ma, A. Bergara, A. O. Lyakhov, T. Iitaka, and G. Zou. *High-pressure crystal structures and superconductivity of Stannane (SnH_4).* Proceedings of the National Academy of Sciences **107**, 1317-1320 (2010).

[173] X. Zhong, H. Wang, J. Zhang, H. Liu, S. Zhang, H.-F. Song, G. Yang, L. Zhang, and Y. Ma. *Tellurium Hydrides at High Pressures: High-Temperature Superconductors.* Physical Review Letters 116, 057002 (2016).

[174] Y. Li, J. Hao, H. Liu, J. S. Tse, Y. Wang, and Y. Ma. *Pressure-stabilized superconductive yttrium hydrides.* Scientific Reports **5**, 9948 (2015).

[175] Y. Fu, X. Du, L. Zhang, F. Peng, M. Zhang, C. J. Pickard, R. J. Needs, D. J. Singh, W. Zheng, and Y. Ma. *High-Pressure Phase Stability and Superconductivity of Pnictogen Hydrides and Chemical Trends for Compressed Hydrides.* Chemistry of Materials **28**, 1746-1755 (2016).

[176] J. A. Flores-Livas, A. Sanna, and E. K. U. Gross. *High temperature superconductivity in sulfur and selenium hydrides at high pressure.* European Physical Journal B **89**, 63 (2016).

[177] X. Jin, X. Meng, Z. He, Y. Ma, B. Liu, T. Cui, G. Zou, and H.-K. Mao. *Superconducting high-pressure phases of disilane.* Proceedings of the National Academy of Sciences **107**, 99699973 (2010).

[178] D. Duan, Y. Liu, F. Tian, D. Li, X. Huang, Z. Zhao, H. Yu, B. Liu, W. Tian, and T. Cui. *Pressure-induced metallization of dense $(H_2S)_2H_2$ with high-T_c superconductivity.* Scientific Reports **4**, 6968 (2014).

[179] H. Wang, J. S. Tse, K. Tanaka, T. Iitaka, and Y. Ma. *Superconductive sodalite-like clathrate calcium hydride at high pressures.* Proceedings of the National Academy of Sciences **109**, 6463-6466 (2012).

[180] M. Borinaga, I. Errea, M. Calandra, F. Mauri, and A. Bergara. *Anharmonic effects in atomic hydrogen: Superconductivity and lattice dynamical stability.* Physical Review B **93**, 174308 (2016).

[181] Y. Li, J. Hao, H. Liu, Y. Li, and Y. Ma. *The metallization and superconductivity of dense hydrogen sulfide.* Journal of Chemical Physics **140**, 174712 (2014).

[182] A. P. Drozdov, M. I. Eremets, I. A. Troyan, V. Ksenofontov, and S. I. Shylin. *Conventional superconductivity at 203 kelvin at high pressures in the sulfur hydride system.* Nature **525**, 73-76 (2015).

[183] I. Troyan, A. Gavriliuk, R. Rüffer, A. Chumakov, A. Mironovich, I. Lyubutin, D. Perekalin, A. P. Drozdov, and M. I. Eremets. *Observation of superconductivity in hydrogen sulfide from nuclear resonant scattering.* Science **351**, 1303-1306 (2016).

[184] C. J. Pickard, M. Martinez-Canales, and R. J. Needs. *Decomposition and Terapascal Phases of Water Ice.* Physical Review Letters **110**, 245701 (2013).

[185] D. Duan, X. Huang, F. Tian, D. Li, H. Yu, Y. Liu, Y. Ma, B. Liu, and T. Cui. *Pressure-induced decomposition of solid hydrogen sulfide.* Physical Review B **91**, 180502(R) (2015).

[186] N. Bernstein, C. S. Hellberg, M. D. Johannes, I. I. Mazin, and M. J. Mehl. *What superconducts in sulfur hydrides under pressure and why.* Physical Review B **91**, 060511(R) (2015).

[187] A. F. Goncharov, S. S. Lobanov, I. Kruglov, X.-M. Zhao, X.-J. Chen, A. R. Oganov, Z. Konôpková, and V. B. Prakapenka. *Hydrogen sulfide at high pressure: Change in stoichiometry.* Physical Review B **93**, 174105 (2016).

[188] C. J. Pickard and R. J. Needs. *Structure of phase III of solid hydrogen.* Nature Physics **3**, 473 (2007).

[189] O. Degtyareva, E. Gregoryanz, M. Somayazulu, P. Dera, H.-K. Mao, and R. J. Hemley. *Novel chain structures in group VI elements.* Nature Materials **4**, 152-155 (2005).

[190] H. Luo, S. Desgreniers, Y. K. Vohra, and A. L. Ruoff. *High-pressure optical studies on sulfur to 121 GPa: Optical evidence for metallization.* Physical Review Letters **67**, 2998 (1991).

[191] O. Degtyareva, E. Gregoryanz, M. Somayazulu, H.-K. Mao, and R. J. Hemley. *Crystal structure of the superconducting phases of S and Se.* Physical Review B **71**, 214104 (2005).

[192] I. Errea, M. Calandra, C. J. Pickard, J. R. Nelson, R. J. Needs, Y. Li, H. Liu, Y. Zhang, Y. Ma, and F. Mauri. *Quantum hydrogen-bond symmetrization in the superconducting hydrogen sulfide system*. Nature **532**, 81-84 (2016).

[193] I. Errea, M. Calandra, C. J. Pickard, J. Nelson, R. J. Needs, Y. Li, H. Liu, Y. Zhang, Y. Ma, and F. Mauri. *High-Pressure Hydrogen Sulfide from First Principles: A Strongly Anharmonic Phonon-Mediated Superconductor*. Physical Review Letters **114**, 157004 (2015).

[194] M. Einaga, M. Sakata, T. Ishikawa, K. Shimizu, M. I. Eremets, A. P. Drozdov, I. A. Troyan, N. Hirao, and Y. Ohishi. *Crystal structure of the superconducting phase of sulfur hydride*. Nature Physics **12**, 835-838 (2016).

[195] B. Guigue, A. Marizy, and P. Loubeyre. *Direct synthesis of pure H_3S from S and H elements: No evidence of the cubic superconducting phase up to 160 GPa*. Physical Review B **95**, 020104(R) (2017).

[196] A. F. Goncharov, S. S. Lobanov, V. B. Prakapenka, and E. Greenberg. *Stable high-pressure phases in the H-S system determined by chemically reacting hydrogen and sulfur*. Physical Review B **95**, 140101(R) (2017).

[197] R. Akashi, W. Sano, R. Arita, and S. Tsuneyuki. *Possible Magnéli Phases and Self-Alloying in the Superconducting Sulfur Hydride*. Physical Review Letters **117**, 075503 (2016).

[198] T. Ishikawa, A. Nakanishi, K. Shimizu, H. Katayama-Yoshida, T. Oda, and N. Suzuki. *Superconducting H_5S_2 phase in sulfur-hydrogen system under high-pressure*. Scientific Reports **6**, 23160 (2016).

[199] E. E. Gordon, K. Xu, H. Xiang, A. Bussmann-Holder, R. K. Kremer, A. Simon, J. Köhler, and M.-H. Whangbo. *Structure and Composition of the 200 K-Superconducting Phase of H_2S at Ultrahigh Pressure: The Perovskite $(SH^-)(H_3S^+)$*. Angewandte Chemie **55**, 3682-3684 (2016); Corrigendum Angewandte Chemie **55**, 12941-12942 (2016).

[200] F. Giustino, M. L. Cohen, and S. G. Louie. *Electron-phonon interaction using Wannier functions*. Physical Review B **76**, 165108 (2007).

[201] S. Poncé, E. R. Margine, C. Verdi, and F. Giustino. *EPW: Electron-phonon coupling, transport and superconducting properties using maximally localized Wannier functions*. Computer Physics Communications **209**, 116-133 (2016).

[202] P. B. Allen and R. C. Dynes. *Transition temperature of strong-coupled superconductors reanalyzed*. Physical Review B **12**, 905 (1975).

[203] E. R. Margine and F. Giustino. *Anisotropic Migdal-Eliashberg theory using Wannier functions*. Physical Review B **87**, 024505 (2013).

[204] E. R. Margine, H. Lambert, and F. Giustino. *Electron-phonon interaction and pairing mechanism in superconducting Ca-intercalated bilayer graphene*. Scientific Reports **6**, 21414 (2016).

[205] M. Lüders, M. A. L. Marques, N. N. Lathiotakis, A. Floris, G. Profeta, L. Fast, A. Continenza, S. Massidda, and E. K. U. Gross. *Ab initio theory of superconductivity. I. Density functional formalism and approximate functionals.* Physical Review B **72**, 024545 (2005).

[206] M. A. L. Marques, M. Lüders, N. N. Lathiotakis, G. Profeta, A. Floris, L. Fast, A. Continenza, E. K. U. Gross, and S. Massidda. *Ab initio theory of superconductivity. II. Application to elemental metals.* Physical Review B **72**, 024546 (2005).

[207] P. Giannozzi, S. Baroni, N. Bonini, M. Calandra, R. Car, C. Cavazzoni, D. Ceresoli, G. L. Chiarotti, M. Cococcioni, I. Dabo, A. Dal Corso, S. de Gironcoli, S. Fabris, G. Fratesi, R. Gebauer, U. Gerstmann, C. Gougoussis, A. Kokalj, M. Lazzeri, L. Martin-Samos, N. Marzari, F. Mauri, R. Mazzarello, S. Paolini, A. Pasquarello, L. Paulatto, C. Sbraccia, S. Scandolo, G. Sclauzero, A. P. Seitsonen, A. Smogunov, P. Umari, and R. M. Wentzcovitch. *QUANTUM ESPRESSO: a modular and open-source software project for quantum simulations of materials.* Journal of Physics: Condensed Matter **21**, 395502 (2009).

[208] R. Akashi, M. Kawamura, S. Tsuneyuki, Y. Nomura, and R. Arita. *First-principles study of the pressure and crystal-structure dependencies of the superconducting transition temperature in compressed sulfur hydrides.* Physical Review B **91**, 224513 (2015).

[209] Y. Qian, X. Zhou, Y. Zhang, W. Zhang, and J. Chen. *Performance and properties of nanoscale calcium peroxide for toluene removal.* Chemosphere **91**, 717-723 (2013).

[210] I. A. Massalimov, A. U. Shayakhmetov, and A. G. Mustafin. *Specific features of thermal decomposition of mechanically activated calcium peroxide.* Russian Journal of Applied Chemistry **83**, 1794-1798 (2010).

[211] C. Brosset and N.-G. Vannerberg. *Formation of Calcium Superoxide.* Nature **177**, 238 (1956).

[212] M. Königstein, A. A. Sokol, and C. R. A. Catlow. *Electronic structure and bonding in crystalline peroxides.* Physical Review B **60**, 4594-4604 (1999).

[213] P. D. VerNooy. *Redetermination of the structure of barium peroxide by single-crystal X-ray diffraction.* Acta Crystallographica C **49**, 433-434 (1993).

[214] X. Zhao, M. C. Nguyen, C.-Z. Wang, and K.-M. Ho. *Structures and stabilities of alkaline earth metal peroxides XO_2 (X = Ca, Be, Mg) studied by a genetic algorithm.* RSC Advances **3**, 22135-22139 (2013).

[215] S. Speziale, S. R. Shieh, and T. S. Duffy. *High-pressure elasticity of calcium oxide: A comparison between Brillouin spectroscopy and radial X-ray diffraction.* Journal of Geophysical Research **111**, B02203 (2006).

[216] Q. Zhu, A. R. Oganov, and Andriy O. Lyakhov. *Novel stable compounds in the Mg-O system under high pressure.* Physical Chemistry Chemical Physics **15**, 7696-7700 (2013).

[217] B. B. Karki and R. M. Wentzcovitch. *Vibrational and quasiharmonic thermal properties of CaO under pressure.* Physical Review B **68**, 224304 (2003).

[218] P. Carrier and R. M. Wentzcovitch. *First-principles prediction of crystal structures at high temperatures using the quasiharmonic approximation*. Physical Review B **76**, 064116 (2007); Erratum Physical Review B **76**, 189901 (2007).

[219] Center for Molecular Modelling: Comparing Solid State DFT Codes, Basis Sets and Potentials. Database online at `https://molmod.ugent.be/deltacodesdft`.

[220] M. Königstein and C. R. A. Catlow. *Ab Initio Quantum Mechanical Study of the Structure and Stability of the Alkaline Earth Metal Oxides and Peroxides*. Journal of Solid State Chemistry **140**, 103-115 (1998).

[221] R. Jeanloz, T. J. Ahrens, H. K. Mao, and P. M. Bell. *B1-B2 Transition in Calcium Oxide from Shock-Wave and Diamond-Cell Experiments*. Science **206**, 829-830 (1979).

[222] M. Catti. *Ab initio predicted metastable TlI-like phase in the B1 to B2 high-pressure transition of CaO*. Physical Review B **68**, 100101(R) (2003).

[223] J. Zhang and J. Kuo. *Phonon and elastic instabilities in rocksalt calcium oxide under pressure: a first-principles study*. Journal of Physics: Condensed Matter **21**, 015402 (2009).

[224] N. Soga. *Elastic properties of CaO under pressure and temperature*. Journal of Geophysical Research **73**, 5385-5390 (1968).

[225] J. Sun, M. Martinez-Canales, D. D. Klug, C. J. Pickard, and R. J. Needs. *Persistence and Eventual Demise of Oxygen Molecules at Terapascal Pressures*. Physical Review Letters **108**, 045503 (2012).

[226] Y. Ma, A. R. Oganov, and C. W. Glass. *Structure of the metallic ζ-phase of oxygen and isosymmetric nature of the ϵ-ζ phase transition: Ab initio simulations*. Physical Review B **76**, 064101 (2007).

[227] J. B. Neaton and N. W. Ashcroft. *Low-Energy Linear Structures in Dense Oxygen: Implications for the ϵ Phase*. Physical Review Letters **88**, 205503 (2002).

[228] I. N. Goncharenko, O. L. Makarova, and L. Ulivi. *Direct Determination of the Magnetic Structure of the Delta Phase of Oxygen*. Physical Review Letters **93**, 055502 (2004).

[229] L. F. Lundegaard, G. Weck, M. I. McMahon, S. Desgreniers, and P. Loubeyre. *Observation of an O_8 molecular lattice in the ϵ phase of solid oxygen*. Nature **443**, 201-204 (2006).

[230] H. Fujihisa, Y. Akahama, H. Kawamura, Y. Ohishi, O. Shimomura, H. Yamawaki, M. Sakashita, and Y. Gotoh, S. Takeya, and K. Honda. *O_8 Cluster Structure of the Epsilon Phase of Solid Oxygen*. Physical Review Letters **97**, 085503 (2006).

[231] Y. Akahama, H. Kawamura, D. Häusermann, M. Hanfland, and O. Shimomura. *New High-Pressure Structural Transition of Oxygen at 96 GPa Associated with Metallization in a Molecular Solid*. Physical Review Letters **74**, 4690-4693 (1995).

[232] S. S. Lobanov, Q. Zhu, N. Holtgrewe, C. Prescher, V. B. Prakapenka, A. R. Oganov, and A. F. Goncharov. *Stable magnesium peroxide at high pressure*. Scientific Reports **5**, 13582 (2015).

[233] I. Efthimiopoulos, K. Kunc, S. Karmakar, K. Syassen, M. Hanfland, and G. Vajenine. *Structural transformation and vibrational properties of BaO_2 at high pressures*. Physical Review B **82**, 134125 (2010).

[234] H. Niu, A. R. Oganov, X.-Q. Chen, and D. Li. *Prediction of novel stable compounds in the Mg-Si-O system under exoplanet pressures*. Scientific Reports **5**, 18347 (2015).

[235] A. Bouibes and A. Zaoui. *A route to possible civil engineering materials: the case of high-pressure phases of lime*. Scientific Reports **5**, 12330 (2015).